The Dissertation Committee for Kalen Elvin Braman
certifies that this is the approved version of the following dissertation:

Parametric uncertainty and sensitivity methods for reacting flows

Committee:

Venkat Raman, Supervisor

Noel Clemens

Ofodike Ezekoye

David Goldstein

Robert Moser

Parametric uncertainty and sensitivity methods for reacting flows

by

Kalen Elvin Braman, B.S.As.E., M.S.As.E.

DISSERTATION

Presented to the Faculty of the Graduate School of

The University of Texas at Austin

in Partial Fulfillment

of the Requirements

for the Degree of

DOCTOR OF PHILOSOPHY

THE UNIVERSITY OF TEXAS AT AUSTIN

May 2014

Dedicated to my friends, my family, and my loving wife Amber

Acknowledgments

First, I would like to acknowledge the support and patience of my wife Amber. In spite of the many long days and nights of work, she has stayed by my side and helped push me towards attaining my doctorate.

Next, I would like to thank my advisor Prof. Venkat Raman. The process of earning my PhD has brought me through many topics of research, some of which I did not realize I would end up pursuing. Without his advice and technical guidance, attaining my PhD would have been much more of a trial.

I also would like to thank Todd Oliver. Along the path of my research, I encountered several roadblocks. Todd's help in clarifying certain concepts has been invaluable towards improving my knowledge.

Finally, I would like to thank the DOE, whose PSAAP program has helped fund my research.

Parametric uncertainty and sensitivity methods for reacting flows

Kalen Elvin Braman, Ph.D.
The University of Texas at Austin, 2014

Supervisor: Venkat Raman

A Bayesian framework for quantification of uncertainties has been used to quantify the uncertainty introduced by chemistry models. This framework adopts a probabilistic view to describe the state of knowledge of the chemistry model parameters and simulation results. Given experimental data, this method updates the model parameters' values and uncertainties and propagates that parametric uncertainty into simulations. This study focuses on syngas, a combination in various ratios of H_2 and CO, which is the product of coal gasification. Coal gasification promises to reduce emissions by replacing the burning of coal with the less polluting burning of syngas. Despite the simplicity of syngas chemistry models, they nonetheless fail to accurately predict burning rates at high pressure. Three syngas models have been calibrated using laminar flame speed measurements. After calibration the resulting uncertainty in the parameters is propagated forward into the simulation of laminar flame speeds. The model evidence is then used to compare candidate models.

Sensitivity studies, in addition to Bayesian methods, can be used to assess chemistry models. Sensitivity studies provide a measure of how responsive target quantities of interest (QoIs) are to changes in the parameters. The adjoint equations have been derived for laminar, incompressible, variable density reacting flow and applied to hydrogen flame simulations. From the adjoint solution, the sensitivity of the QoI to the chemistry model parameters has been calculated. The results indicate the most sensitive parameters for flame tip temperature and NO_x emission. Such information can be used in the development of new experiments by pointing out which are the critical chemistry model parameters.

Finally, a broader goal for chemistry model development is set through the adjoint methodology. A new quantity, termed field sensitivity, is introduced to guide chemistry model development. Field sensitivity describes how information of perturbations in flowfields propagates to specified QoIs. The field sensitivity, mathematically shown as equivalent to finding the adjoint of the primal governing equations, is obtained for laminar hydrogen flame simulations using three different chemistry models. Results show that even when the primal solution is sufficiently close for the three mechanisms, the field sensitivity can vary.

Table of Contents

List of Tables

List of Figures

Chapter 1

Introduction

Combustion simulations of practical, large-scale geometries require vast computational resources. Those simulations must combine the capability to solve the relevant flow features with the ability to solve the relevant chemistry, as well as any other important physical phenomena. In order to reduce the computational expense, modeling choices must be made to simplify these simulations. In particular, the chemistry associated with combustion must be modeled.

In combustion flows fuel and oxidizer combine and react to form products, primarily water and carbon dioxide. In the process of forming those products, the reactants, through various chemical pathways, will form intermediate species, which will ultimately react to form the combustion products. This series of intermediate reactions cannot tractably be solved directly from first principles. Therefore, this series of reactions is modeled to approximate reality, with each reaction approximated by simple relations like the Arrhenius equation:

$$k = AT^{\eta} \exp\left(\frac{-E_A}{R_u T}\right), \tag{1.1}$$

where k is the reaction rate coefficient, T is the temperature, and R_u is the uni-

versal gas constant. The three Arrhenius parameters are the pre-exponential factor A_r, the temperature exponent η, and the activation energy E_A. With the introduction of the Arrhenius equation, chemistry modeling requires the introduction of a large number of model parameters. For example, considering hydrogen as a fuel, the reacting flow will commonly contain nine species and approximately twenty reactions [1–3]. Including the three Arrhenius parameters, the pre-exponential coefficient, temperature exponent, and activation energy, and any additional parameters such as third-body reaction efficiencies, the total number of parameters can reach 100. Considering methane as a fuel, the reacting flow can contain 37 or more species and more than 300 reactions [4, 5]. Assuming five parameters per reaction as with hydrogen, the number of parameters for methane chemistry reaches over 1,500. For more complex fuels such as diesel, chemistry models can include more than 2,800 species and over 10,000 reactions [6], leading to 50,000 or more parameters. Determining how the chemistry model parameters affect the results of simulations is an important step towards improving the accuracy and predictive capabilities of combustion simulations.

In this chapter an introduction will be given to the chemistry of reacting flow with a focus on finite rate chemistry. Then, the parametric uncertainty inherent in chemistry models will be described, including how this uncertainty affects simulations. Next, the sensitivity of simulation results to model choices will be covered. Finally, the objectives for this work will be outlined.

1.1 Reacting flow simulations

Chemical reactions can occur throughtout the flowfield of a simulation depending upon local thermodynamic state and species concentrations. In the reacting flow equations, this chemistry manifests as reaction source terms. An example of such a source is shown in the reacting scalar equation:

$$\frac{\partial \rho Y_k}{\partial t} + \frac{\partial \rho u_j Y_k}{\partial x_j} - \frac{\partial}{\partial x_j}\left(\rho D_k \frac{\partial Y_k}{\partial x_j}\right) = \omega_k, \tag{1.2}$$

for which Y_k is a reacting scalar, ρ is the density, u_j is the velocity vector corrected to maintain continuity, D_k is the mixture-averaged diffusion coefficient, and ω_k is the reaction source term. This source term is calculated based upon the local reaction rates which are typically determined from the Arrhenius equation. In that way the chemistry model parameters directly affect the source in the governing equations. In the case of turbulent reacting flow, the source term appears as an averaged source term which must be closed. This closure serves to model the effects of turbulence on the chemistry occuring in the flow. For laminar reacting flow, no such closure is required. This work will focus on laminar flows, which provide a vital first step in the development of chemistry models. Laminar flame simulations provide an important means to test the effect of chemistry models on results, while eliminating the need to account for the effects of turbulence model uncertainty in the reacting flow simulation.

For the case of laminar reacting flow, two common methods available to provide the chemistry source term include single-step chemistry and multi-

step/finite rate chemistry. With the single-step chemistry model, the set of chemical reactions which occur in the combustion of the fuel are distilled down to a single global reaction. This global reaction aims to approximate the many chemical pathways which lead from reactants to products. With finite rate chemistry, the set of chemical reactions that occur are modeled by a set of elementary reactions which are intended to cover most or all of the relevant pathways for the combustion of the fuel. In this work the focus will be on laminar reacting flow and finite rate chemistry models.

Finite rate chemistry models for even the simplest fuel, H_2, involve at least nine species and approximately twenty to thirty elementary reactions [1–3]. When modeled by the Arrhenius relation, each elementary reaction involves at least three parameters, but more commonly averages to approximately five per reaction when third body efficiencies and other parameters are included [1–3]. Thus for H_2, chemistry models involve approximately 100 model parameters. When the fuel becomes more complex such as by adding CO to form synthesis gas (syngas), the number of species and elementary reactions increases. For even more complex fuels, this list of species and reactions increases drastically leading to thousands (as with methane [4, 5]) or tens of thousands (as with diesel [6]) of chemistry model parameters.

The value of each chemistry model parameter must be determined in some fashion prior to application in simulations. These values often are determined via targeted experimental studies which aim to isolate the effects of specific elementary reactions [7, 8], or via fundamental calculations like *ab*

initio chemistry calculations [9, 10]. After these studies are completed, typically the set of Arrhenius parameters are calibrated to the results to give nominal values plus some measure of uncertainty, often a variance for the pre-exponential parameter. For larger chemistry models, some of the parameters are not easily characterized by such experiments or have not been characterized by such experiments. As a result, the Arrhenius parameters for those elementary reactions take assumed values based upon similar reactions and/or researcher intuition [11, 12].

The full set of elementary reactions which form a chemistry model requires a series of the aforementioned investigations in order to provide initial values for the set of chemistry model parameters. Further complications arise in the determination of those parameters when the sets of elementary reactions are combined together to form a chemistry model. Each elementary reaction's behavior during a targeted experiment may not exactly match that reaction's behavior in practical combustion experiments [13]. Additionally, since the Arrhenius form only approximates the behavior of reactions, the Arrhenius parameters which have a specific nominal value calculated from a targeted experiment may require a different value in concert with the other elementary reactions. As a result the chemistry parameters require additional calibration with the entire reaction set as a whole. These calibrations apply simulations to simple canonical configurations which have associated experimental data and perform some type of inversion process to infer information about the model parameters [13, 14]. Given the multiple layers of modeling choices that must be

made in order to simulate combustion chemistry, including the selection of the elementary reactions and the application of the Arrhenius form, the specification of the parameter values leads to a process in which the 'best' parameter values are selected for the model. These 'best' values lead to a model which matches closely to a set of known experimental targets. A 'true' or 'correct' set of parameter values does not exist in such a modeling framework, only the 'best' set of values determined from the most up to date set of experimental targets.

1.2 Chemistry model uncertainty and simulation uncertainty quantification

Every chemistry model lists nominal values for each parameter of each elementary reaction. Since chemistry models typically adopt the Arrhenius description of reaction rates, each elementary reaction will require three parameters. For example take the reaction $H + O_2 \rightleftharpoons O + OH$. For the syngas chemistry model of Davis [13] listed in Appendix A, the three parameters take the following values:

$$A = 2.65 \times 10^{16} \text{ cm}^3\text{/mol-s}, \ \eta = -0.671, \text{ and } E_A = 17,041 \text{ cal/mol}. \quad (1.3)$$

Simulations typically proceed using the nominal parameter values. However, a single nominal value for each parameter does not fully characterize the level of knowledge of the reaction parameters. While the temperature exponents and activation energies are typically described by just a nominal value, as stated previously each Arrhenius pre-exponential parameter is typically described

by a nominal value and variance. For the $H + O_2 \rightleftharpoons O + OH$ reaction, the variance is given as 1.855×10^{15} cm^3/mol-s. This variance indicates the uncertainty present in the determination of the target reaction's reaction rate. The uncertainty exists since the Arrhenius form cannot perfectly fit all of the data from the targeted experiment over a range of temperatures. This inability to fit occurs for two reasons: because the Arrhenius form is merely a model, and because the experimental data has a spread.

This uncertainty can be considered in a different fashion than just a variance on fitting the reaction rates. Any pre-exponential parameter value has a probability of reproducing the experimentally observed reaction rate within its experimental uncertainty. Therefore, each pre-exponential parameter can be considered a random variable with a distribution. This distribution represents the state of knowledge of the parameter's value. The temperature exponent and activation energy, although described typically only by nominal values, are not known exactly either for the same reasons stated previously. Nonetheless, for the purpose of most parameter calibrations, only the pre-exponential parameters are considered uncertain in this way [13, 14].

When all reaction parameters are conglomerated together into a single chemistry model, a high-dimensional set of parameters is formed. Adopting the probabilistic description of the parameters, the chemistry model can then be described with a high-dimensional parametric distribution. This distribution naturally can be assigned a multivariate Gaussian distribution with no covariance given the characterization of each parameter's independent distri-

bution (nominal or mean plus variance). When calibrated as a whole, the chemistry model will have new nominal values shifted from the original. Arguably more importantly, the multi-variate distribution, depending upon the method of calibration, will form a covariance and may take a new form of distribution other than Gaussian.

This inherent uncertainty in the model parameters should lead to uncertainty in the simulation results. This uncertainty is ignored when simulating only with the nominal values of the parameters. Thus, uncertainty quantification (UQ) methods have been developed to address how the uncertainty in parameters affects the outcome of simulations [14–22]. These methods focus on providing a probable range on simulation results given what is known about the range of the chemistry model parameters. However, each of these methods involves its own limitations and assumptions which can include the use of surrogate models for the target simulations and the assumption of the form of the parametric and resultant distributions.

1.3 Sensitivities

For the purpose of estimating uncertainty in simulation predictions, the desired relevant prediction must be specified. More broadly, reacting flow simulations are performed typically to obtain a specific set of results or target quantities, referred to as quantities of interest (QoIs). For a full-scale combustor simulation, the QoIs might include peak outflow temperature which can be critical in designing resilient turbine vanes, or the integrated output

of a specified pollutant like NO_x. Often, the QoIs are intended for a model validation. For that scenario the results commonly take the form of a single or a small set of quantities which may be available from an experiment, such as a small series of temperature measurements. These quantities are affected by many of the modeling choices made in the simulation, including chemistry model Arrhenius parameters. Since chemistry models form an integral part of the simulation method, the chemistry modeling choices must be made to serve the ultimate aim of the simulations.

Each QoI for a reacting flow simulation may be sensitive to any number of chemistry model parameters. Sensitivity can be described by the change in some QoI $\mathcal{J}$ due to the change in some parameter A as follows

$$S = \frac{d\mathcal{J}}{dA}. \tag{1.4}$$

Sensitivity methods aim to quantify how parameters affect the results of simulations by determining how small changes to the parameter values shift the results. Such sensitivity results are important in developing and improving chemistry models. For example, parameters that have significant uncertainty as well as significant effect upon the simulation results require further improvement. Thus the results of a sensitivity study can serve to illuminate which parameters in a model must be the focus of future studies to narrow their uncertainty.

The sensitivity S can be determined through one of a few methods including brute force, forward (direct) sensitivity, and adjoint (reverse) sen-

sitivity. Brute force methods involve repeated simulation. Each simulation proceeds with a perturbed parameter, and the difference in the resultant QoI divided by the perturbation gives the sensitivity. Forward sensitivity methods involve the simulation of an added set of sensitivity equations. In this method every primal variable has a sensitivity variable for each investigated parameter. Thus a new set of equations must be solved for every model parameter for which the sensitivity is desired. Both brute force and forward sensitivity methods provide the sensitivity of an arbitrary number of QoIs for the specified parameter. Finally, adjoint sensitivity methods involve the simulation of an added set of adjoint equations. In this method every primal equation has a corresponding adjoint equation which needs to be solved for each investigated QoI. Although each QoI requires the solution of an additional set of adjoint equations, each adjoint solution provides sensitivity to an arbitrary number of parameters.

Many studies have examined the sensitivity of various quantities to reaction parameters in homogeneous reactors and one-dimensional flows. Several of these studies have focused on the sensitivity of single-value outputs like flame speeds [3, 13, 23, 24], ignition delay times [3, 13, 25], or other assorted single-value outputs [13, 26, 27], while a smaller number have focused on the sensitivity of spatially varying quantities like temperature and species concentrations [28, 29]. Despite this proliferation of chemistry model sensitivity studies, few have focused on determining sensitivity in multi-dimensional flows.

1.4 Objective

The design specifications of reacting flow simulations require chemistry models to give accurate predictions with limited uncertainty. This aim requires that chemistry models be well-calibrated to give accurate results over the range of operating conditions required. By narrowing down the uncertainty of specific chemistry model parameters, the uncertainty in the QoIs can be reduced. This leads to an improved characterizaton of what is necessary in designing a combustor or engine in order to meet the required specifications, like reduced pollutant emission.

The objective of this work is to develop a means for investigating the uncertainty in simulations caused by chemistry modeling, as well as a means for efficiently determining the sensitivity of integrated combustion quantities to chemistry model choices. The first involves the use of Bayesian inverse methods. This work introduces the use of Bayesian inversion methods for syngas combustion chemistry models. The objective is to update the chemistry model parameters with experimental data, and subsequently to estimate the uncertainty in flame speed calculations due to parametric uncertainty. Unlike other UQ methods, this method updates parametric uncertainty without assuming a posterior distribution form and without using surrogate models. The second topic involves the development of adjoint sensitivity methods to determine efficiently how sensitive simulation results are to chemistry model parameters in the flow. This work derives the adjoint equations for laminar, incompressible, variable density reacting flow and applies those equations to simulations of

laminar hydrogen flames. The results of those simulations provide the sensitivity of two selected QoIs to the Arrhenius pre-exponential parameters of a hydrogen chemistry model including NO_x production. Finally, an additional topic involves the application of adjoint results to determining sensitivity of QoIs to perturbations in the flow field variables. This work introduces field sensitivity as a method of investigating and comparing chemistry models and applies that method to a set of hydrogen chemistry models. Together, these methods provide a means of characterizing the effects of chemistry modeling choices upon simulation results.

1.5 Outline

Building upon the above introduction and objectives, this dissertation is layed out as follows. Chapter 2 presents the calibration and uncertainty quantification of syngas models. Next, Chapter 3 describes the derivation and application of adjoints for sensitivity studies of laminar hydrogen flames. In Chapter 4, the adjoint description is extended to sensitivity of quantities to field variables. Finally, Chapter 5 presents the conclusions and future directions.

Chapter 2

Bayesian Analysis[1]

2.1 Introduction

As numerical modeling becomes critical for computational design of practical combustion devices, there is an increasing focus on the reliability of models. Specifically, an estimate of the error incurred by the different models is sought. Given that models are necessarily imperfect, a quantitative estimate of the uncertainty associated with the representation of the underlying physics needs to be obtained. This process is termed uncertainty quantification (UQ). Many different techniques for assessing uncertainty exist [14–17, 19–22, 30–33]. In this work, the Bayesian description is used to assess uncertainty. Here, the lack of knowledge or the imprecision of the model is expressed probabilistically. Learning, through experimentation or improved modeling, then manifests as a change in the probabilities. In this work, the Bayesian approach is used to analyze a syngas combustion model.

The purpose of the chemistry model is to provide reaction rates that will then be used in the spatial transport equation for species mass fractions

[1]Portions of the introductory material authored by Venkat Raman, and portions of the Bayesian methodology authored by Todd Oliver

to predict measurable quantities (e.g., mass fraction profile, burning velocity, etc.). The model itself is built for a certain range of operating conditions (e.g., high pressure or fuel-lean conditions). For the purpose of this discussion, it is assumed that the chemistry model contains all necessary pathways to describe the combustion process. In this sense, the model error arises from the inability to precisely determine the Arrhenius rate coefficients. Experiments or quantum chemistry simulations could then be used to increase the accuracy of the rate coefficients. However, both these approaches are themselves imperfect. Experiments contain measurement errors and may also be subject to inherent variability from one run to the next. Quantum chemistry calculations utilize a variety of simplifying assumptions (e.g., Born-Oppenheimer approximation, transition-state based rate computation) that will lead to errors in the potential energy surface as well as chemical rate coefficients. Consequently, the reaction rate coefficients in a chemistry model cannot be known to arbitrary precision.

Consider a chemistry model consisting of N parameters, where this number consists of pre-exponential factors, activation energies, and all model parameters used to define the entire set of reactions. None of these N parameters is known exactly, but often are given a range or a distribution. These ranges for the individual parameters combine to form a hypervolume of possible parameter settings in N-dimensional space. It is important to note that the different parameters are correlated, and that varying one without adjusting the rest is not meaningful. Using data, it is then possible to reduce this

volume and understand parameter correlations. This process is termed learning. While different UQ approaches all have this basic philosophy regarding the parameters, they vary in the methodology used to represent the relative plausibility of points inside the hypervolume as well as in the approach to using data for reducing the volume of the plausible region in this high-dimensional space.

In the area of combustion chemistry, three different approaches have been formulated. Najm and coworkers [15–17] use a polynomial chaos expansion approach, where the parameters are assumed to be random variables. Such application allows the simulation results to be treated probabilistically with the uncertainty in the model parameters propagating to those results. Frenklach and coworkers [19, 20, 30–33] propose an approach called "Data Collaboration", where estimates of the bounds of the parameters are obtained using semi-linear programming. This approach focuses on obtaining a feasible set, which is defined as the hypervolume that reproduces the experimental observations within the associated experimental uncertainty. In this sense, estimates of the lower and upper bounds of the parameter values are obtained without using a probabilistic description. Further, a response-surface approximation is used which deserves further explanation. The experimental data used to develop the uncertainty estimates typically contain laminar burning velocity or autoiginition time. In the response-surface method, the experimental measurement is represented as a quadratic function of the parameters. Since the true relation between the outputs and the parameters is highly nonlinear

and may involve spatial transport as well, this reduced-order representation itself will introduce some error. Nevertheless, Frenklach and coworkers have demonstrated in numerous studies [19, 20, 30–33] that this approach is very robust, and well-suited for the problem of chemistry modeling.

The third approach is that of Sheen and Wang [14, 21, 22], (SW), which is billed as an uncertainty minimization rather than a quantification technique. This method combines a simplified form of the Bayesian approach with the response-surface approximation. In this approach, the parameters are adjusted such that the uncertainty predicted by the chemistry model for the experimental data used in calibration is reduced. Note that the goal of uncertainty minimization is different from that of determining the hypervolume of possible parameter values. Further, while the authors themselves do not relate their technique to Bayesian technique, we show in this work that this approach is a reduced form of the Bayesian technique that invokes several simplifying assumptions. First, the PDF of the parameters is indirectly assumed to be a Gaussian distribution. Second, the response-surface approach is used to approximate the relation between the parameters and the model output. Third, in order to maintain the Gaussian nature of the PDF after the learning process, the response surface is further approximated using a linear function. Consequently, this approach has the potential to introduce large errors in the estimation of uncertainty. For instance Russi and Frenklach [34] explore the effects of assuming specific shapes for the parameter hypervolume. In particular they note the substantial error introduced by assuming high-dimensional

ellipsoids.

With this background, the purpose of this chapter is to explore the use of the Bayesian UQ approach for the modeling of syngas combustion chemistry. Syngas, which is a mixture of carbon monoxide and hydrogen, has become central to the use of integrated gasification combined cycle (IGCC) systems for carbon capture and sequestration [35, 36]. Due to the presence of hydrogen, syngas mixtures exhibit wider flammability limits and higher reactivity. Interestingly, chemistry models for syngas combustion have considerable difficulty predicting combustion characteristics (e.g., laminar flame speed) at high pressures for a range of syngas compositions [37]. Application of UQ to this system is of immediate interest, not only in characterizing the uncertainties but in determining the root cause of this prediction problem. This study evaluates the Bayesian approach, with particular focus on kinetics parameter calibration and evidence-based chemistry model comparison.

2.2 Methodology: Bayesian Analysis

The starting point for the Bayesian approach is a chemistry model with a specific set of reactions and associated rate parameters. It is assumed that some information about these rate parameters is available and is termed as prior information. The purpose of the Bayesian approach is to improve the estimates of these rate parameters based on hitherto unused experimental data. Since changing the rate parameters for a single reaction will affect the

overall performance, all the rate parameters are linked to one another and are simultaneously updated. This process is termed a global calibration approach.

In this work, a global calibration approach based on Bayesian statistics is used. Bayesian probability analysis is a well-developed field that is increasingly used to pose and solve inverse problems in many areas of science and engineering [38–42]. While some examples have appeared involving chemistry and combustion [43–45], the approach is not widely used. Thus, Sec. 2.2.1 and Sec. 2.2.2 describe the Bayesian formulations of the calibration and model comparison problems, respectively. Finally, Sec. 2.2.3 briefly describes the statistical algorithms used to compute results in this work.

2.2.1 Calibration

In the Bayesian interpretation of probability, model parameters such as kinetic rate coefficients are treated as random variables. Since the "true" value of the parameter is unknown, one represents what is known about the "true" value using probability. Then, the state of knowledge about a parameter value is represented by the PDF of the corresponding random variable. For instance, if the parameter were known with complete certainty, the corresponding PDF would be a delta function. Given these PDFs, one updates one's knowledge to account for new data by updating the parameter PDFs according to Bayes' theorem [38, 40]. Specifically, given two quantities, x and y, Bayes' theorem

states that

$$p(x|y) = \frac{p(x)p(y|x)}{p(y)}, \tag{2.1}$$

where $p(x|y)$ is the probability distribution of x, conditioned on a specific value of y, and similarly for $p(y|x)$.

In order to apply this theorem to chemistry modeling, let $\boldsymbol{\theta}$ denote the vector of uncertain kinetics parameters being calibrated. This vector will be the combination of activation energies, pre-exponential factors, and any other parameters that appear in the chemistry model. Let $\mathbf{d}$ denote the experimental data used for calibration (e.g., flame speed). Bayes' theorem implies that

$$p_{\text{post}}(\boldsymbol{\theta}|\mathbf{d}) = \frac{p_{\text{prior}}(\boldsymbol{\theta})\,\pi(\boldsymbol{\theta};\mathbf{d})}{\int p_{\text{prior}}(\boldsymbol{\theta})\,\pi(\boldsymbol{\theta};\mathbf{d})\,\mathrm{d}\boldsymbol{\theta}}. \tag{2.2}$$

In (2.2), p_{prior} denotes the prior PDF, which quantifies available information about the parameters that is independent of the data, and p_{post} denotes the posterior PDF, which quantifies the state of knowledge about the parameter values after incorporating the information in the data. These PDFs are connected through the likelihood function, $\pi(\boldsymbol{\theta};\mathbf{d})$. The likelihood function quantifies the level of agreement between the model and the data for specific values of the parameters. It is the function mapping the parameters $\boldsymbol{\theta}$ to the PDF associated with the observed data. That is,

$$\pi(\boldsymbol{\theta};\mathbf{d}) = p_{\text{like}}(\hat{\mathbf{d}}|\boldsymbol{\theta})|_{\hat{\mathbf{d}}=\mathbf{d}}, \tag{2.3}$$

where $\hat{\mathbf{d}}$ is the variable representing the observed quantity. Given only the model parameter values, the value that will be observed in an experiment

differs from the model prediction due to inadequacies in the chemistry model (model error) as well as the observation process (experimental error). The PDF p_{like} represents the state of knowledge regarding these errors. When p_{like} is evaluated at the actual observed values $\mathbf{d}$ and considered as a function of $\boldsymbol{\theta}$, it becomes the likelihood function, π.

Thus, Bayes' theorem provides a probabilistic approach for extracting information about parameters from experimental data. Furthermore, the posterior obtained from one calibration can be used as the prior for a subsequent calibration problem if more experimental data becomes available. In this sense, the Bayesian approach provides a naturally self-consistent process for learning based on all available information.

The prior and likelihood must be constructed to represent the state of knowledge before the data are obtained. Rigorous approaches for specifying these forms are the subject of ongoing research. Here, simple common forms are used to illustrate the process.

Specifically, two forms of prior PDF are used: uniform and Gaussian. A uniform prior assigns an equal prior probability density to any parameter value within its bounds, which are selected to span the expected possible range of the parameter. Alternatively, a Gaussian assigns higher prior density near the mean. Here, each Gaussian prior is assigned a mean equal to the parameter's nominal value. The standard deviation for each parameter is estimated from the uncertainty factor listed in the literature. Furthermore, the parameters are assumed to be independent in the prior.

The likelihood function is defined based on the description of the error resulting from the application of the chemistry model and the experimental error. For instance, if d_i refers to an experimental measurement at certain conditions, and x_i denotes the simulated value of this measurement (using the chemistry model), the two could be related by the following additive error model:

$$d_i = x_i + \epsilon_i, \tag{2.4}$$

where ϵ_i refers to the total error due to both experimental and modeling errors. The reasoning for the choice of combined model and experimental error is elucidated in Sec. 2.3.3. When d_i and x_i are both known, (2.4) defines ϵ_i. However, to use such a model in a calibration, one must construct a model for ϵ_i that does not depend on d_i. In this situation, the state of knowledge is expressed probabilistically. A simple model that is often used is to assume that ϵ_i are independent, identically distributed (i.i.d.) zero-mean Gaussian random variables. In this case, the likelihood function is written as

$$\pi(\boldsymbol{\theta}; \mathbf{d}) = \frac{1}{(2\pi\sigma^2)^{N_d/2}} \exp\left[-\frac{1}{2\sigma^2}\sum_{i=1}^{N_d}(d_i - x_i)^2\right], \tag{2.5}$$

where N_d is the number of data points and the hyperparameter σ denotes the standard deviation of ϵ_i. The i.i.d. assumption for ϵ_i implies that errors are independent even for data points that are close together in scenario space—i.e., that the errors in the laminar flame speeds are independent even at nearly the same pressure and equivalence ratio. While this assumption is not realistic, it allows calibration of the model parameters in a simple setting. The development of more realistic covariance structures is left for future work. Even in

this simple setting, σ is generally not known a priori, which is the case here. In this situation, σ is treated as a hyperparameter to be calibrated along with the kinetic model parameters.

A multiplicative error model is also investigated here. A multiplicative error model applies to cases in which the error is proportional to the output of the model, as can be the case for a range of conditions for which the model result varies widely in magnitude, or for cases in which the output must retain the same sign [46]. For the multiplicative error form used here, the model and experimental values are related by

$$d_i = x_i \exp(\epsilon_i). \tag{2.6}$$

Again assuming ϵ_i are Gaussian and i.i.d. leads to the following likelihood:

$$\pi(\boldsymbol{\theta}; \mathbf{d}') = \frac{1}{(2\pi\sigma^2)^{N_d/2}} \exp\left[-\frac{1}{2\sigma^2}\sum_{i=1}^{N_d}(d_i' - x_i')^2\right], \tag{2.7}$$

where $d_i' = \log d_i$ and $x_i' = \log x_i$.

It should be noted that similar modeling choices are inherent to any UQ process, not just the Bayesian methodology. All results are contingent on these choices. While the descriptions used here represent convenient choices, it should be recognized that a more in-depth analysis of the details of the chemistry models and experimental data would likely lead to more complex models. Such UQ model development is beyond the scope of the current work.

2.2.2 Model Comparison

Bayes' theorem can also be used as a basis for model comparison. This comparison methodology is used here to evaluate the relative merits of competing chemistry models. Just as PDFs are used to characterize the state of knowledge of kinetics parameters, probability can be used to characterize knowledge about which model in a given set is best.

To define the procedure, let $\mathcal{M} = \{M_1, \ldots, M_K\}$ denote a set of K candidate models M_i that one wishes to compare. The parameters of each model are calibrated using a Bayesian update based on the data $\mathbf{d}$, as described in Sec. 2.2.1. Rewriting (2.2) with explicit dependence on the model gives

$$p_{\text{post}}(\boldsymbol{\theta}_i|\mathbf{d}, M_i) = \frac{p_{\text{prior}}(\boldsymbol{\theta}_i|M_i)\,\pi(\boldsymbol{\theta}_i, M_i; \mathbf{d})}{\int p_{\text{prior}}(\boldsymbol{\theta}_i|M_i)\,\pi(\boldsymbol{\theta}_i, M_i; \mathbf{d})\,\mathrm{d}\boldsymbol{\theta}_i}, \tag{2.8}$$

where $\boldsymbol{\theta}_i$ indicates the parameters for the ith model.

In the model comparison problem, the task is to rank the models according to which is best, given the data. In the Bayesian framework, this ranking is determined by the posterior probability of the models. As in the calibration problem, the posterior distribution is determined from Bayes' theorem:

$$P_{\text{post}}(M_i|\mathbf{d}, \mathcal{M}) = \frac{P_{\text{prior}}(M_i|\mathcal{M})\,\pi_{\text{evid}}(M_i; \mathbf{d})}{\sum_{k=1}^{K} P_{\text{prior}}(M_k|\mathcal{M})\,\pi_{\text{evid}}(M_k; \mathbf{d})}. \tag{2.9}$$

In (2.9), $P_{\text{prior}}(M_i|\mathcal{M})$ is the prior probability of the model M_i. That is, it is the probability assigned to M_i based on information that is independent of the data. Often, there is very little such information. In this case, a uniform prior, i.e., $P_{\text{prior}}(M_i|\mathcal{M}) = 1/K$, is appropriate. Then, the relative

posterior probability is determined entirely by $\pi_{\text{evid}}(M_i; \mathbf{d})$, which is known as the evidence function. The evidence function measures the consistency of the model and the data considering the entire parameter space. It is given by the following integral over parameter space:

$$\pi_{\text{evid}}(M_i; \mathbf{d}) = \int p_{\text{prior}}(\boldsymbol{\theta}_i | M_i) \pi(\boldsymbol{\theta}_i, M_i; \mathbf{d}) \, \mathrm{d}\boldsymbol{\theta}_i. \tag{2.10}$$

Thus, the evidence for the model M_i is just the normalization constant (the denominator) in the calibration expression (2.8).

To gain insight into the Bayesian model comparison, note that this process can be thought of as a natural formalization of Ockham's razor. To see this interpretation, it is helpful to write the evidence in a different form. Following Muto and Beck [47], the log-evidence can be decomposed into two terms:

$$\begin{aligned} &\log\left(\pi_{\text{evid}}(M_i; \mathbf{d})\right) = \\ &\quad \int \log\left(\pi_{\text{like}}(\boldsymbol{\theta}_i, M_i; \mathbf{d})\right) \, p_{\text{post}}(\boldsymbol{\theta}_i | \mathbf{d}, M_i) \, \mathrm{d}\boldsymbol{\theta}_i \\ &\quad - \int \log\left(\frac{p_{\text{post}}(\boldsymbol{\theta}_i | \mathbf{d}, M_i)}{p_{\text{prior}}(\boldsymbol{\theta}_i | M_i)}\right) p_{\text{post}}(\boldsymbol{\theta}_i | \mathbf{d}, M_i) \, \mathrm{d}\boldsymbol{\theta}_i. \end{aligned} \tag{2.11}$$

The first term is the posterior expectation of the log-likelihood which measures how well the model is able to fit the data, averaged over the posterior PDF for the parameters. The second term is the relative information entropy (or Kullback-Leibler divergence [48]) between the posterior and the prior PDFs. It measures the information about the parameters that is gained from the data. For two models that fit the data equally well, as measured by the first term in (2.11), the model that requires the least tuning, as measured by information

gain, is preferred. For more details and discussion, see Jaynes [40] (Chapter 20) and Muto and Beck [47] (Section 4).

2.2.3 Statistical Algorithms

While the posterior PDF in (2.8) and posterior probability in (2.9) are simple to write down, evaluating and using these expressions is computationally challenging. For example, computing statistics using the posterior PDF (2.9) and computing the evidence (2.10) both require the evaluation of high-dimensional integrals. To evaluate such integrals, stochastic simulation methods have been developed in which the posterior PDF is represented by samples and integrals are approximated by Monte Carlo methods using those samples. In work presented here, an advanced stochastic simulation method, referred to as the Adaptive Multi-Level Algorithm [49, 50] is used. This algorithm involves the use of a staged Bayesian update in which the posterior is gradually approached across a sequence of intermediate updates. The main idea is to construct and then sample a sequence of intermediate distributions between the prior and the posterior. Specifically, at the ℓth intermediate "level", one uses Markov chain Monte Carlo to sample

$$\pi_{\text{int}}^{(\ell)}(\boldsymbol{\theta}; \mathbf{d}) \propto p_{\text{prior}}(\boldsymbol{\theta}) \pi(\boldsymbol{\theta}; \mathbf{d})^{\tau_\ell}, \tag{2.12}$$

where $0 \leq \tau_\ell \leq 1$. Clearly, when $\tau_\ell = 0$, $\pi_{\text{int}}^{(\ell)}$ is the prior, and when $\tau_\ell = 1$ it is the posterior. After sampling at level ℓ, a selection of the samples generated is used to begin Markov chains for the $\ell + 1$th intermediate distribution, where

$\tau_{\ell+1} > \tau_\ell$. Complete details of the algorithm can be found in [50]. This algorithm is implemented in the QUESO library [51], which was used to generate all of the results shown in Sec. 2.4 and Sec. 2.5.

2.3 Application of Bayesian approach to high-pressure syngas combustion modeling

For application in hydrogen-rich gas turbines for power generation, the chemistry models have to be calibrated at high pressure and low equivalence ratio conditions. Here, three different chemistry models are used to demonstrate the Bayesian approach to model calibration, model selection, and error propagation.

2.3.1 Synthesis gas chemical kinetics models

Three kinetics models from Davis et al. [13], Li et al. [52], and Sun et al. [53] are considered here. For simplicity, these models will be referred to as DM, LM, and SM, respectively, from here forward.

The DM involves 14 species and 30 reactions. The Arrhenius reaction rate parameters were compiled from recent kinetics experiments as well as the GRI 3.0 model. The Arrhenius reaction rate pre-exponential coefficient was optimized for 19 of those reactions based upon experimental results of laminar flame speeds, peak mole fractions of low-pressure burner-stabilized flames, fuel consumption rates in a turbulent flow reactor, and ignition delay times behind reflected shock waves. The LM involves 14 species and 31 reactions. Reaction

rate parameters for this model were compiled by calibration to data from formaldehyde oxidation in a flow reactor, from a hydrogen-oxygen model [2], and by calibration to other recent experimental data. The SM involves 15 species and 33 reactions. The reaction rate parameters were compiled from recent literature, including *ab initio* calculations for specific reactions. The three models have an identical list of species involved, except for the SM, which also involves CH_2O.

2.3.2 Kinetic parameters used in Bayesian calibration

The Bayesian methodology can incorporate the calibration of an arbitrary selection of model parameters. In combustion, the pertinent parameters include those from the kinetics model such as the Arrhenius pre-exponential coefficient, temperature exponent, activation energy, and third body efficiencies, as well as those from transport and thermodynamic models. For the context of this study, only Arrhenius pre-exponential coefficients in each syngas kinetics model have been incorporated in the Bayesian update. Of course, in general, the set of parameters need not be limited only to the pre-exponential coefficients.

Additionally, the method of Sheen and Wang has been incorporated in this study for comparison to the Bayesian method. The Sheen and Wang method commonly restricts itself to pre-exponential parameters. That method, in order to minimize computational cost, incorporates a list of pre-exponential parameters selected by a sensitivity study for each experimental target rather

than all pre-exponential parameters. In the cases shown in Sec. 2.5, after the sensitivities of the flame speed to the kinetics parameters, $\frac{\partial \eta}{\partial \ln k_j}$, were calculated, the sensitivity-uncertainty index (SUI) [54], $C_j(\eta) = |\frac{\partial \eta}{\partial \ln k_j} f_j|$, was calculated for each parameter. In this expression, η is the simulated flame speed, k_j is the parameter and $f_i = \log_{10}(k_j^0/k_j^{min}) = \log_{10}(k_j^{max}/k_j^0)$ is the multiplicative uncertainty factor, which relates the literature-listed uncertainty in each rate parameter. In the expression for the uncertainty factor, the superscript 0 refers to the nominal value of the parameter and min and max refer to two standard deviations away from the nominal. These indices give a relative ranking of the sensitivity of the flame speed calculations to each parameter weighted by the uncertainty in that parameter. The sensitivity threshold was set as 10% of the maximum SUI for each experimental target.

2.3.3 Premixed laminar flame experiments and simulations

The Bayesian update of the model parameters incorporates information from experimental data with results from corresponding simulations. For this update process, laminar premixed flame experiments were chosen. The high pressure flame speed data of Sun et al. [53] serves as the experimental data set. These data were selected because the conditions approximate those expected in ground-based combustors. Specifically, experiments conducted at equivalence ratios of 1.2 or lower and at pressures of 5 and 10 atm are used for calibration. Flame speed data for a pressure of 20 atm are used for predictive comparison. The CO:H_2 ratios of 1, 3, and 19 were tested. These conditions

and the observed flame speed values are listed in Table 2.1. Note that the experimental error in the flame speed is not reported by [53] and, thus, for simplicity, the experimental error is lumped with the model error in ϵ_i during calibration, as discussed in Sec. 2.2.1. Simulations of premixed laminar flames were completed with the CHEMKIN PREMIX routines [55]. The standard CHEMKIN routines for thermodynamic and transport properties [56] were also used.

The Bayesian process need not be restricted to a single type of experiment. Other experimental results such as autoignition times may be used in the process. For this procedure, laminar flame speeds were selected since they provide a fundamental basis for many turbulent combustion models.

2.4 Bayesian Calibration Results

This section details the results of the use of the Bayesian methodology for UQ of syngas kinetics models. The three kinetics models are calibrated, uncertainty is propagated, and the model results are compared in Sec. 2.4.1. Next, the Bayesian evidence is used to compare the relative plausibility of each kinetics model in Sec. 2.4.2. Then, the form of the prior distributions is discussed in the context of the DM in Sec. 2.4.3, and the form of the error model is discussed in the context of the LM in Sec. 2.4.4.

Table 2.1: Experimental data [53] used in calibration and comparisons

p (atm.)	$CO:H_2$	ϕ	η (cms)
5.0	1.0	0.8	79.4
5.0	1.0	1.0	113.6
5.0	1.0	1.2	136.1
5.0	3.0	0.8	52.6
5.0	3.0	1.0	64.3
5.0	3.0	1.2	81.3
5.0	19.0	1.2	40.6
10.0	1.0	0.6	27.8
10.0	1.0	0.8	68.7
10.0	1.0	1.0	101.2
10.0	1.0	1.2	128.0
10.0	3.0	0.6	25.9
10.0	3.0	0.8	43.9
10.0	3.0	1.0	64.1
10.0	3.0	1.2	79.3
10.0	19.0	0.8	21.2
10.0	19.0	1.0	27.7
10.0	19.0	1.2	39.1
20.0	3.0	0.8	36.3
20.0	3.0	1.0	56.3
20.0	3.0	1.2	68.7
20.0	19.0	1.0	29.2
20.0	19.0	1.2	36.7
40.0	19.0	1.0	30.1

2.4.1 Bayesian calibration and uncertainty propagation

The Bayesian uncertainty analysis first updates the model parameters according to Eqn. 2.2 with the algorithm described in Sec. 2.2.3. This calibration leads to an updated level of knowledge regarding the uncertain parameters in the kinetics model as provided by the joint posterior distribution. All Arrhenius pre-exponential coefficients from the three kinetics models, 37 for the DM, 36 for the LM, and 44 for the SM, are updated in this fashion using the additive error model and Gaussian priors. The use of the additive error model also introduces an additional parameter, the error model variance hyperparameter, leading to 38, 37, and 45 updated uncertain parameters for the DM, LM, and SM models, respectively. The data set used for the calibration is the laminar flame speed data described in Sec. 2.3.3.

The final joint and marginal parameter distributions are constructed from the full dimensional sampling results. Figure 2.1 shows a section of the raw chain, as well as the autocorrelation, for the parameter with the slowest decaying autocorrelation. The chain itself shows reasonable mixing, and the autocorrelation, although long lasting, dies out at approximately 500 samples. For each test case, the full computation took approximately 15,000 processor hours, using 3.33 GHz compute cores with two GB memory per core. The majority of the computational time is spent computing the flame speed. Each sample flame speed calculation takes approximately one to three seconds depending on the number of iterations required to reach convergence. The multi-level algorithm computes approximately 300,000 accepted samples on

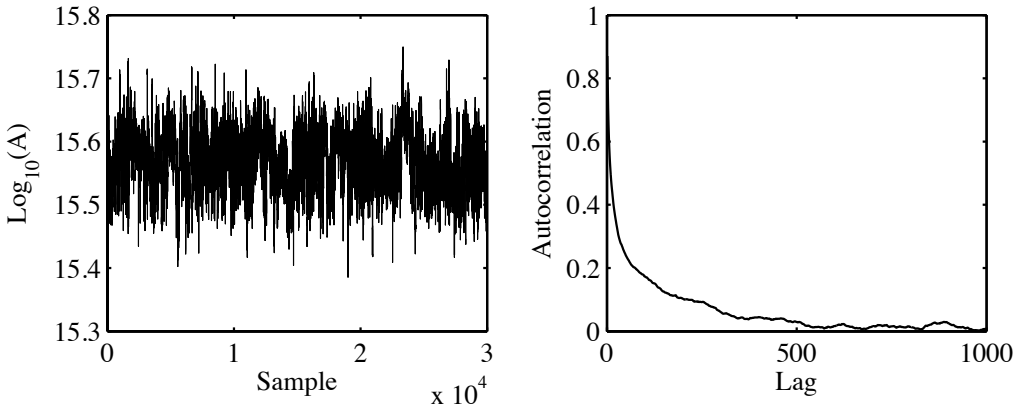

Figure 2.1: (left) Subsection of sampling results and (right) autocorrelation for the O + H_2 ⇌ H + OH pre-exponential coefficient in the LM

the final level.

The left side of Fig. 2.2 shows a selection of the marginal posterior PDFs obtained by the stochastic multilevel algorithm for select pre-exponential parameters plotted with the Gaussian prior distributions (the right side of this figure will be discussed in Sec. 2.4.3). The prior distributions are shown as dashed lines and the marginal distributions as solid lines. Note that the posterior PDF for a multi-parameter calibration is a joint PDF of all the parameters. Here, only the marginal PDFs are shown. The shift from the prior distribution to the posterior shows some of the information gained by calibrating the kinetics model parameters to the data set. For some parameters, the distribution remains nearly the same. For example the posterior distributions of reactions O + H_2 ⇌ H + OH and H_2O_2 + OH ⇌ HO_2 + H_2O shift little from the priors. For other parameters, such as OH + H_2 ⇌ H + H_2O and CO + OH ⇌ CO_2 + H, the most likely value shifts or the shape of the dis-

tribution changes. In particular the distribution for the parameter of CO + OH $\rightleftharpoons$ CO_2 + H shifts significantly lower and becomes slightly tail heavy and more peaked. Thus certain parameters are informed more by the Bayesian update. Such results imply either that the chosen experiments contain more information regarding those shifted parameters or that the information in the experiments has already been encapsulated in the prior distribution for the uninformed parameters.

To further investigate the information provided regarding the parameters by the calibration data, Figure 2.3 shows the Kullback-Leibler (KL) divergence between the marginal posterior and prior PDFs for all parameters in each model. Most parameters have a small divergence, indicating that those parameters have gained little from the calibration. This result is not surprising given that the number of parameters is greater than the number of data points, and thus not every parameter is identifiable using only this data. Further, only parameters that significantly affect the computed laminar flame speed will be constrained by the Bayesian update. Thus, low KL divergence indicates that, over the range of the prior, the parameter does not greatly influence the laminar flame speed for the calibration cases. However, some of the parameters, in particular the pre-exponential coefficients for CO + OH $\leftrightharpoons$ CO_2 + H and its duplicate reactions in all three models, have relatively large divergence. These parameters have gained the most from the Bayesian update, indicating that the chosen experiments provide information for the calibration of those parameters.

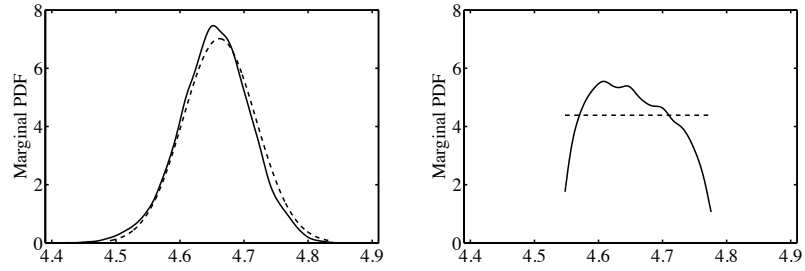

(a) **Pre-exponential coefficient for $O + H_2 \rightleftharpoons H + OH$**

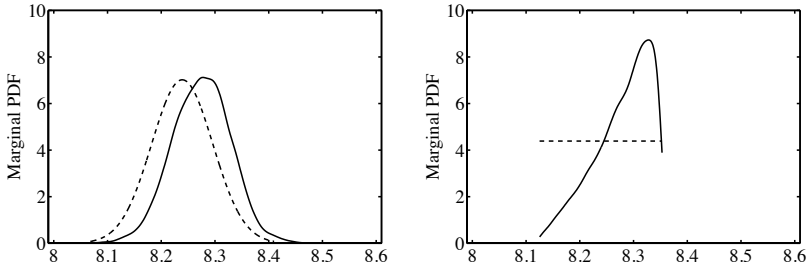

(b) **Pre-exponential coefficient for $OH + H_2 \rightleftharpoons H + H_2O$**

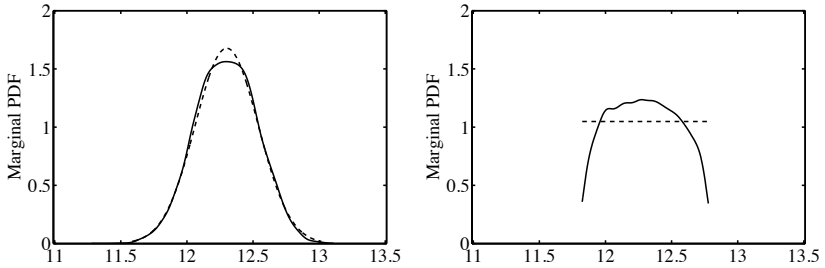

(c) **Pre-exponential coefficient for $H_2O_2 + OH \rightleftharpoons HO_2 + H_2O$**

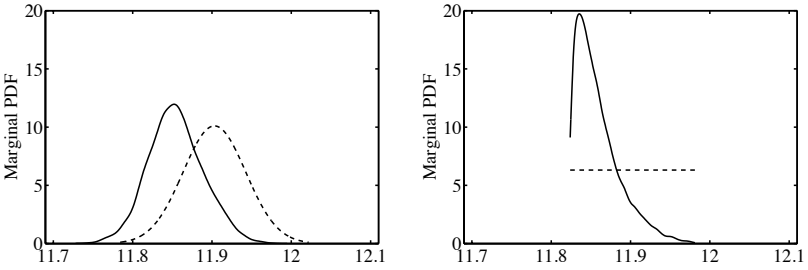

(d) **Pre-exponential coefficient for $CO + OH \rightleftharpoons CO_2 + H$**

Figure 2.2: Prior (dashed) and final (solid) marginal PDFs of Arrhenius pre-exponential parameters for the DM with Gaussian priors (left) and uniform priors (right)

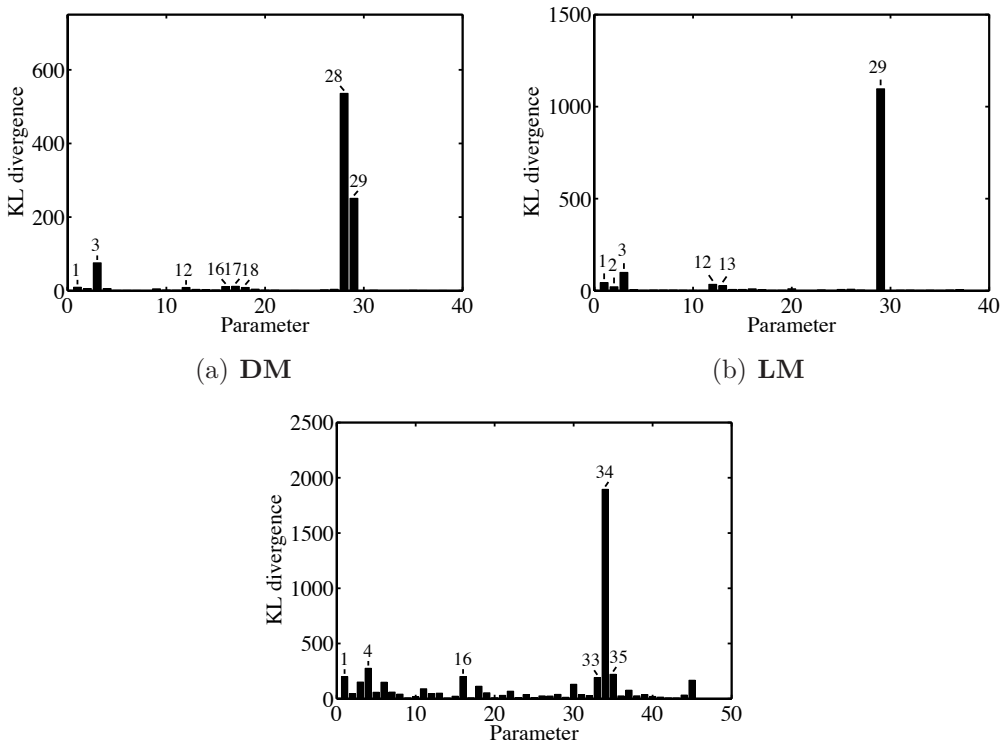

(a) **DM** (b) **LM**

(c) **SM**

Figure 2.3: Kullback-Leibler divergence for every parameter of each model, with the parameters within the top 10% of divergence for each model labeled

While the marginal posterior PDFs are informative, one of the important aspects of UQ methods like the Bayesian approach is the joint calibration of the parameters. In essence, kinetic parameters cannot be tuned individually without degrading performance. The best representation of the experimental data is achieved when all parameters are calibrated simultaneously. The simultaneous calibration of the entire parameter set updates not only individual parameter distributions as described above, but also the correlation between parameters. The posterior joint-PDF of the parameters provides insight as to how a change in a single parameter value changes the other parameters. For instance, Fig. 2.4 shows the two-dimensional joint-PDF of the pre-exponential factor for reactions $HO_2 + O \rightleftharpoons OH + O_2$ and $CO + OH \rightleftharpoons CO_2 + H$. This joint-PDF itself is a marginal PDF obtained from the full multi-dimensional PDF of all calibration parameters. Moreover, the domain of likely values has a complex shape, and is not limited by the presumed-shapes for the prior PDFs. Fig. 2.5 shows slices of a three-dimensional PDF for three parameters from the DM with high KL divergence, parameters 1, 3, and 28 in Fig. 2.3(a). This plot indicates that only a narrow range of parameter values is optimal in reproducing the experimental data.

ADD A PLOT FOR THE PARAMETER WHICH LEARNS THE MOST (HIGHEST KL DIV)!!!

Once the parameters have been calibrated and the samples of the posterior joint PDF obtained, this information can be propagated to determine the uncertainties in predictions of the laminar flame speed. Here, this is illustrated

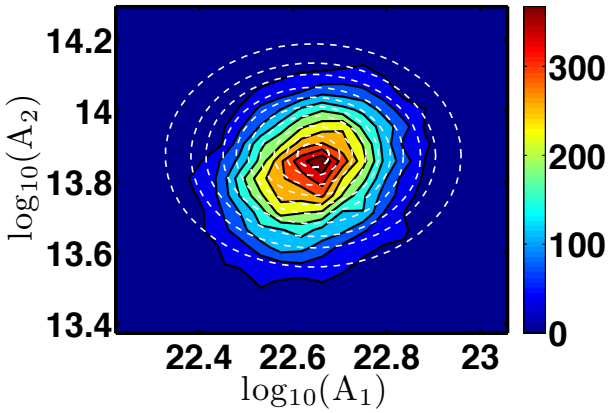

Figure 2.4: Posterior two-dimensional marginal joint PDF for the pre-exponential parameters of reactions H + OH + M $\rightleftharpoons$ H_2O + M (1) and HO_2 + H $\rightleftharpoons$ OH + OH (2) for the DM with Gaussian prior shown as dashed lines

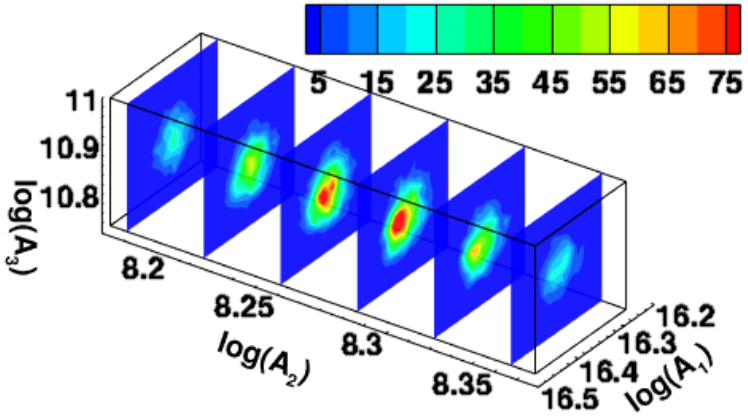

Figure 2.5: Posterior three-dimensional marginal joint PDF for the pre-exponential parameters of reactions H + O_2 $\rightleftharpoons$ O + OH (1), OH + H_2 $\rightleftharpoons$ H_2O + H (2), and CO + OH $\rightleftharpoons$ CO_2 + H (3) for the DM with Gaussian prior

using the Pushed Forward Posterior method. Specifically, for the jth posterior sample of the kinetics model parameters $\boldsymbol{\theta}_j$, the corresponding laminar flame speed $\eta_j = \eta(\boldsymbol{\theta}_j)$ is computed using the chemistry model. In total, 18,432 laminar flame speeds were computed for each condition, leading to an ensemble of flame speed values that can be used to estimate the flame speed distribution. Note that this procedure is equivalent to marginalizing the posterior over the hyperparameter σ and propagating the resulting distribution for the kinetics parameters alone. This allows one to see the uncertainty in the predictions given by just the posterior uncertainty in the calibrated kinetics parameters.

The left side of Fig. 2.6 shows the laminar flame speed computations for two different syngas mixtures at 10 atm pressure. The experimental data for these conditions listed in the top section of Table 2.1 formed a portion of the data set used to calibrate the kinetics models. For comparison, the flame speed computed with the original (nominal) model parameter values and the experimentally observed values are also shown. Since the calibration process produces a PDF for the uncertain parameters, the propagation step produces a PDF for the flame speed results. The plot shows the 95% confidence interval bounding a grey-scale plot of probability density. It is seen that the original models predict higher flame speed compared to the calibrated models for the same conditions. Overall the uncertainty in the predictions is roughly 10% over the range of equivalence ratios considered.

The right side of Fig. 2.6 shows the flame speed computations for an operating pressure of 20 atm, also computed using the Pushed Forward Pos-

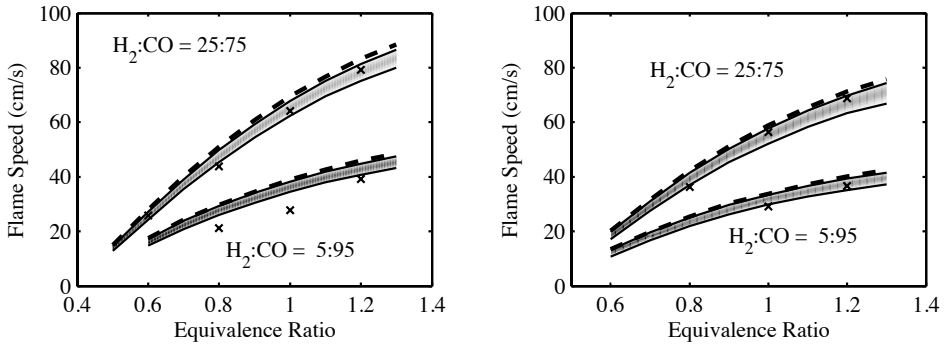

(a) **DM**

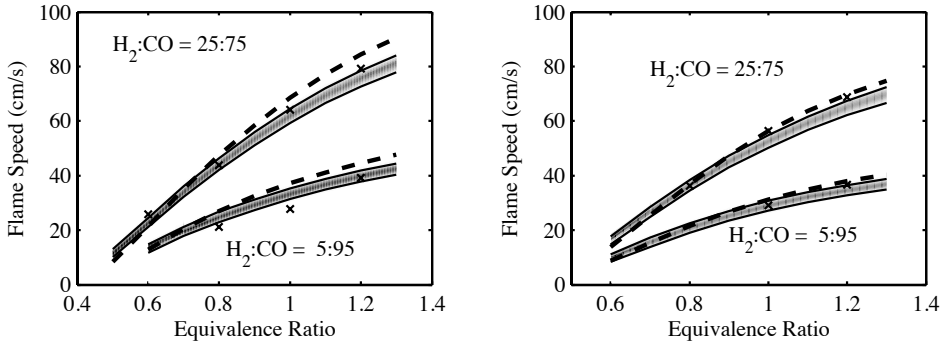

(b) **LM**

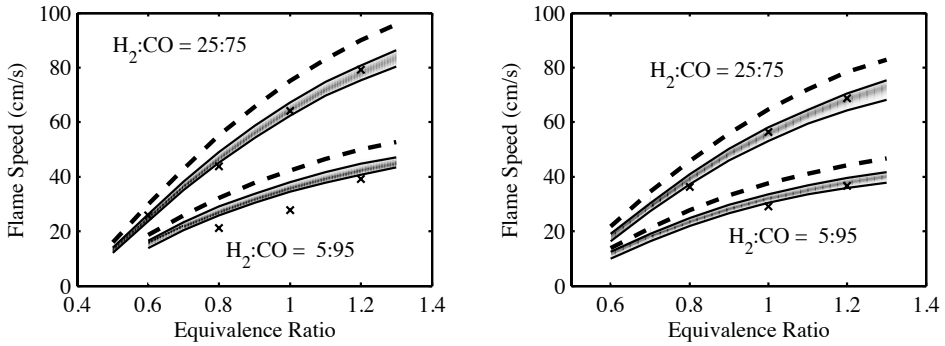

(c) **SM**

Figure 2.6: Flame speed results for (left) 10 atm. and (right) 20 atm., where grey intensity indicates probability between the 95% confidence interval bounds, dotted lines represent results using pre-calibrated parameters, and symbols (x) represent experimental results [53]

terior method. Note that the experimental data for this case is not part of the calibration data set. Thus, this calculation examines the effect of the kinetics parameter uncertainty in extrapolation. The uncertainty in the results increases compared to the 10 atm case, with the 95% confidence interval bands producing a slightly wider spread of flame speeds. Overall, the SM seems to have gained the most in terms of accuracy, with the flame speeds computed from the original model being highly inaccurate for all equivalence ratios considered. The LM produces the least spread in the simulations, indicating lower uncertainty in the parameters considered.

For both the 10 atm and 20 atm computations, the maximum *a posteriori* (MAP) estimates of the flame speed in many cases differ from the experimental measurements. In particular, the 10 atm results with 5:95 H_2:CO ratio show a significant disparity from measurement. Even with the kinetic parameter uncertainty propagated through the simulations, the uncertainty spread of the flame speeds does not capture the experimental results. To further explore the simulation uncertainty, the posterior predictive propagation method has also been employed. In this method, the samples of the hyperparameter σ are used in addition to the kinetics parameters. Specifically, for the jth sample $(\boldsymbol{\theta}_j, \sigma_j)$, the predicted flame speed η_j is implied by the chosen likelihood function. For example, using the additive model from (2.4) leads to

$$\eta_j = \eta(\boldsymbol{\theta}_j) + N(0, \sigma_j^2), \tag{2.13}$$

where $\eta(\boldsymbol{\theta}_j)$ is the flame speed given by the chemical model with kinetics

parameters $\boldsymbol{\theta}_j$ and $N(0, \sigma_j^2)$ is the zero-mean Gaussian with standard deviation σ_j. Thus, in this method, both the parameter uncertainty and the combined model/experimental error term explicitly contribute to the uncertainty of the simulations. With this propagation method, the 95% confidence interval spread encompasses the data. This result can be seen in Fig. 2.7 which shows the posterior predictive flame speed results for 10 atm and 20 atm for all three models. The use of the hyperparameter in the propagation of the predictive 20 atm cases is included to show the effect that the error model could potentially have on those results. However, since the 20 atm data was not used to train the models, σ does not account for the true combined model and experimental error for the 20 atm cases.

Given a properly chosen prior, these results indicate one of two conclusions: either model form error or experimental error must explain the discrepancy. This can also be seen by examining the marginal posterior for σ directly, as shown in Fig. 2.8.

Note that the MAP estimate of σ is a significant fraction of the predicted laminar flame speeds, particularly for lower equivalence ratios. For instance at 20 atm. with equivalence ratio 0.8 and H_2:CO ratio 5:95, the ratio of MAP sigma to the experimental flame speed is approximately 25% for all three models. Even in the best case, the ratio is nearly 4%. This result indicates that the chemical models used here may not be rich enough to reproduce the calibration data. While this could be due to experimental error, given the large magnitude of σ, it seems likely that it is due to model form

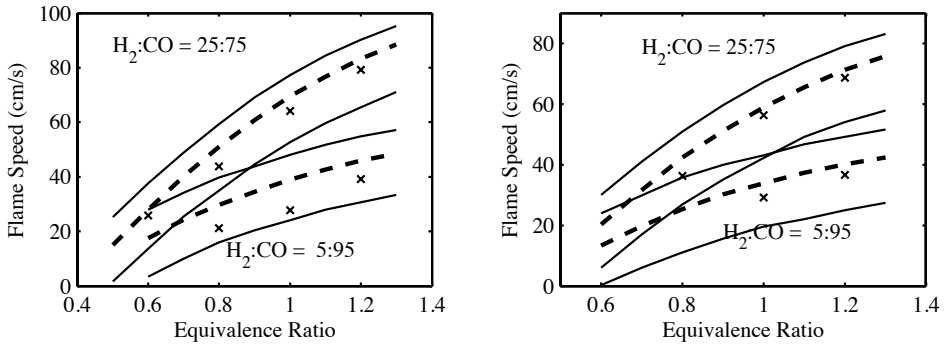

(a) **DM**

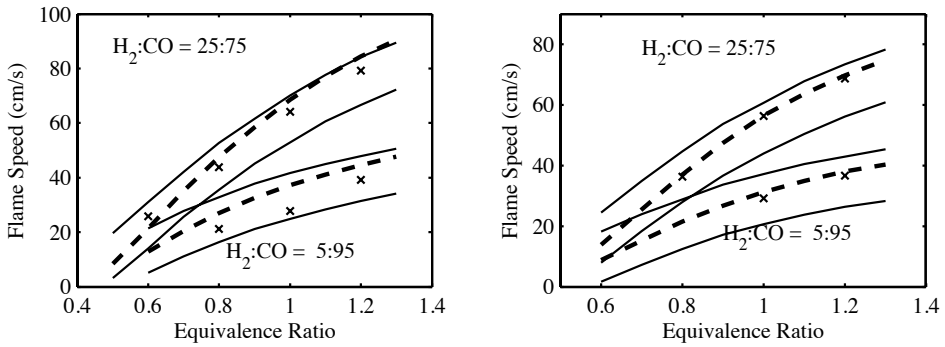

(b) **LM**

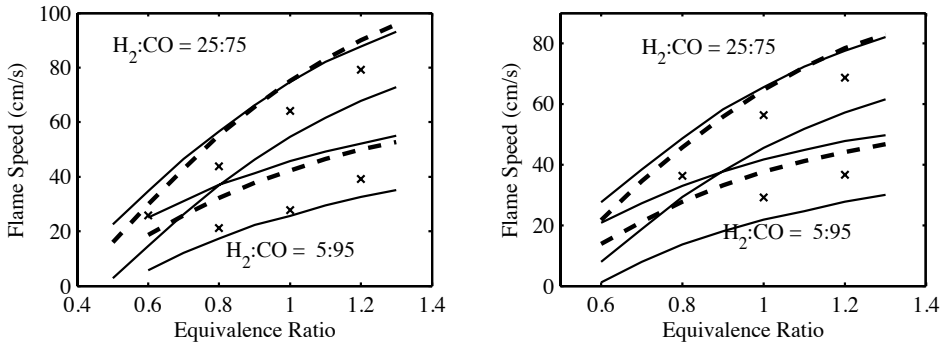

(c) **SM**

Figure 2.7: Posterior predictive flame speed results for (left) 10 atm. and (right) 20 atm., where the solid lines indicate 95% confidence interval bounds, dotted lines represent results using pre-calibrated parameters, and symbols (x) represent experimental results [53]

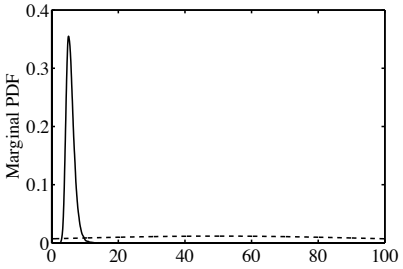

Figure 2.8: Marginal PDF of the error variance hyperparameter σ for the DM with prior shown as a dashed line

error. One way to enrich the current models would be to calibrate additional parameters, such as activation energies, third body efficiencies, and thermodynamic parameters, that have been assumed to be perfectly known in the current calibration.

2.4.2 Bayesian evidence model comparison

The three different syngas chemistry models form a model set. Thus, these models can be compared using the Bayesian framework described in Sec. 2.2.2. Different choices made in setting up the Bayesian calibration will affect the evidence results, including the choice of prior. This dependence is natural given that the evidence depends not only on how well the data is fit but also on how much information is extracted from the data, as measured by the change from prior to posterior. Here, the comparison is made with Gaussian priors used for every parameter in each model. For brevity, we show results only for the additive error likelihood. However, a similar process could be used to compare the chemistry models using different prior and likelihoods

Table 2.2: Log evidence and posterior probability for all three models with additive error form and Gaussian prior

Model	Log evid.	Post. prob.
DM	-61.6433	0.0127
LM	-57.3094	0.9696
SM	-61.3102	0.0177

and/or to compare the different prior and likelihood forms.

Table 2.2 shows the logarithm of the evidence and the posterior probability for each chemistry model. Using this measure, the LM is strongly preferred, with a posterior probability of 0.9696. Recalling the decomposition of the evidence shown in (2.11), this result implies that the LM is able to fit the data well without extracting so much information from the data that the information gain term overwhelms the data fit term. Thus, the LM provides the best combination of data fit and minimal tuning of the parameters from their initial priors for this set of laminar flame speed data. This result does not imply that this kinetics model is the best model, but only that it is the best model of this set at reproducing the data used with minimal fitting.

2.4.3 Prior selection

Common choices for priors when little prior information exists include the uniform prior and Gaussian prior [57]. The uniform prior assigns an equal probability to the parameter over a range of values bounded by a minimum and maximum value. However, care must be taken since the posterior in the case of a uniform prior will not be able to span beyond the minimum or

maximum of the prior. If a region of parameter space is given zero probability by the prior, the posterior will have zero probability in that region as well. The Gaussian prior is a common choice when given information about a parameter's mean and variance. This choice can be motivated by considering Shannon's information entropy, which can be interpreted as a measure of uncertainty of a random variable. One can show that, given only mean and variance, the Gaussian distribution maximizes this entropy [58] relative to a uniform distribution. Similarly, the uniform prior provides the highest information entropy given only a minimum and maximum. Here, the results using uniform priors and Gaussian priors for the DM are compared and discussed.

Figure 2.2 shows sample parameter distributions for the DM given Gaussian priors in the left column and uniform priors in the right column. For the case of reactions O + H_2 $\rightleftharpoons$ H + OH and H_2O_2 + OH $\rightleftharpoons$ HO_2 + H_2O, some information is learned regarding the parameters when the uniform prior is applied. The posteriors have obtained peaks, but are not highly peaked. For reactions OH +H_2 $\rightleftharpoons$ H + H_2O and CO + OH $\rightleftharpoons$ CO_2 + H when applying the uniform prior, the posterior distributions become more highly peaked; however, the distributions also abut against the bounds of the prior distribution. This effect shows that the bounds on the prior can limit the posterior distribution. As mentioned earlier, where the prior distribution has zero probability, the posterior must have zero probability. As a result the posteriors for the parameters in those two reactions are limited and do not reach the parameter values attainable if not bounded. When the Gaussian

prior is applied, the posterior distributions shift for those two pre-exponential coefficients, with the distribution for $CO + OH \rightleftharpoons CO_2 + H$ becoming slightly more peaked. Most importantly the support of the Gaussian priors allows the posterior distributions to attain the distributions as informed by the data.

2.4.4 Error model comparison

The Bayesian methodology provides for the utilization of different error models, which are incorporated in the likelihood function. Prior knowledge regarding how the error will develop for a particular problem can be integrated into the form of the likelihood. In the results above in Sec. 2.4.1, the additive error model has been used. In the following, the additive and multiplicative error models, detailed in Sec. 2.2.1, are compared for the LM.

The different error models result in different posterior parameter distributions. Samples of the one-dimensional marginal distributions are plotted in Fig. 2.9. For some of the parameters, in particular the coefficient for $HO_2 + H \rightleftharpoons H_2 + O_2$, the multiplicative error model leads to a more peaked distribution with a different MAP estimate.

Furthermore, the propagated results for the multiplicative error form display a broadening of the flame speed uncertainty in comparison with the additive model as seen in Fig. 2.10. The multiplicative treatment of the error model, although resulting in less certainty in the results, is not necessarily a poor choice of error model. A reduced uncertainty does not imply that the additive error model is the correct model for a particular application.

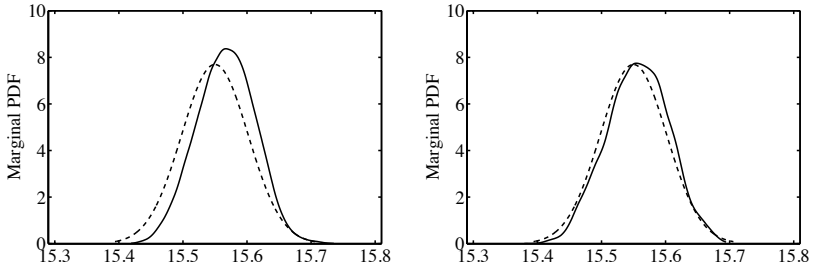

(a) **Pre-exponential coefficient for $H + O_2 \rightleftharpoons O + OH$**

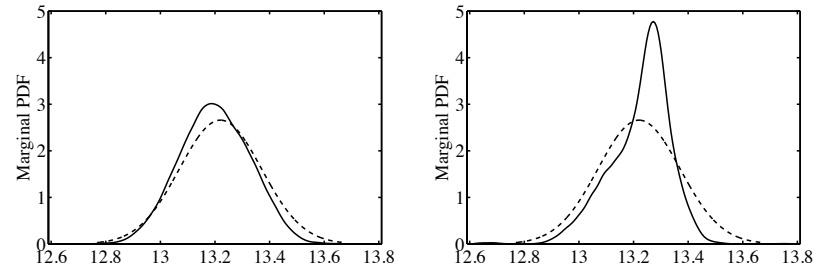

(b) **Pre-exponential coefficient for $HO_2 + H \rightleftharpoons H_2 + O_2$**

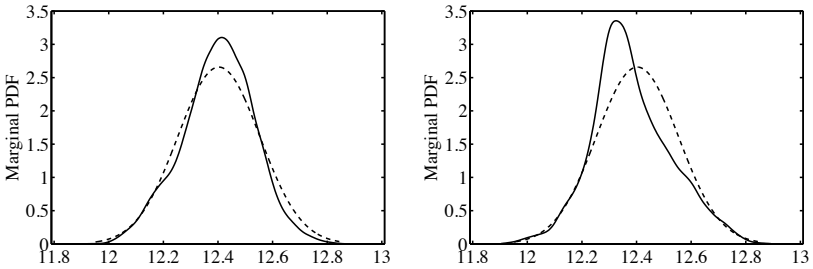

(c) **Pre-exponential coefficient for $CO + O_2 \rightleftharpoons CO_2 + O$**

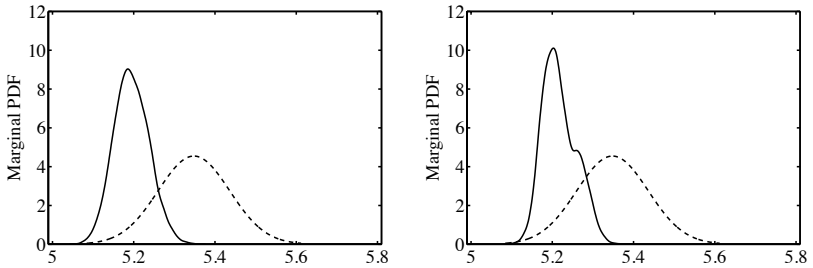

(d) **Pre-exponential coefficient for $CO + OH \rightleftharpoons CO_2 + H$**

Figure 2.9: Prior and final marginal PDFs of Arrhenius pre-exponential parameters for the LM with (left) additive error and (right) multiplicative error.

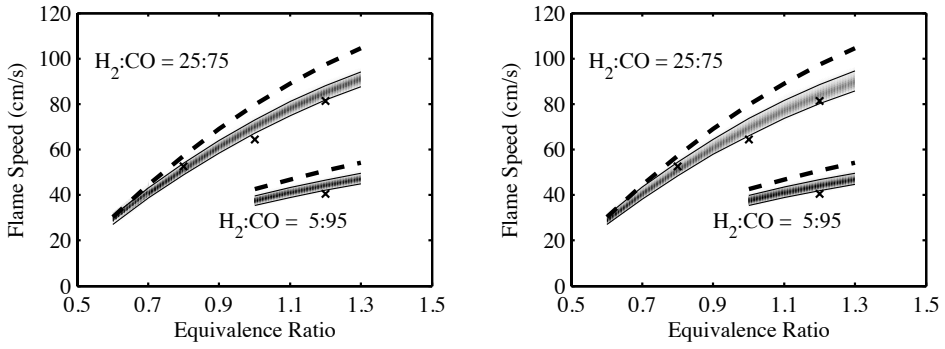

(a) **5 atm.**

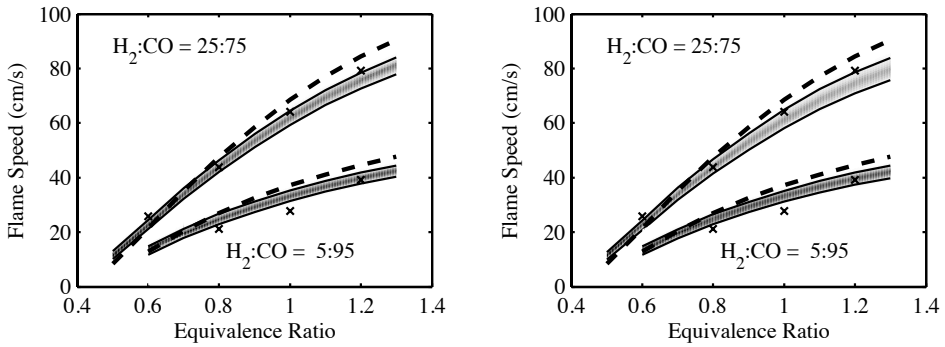

(b) **10 atm.**

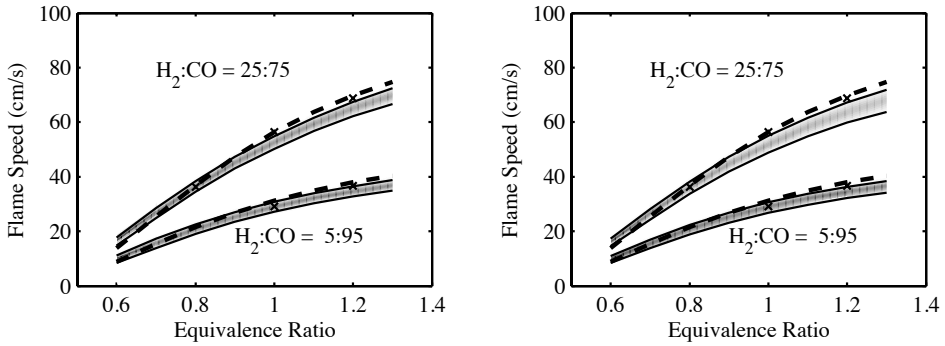

(c) **20 atm.**

Figure 2.10: Flame speed results for the LM with (left) additive error and (right) multiplicative error, where grey intensity indicates probability between the 95% confidence interval bounds, dotted lines represent results using pre-calibrated parameters, and symbols (x) represent experimental results [53]

The additive error model weights all model error equally amongst the separate experimental conditions. Thus, for conditions which result in flame speeds on the order of 100 cms, a relative error of say 5% will affect the model error term more drastically than conditions with a flame speed on the order of 10 cms. With a multiplicative model error term, which scales with the magnitude of the result, the error at each condition is weighted more naturally so that the conditions with higher flame speeds do not dominate the error from conditions with lower flame speeds. Such a treatment is not unknown in combustion applications, and it has been shown to be beneficial when modeling chemical kinetics [31].

Table 2.3 shows the logarithm of the evidence and the posterior probability for the Bayesian update using additive and multiplicative error models. Much like comparing different kinetics models, the evidence may be used to compare results from the same kinetics model, but with different applied error models. The two cases with different applied error models then become two different model classes within the set of models. Using the evidence measure, the multiplicative error model is strongly preferred, with a posterior probability of essentially 1. Similar to the result for the kinetics model comparison, this result implies that the multiplicative error model provides the best combination of data fit and minimal tuning of the parameters for this set of laminar flame speed data.

Other error models could potentially provide a better match. Parameterizing an error model proportional to some experimental parameters such

Table 2.3: Log evidence and posterior probability for the LM with additive and multiplicative error forms and Gaussian prior

Error Model	Log evid.	Post. prob.
Additive	-57.31	0.0
Multiplicative	6.236	1.0

as pressure may prove to fit the data better. The downside is that these parametric relations may not be known *a priori* and could require a significant number of parameters.

2.5 MUM-PCE and Bayesian Approach Comparison Results

The method of Sheen and Wang [14, 21, 22], referred to as MUM-PCE, is an interesting technique that combines aspects of the Bayesian formulation with regression-type error minimization to produce updated parameters. In this section, the specific assumptions made in this technique are analyzed in order to better understand the relative importance of model and error forms on the calibration process. In Appendix B, it is shown that the MUM-PCE is a simplified Bayesian technique that utilizes the following simplifications: 1) the target model is replaced by a surrogate model, 2) the surrogate model is assumed to be linear with regard to the parameters, 3) the error in the predictions appears only from experimental uncertainty. In other words, if the experimental error were to reduce to zero, the parameters would be tuned to capture the experimental data with no resultant uncertainty in either the parameters or simulation results.

During the parameter update process with MUM-PCE, a surrogate model, the quadratic response surface model, is assumed for the flame speed. This assumption varies from the direct use of the target model in the Bayesian methodology. Furthermore, the surrogate model is linearized with respect to the model parameters when determining the covariance between parameters. This represents a further step from the Bayesian method. Next, treating the error in the parameter update process as strictly from experimental uncertainty neglects any error inherent in the kinetics model itself. This assumption applied to the Bayesian methodology is equivalent to assuming an additive error in which no additional error variance hyperparameter is employed. Applying these assumptions to the sampling-based Bayesian method results in nearly identical results in comparison to MUM-PCE results. Removing those assumptions one at a time reveals how the assumptions affect the outcome.

Applying the above described assumptions incrementally leads to a set of tests of the modified Bayesian method. These tests are categorized by choice of target model, linearized response surface, full response surface, or true flame speed model, and by choice of model error, either additive error with fixed $\sigma = \sigma_{obs} = 2.0$ or additive error with the inferred error variance hyperparameter. The following sections detail the effects of removing the Sheen and Wang assumptions from the modified sampling-based Bayesian method. These test cases all were performed using a single kinetics model, the DM, for brevity. Section 2.5.1 describes the posterior distributions which result from the incremental testing, and Sec. 2.5.2 describes the resultant flame speed

distributions from the uncertainty propagation.

2.5.1 Marginal parameter distributions

Figure 2.11 shows two-dimensional plots of the CO + OH $\rightleftharpoons$ CO_2 + H and of the duplicate CO + OH $\rightleftharpoons$ CO_2 + H pre-exponential parameters for the different options. The first reaction is referenced as R1 with parameter A_1, and the second reaction is referenced as R2 with parameter A_2. When the Bayesian update is performed with the linearized response surface and fixed additive error, hereafter referred to as the baseline and shown in plots labeled with (a), the solution closely matches that of the MUM-PCE method. With the modification to the full response surface shown in the plots labeled (c), the solution changes from the baseline. While the parameter MAP values remain essentially the same, the shape, size, and alignment of the probability contours change. These changes can manifest themselves as a modification of the multivariate Gaussian covariance, as well as a shift away from a multivariate Gaussian to an arbitrary distribution. Such an outcome shows that the use of linearized response surfaces affects the shape and size of the probability surfaces, here two-dimensional marginal distribution contours.

When the error standard deviation hyperparameter is inferred, i.e. updated along with the kinetics parameters in the Bayesian update, the shape, size, alignment, and location of the probability contours changes. These changes are shown in plots labeled (b) and (d). The MAP parameter values show a significant shift and the sizes of the probability contours show a

significant increase. The MAP parameter value shift is due to the shift in the region of the error parameter space. In Fig. 2.12 showing kinetics parameters versus the error term, the corresponding MAP kinetics parameter values for each error value are plotted in dashes. Following the dashed line towards an error of $\sigma_{obs} = 2.0$ shows the shift in the MAP kinetic parameter value, and thus that the results from error of $\sigma = 2.0$ can be extrapolated as a solution for the parameter space with the inferred error term hyperparameter. Regarding the expansion of the probability contours, including the error model standard deviation as a hyperparameter to be inferred reduces the certainty with which the kinetics parameters are determined. The modeled flame speed results vary from the corresponding experimental results with a standard deviation greater than that assumed for the MUM-PCE solution. With the MUM-PCE assumed experimental error standard deviation, the kinetics parameters are determined with more certainty than the modeled results themselves indicate. Thus, the kinetics parameters are determined with more certainty than warranted.

2.5.2 Propagated flame speed distributions

Figure 2.13 displays the flame speed propagation results. The results for the Bayesian cases vary when switching from fixed to inferred error standard deviation. With the linearized response surface and inferred error standard deviation shown in Fig. 2.13(c), the uncertainty is greater as compared with fixed error standard deviation shown in Fig. 2.13(b). Similar results are displayed with the quadratic response surface shown in Figs. 2.13(e) and 2.13(d).

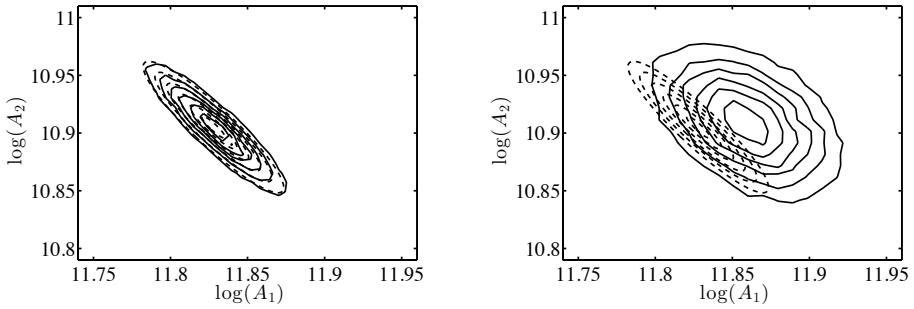

(a) **Bayesian with linearized response surface and error term specified**

(b) **Bayesian with linearized response surface and error term inferred**

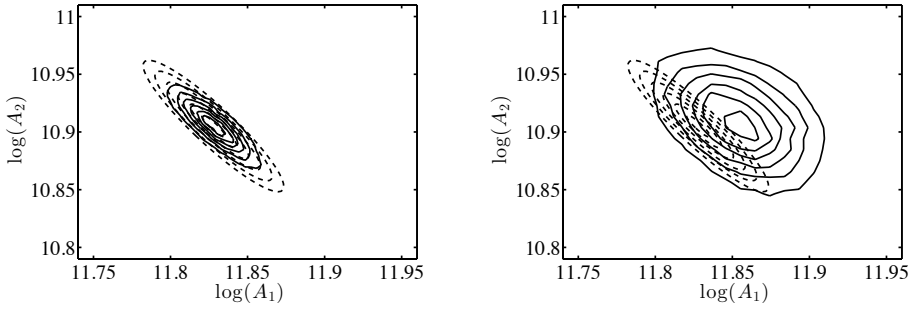

(c) **Bayesian with quadratic response surface and error term specified**

(d) **Bayesian with quadratic response surface and error term inferred**

Figure 2.11: Bayesian posterior (solid) and MUM-PCE posterior (dashed) two-dimensional marginal PDFs of R1 and R2 pre-exponential coefficient A for the DM with two parameters varied

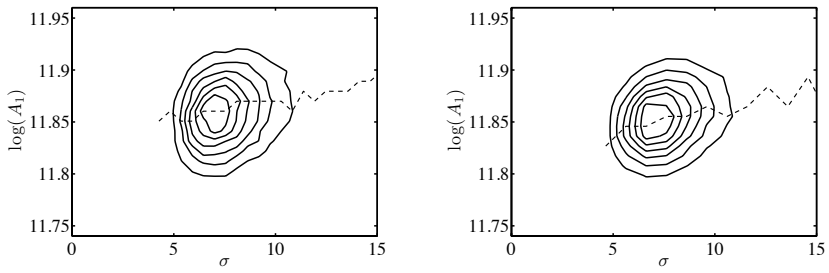

(a) **Bayesian with linearized response surface and error term inferred**

(b) **Bayesian with quadratic response surface and error term inferred**

Figure 2.12: Bayesian posterior (solid) two-dimensional marginal PDFs of the error standard deviation and R1 pre-exponential coefficient A for the DM with two parameters varied, with a line of MAP value (dashed)

Such results imply one of two conclusions. First, using the error model standard deviation as a hyperparameter in the inference problem leads to larger uncertainty in the kinetics parameters and consequently the flame speed solutions. Second, specifying the standard deviation of the error term unnecessarily increases certainty in the kinetics parameters and consequently the flame speed solutions. This second conclusion should apply generally. Specifying the standard deviation of the error term, in essence specifying the model and experimental error spread, will lead to an artificial sense of certainty when these error spreads are not known *a priori*.

The flame speed results for the full Bayesian case shown in Fig. 2.13(f) exhibit a closer match to the experimental data than the response surface cases with inferred error σ. This result indicates that calibration and propagation with the true rather than surrogate model likely provides more accurate flame speed results in the parameter space regions farther from the nominal

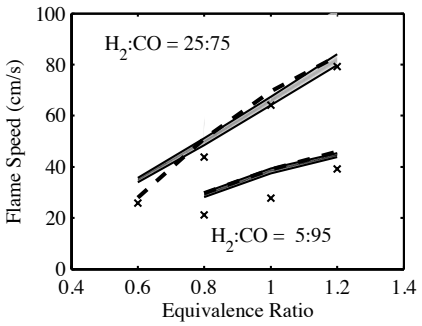

(a) **R1 and R2 varied, MUMPCE**

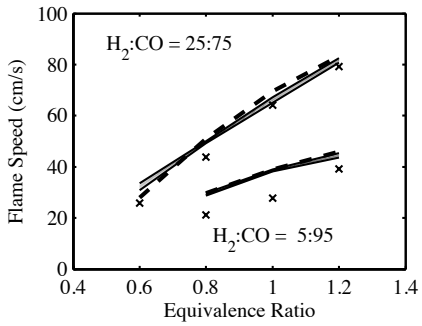

(b) **R1 and R2 varied, Linearized Response Surfaces with σ specified**

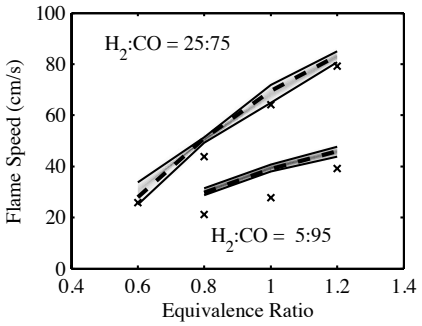

(c) **R1 and R2 varied, Linearized Response Surfaces with σ inferred**

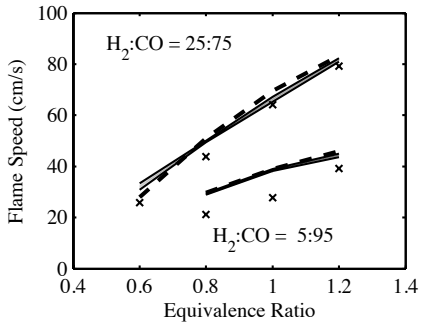

(d) **R1 and R2 varied, Quadratic Response Surfaces with σ specified**

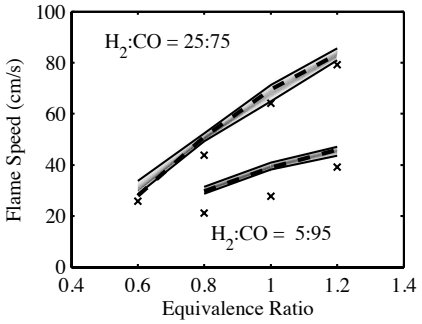

(e) **R1 and R2 varied, Quadratic Response Surfaces with σ inferred**

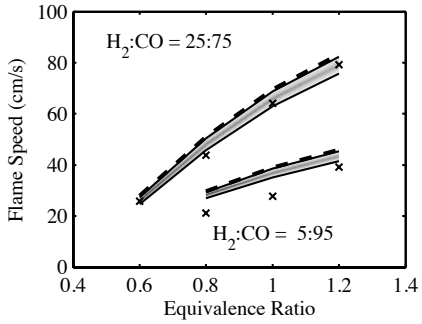

(f) **R1 and R2 varied, full Bayesian**

Figure 2.13: Flame speed results at 10 atm. for the Davis et al. [13] model, where grey intensity indicates probability between the 95% confidence interval bounds, dotted lines represent results using the nominal parameters, and symbols (x) represent experimental results [53]

Table 2.4: Mean and RMS error ε between the response surface and Chemkin-determined flame speeds for the experimental conditions which lead to the largest and smallest error

Expt	Mean ε	RMS ε	Max ε	RS MAP ε	Bayesian MAP ε
8	2.2	2.1	10.8	5.1	2.1
9	0.1	0.1	0.2	0.1	0.0

parameter values where the linearization assumptions break down. Table 2.4 lists the mean, RMS, and maximum error between the response surface and Chemkin-determined flame speeds for the two experimental conditions leading to the largest and smallest error. The table lists those errors for flame speeds determined from parameter values chosen on an evenly spaced grid within the parameter space bounded by two standard deviations from the mean parameter values. Additionally, the table lists the error at the MAP estimate for the parameters. Although for some experimental conditions the error is low, for others the error reaches magnitudes of more than 10 cm/s near the boundaries of the response surface. Looking at the MAP values, the response surface errors reach a magnitude as high as 5.1 cm/s. Such errors potentially can lead to errors in the determination of the nominal parameter values and parameter covariances.

2.6 Conclusions

Bayesian methods provide a powerful framework for quantifying uncertainty in syngas combustion applications. Bayesian calibration, given a set of experimental data to compare against, both improves calibration of the syngas

chemistry models as well as provides updated distributions for parameters of those models. Those distributions can then be propagated forward into simulations of laminar flame speed to determine the uncertainty in their predictions. The same framework can also be used to rank a set of candidate models.

The application of this approach to existing experimental data and a select group of chemistry models was conducted here. It was found that the model by Sun [53] undergoes significant changes in order to capture the experimental data. All three models showed some increase to uncertainty in the results at higher pressures, even when calibrated using experimental data at 10 atm, confirming prior analyses that suggest increased sensitivity of results to model coefficients at higher pressures. The functional form and support of the prior PDF was found to have an important effect on the calibration results. Specifically, the bounds on the uniform prior set based on previous uncertainty estimates can be too narrow to allow a good calibration. Additionally, the error model affects the Bayesian calibration and forms an integral part of the calibration process.

MUM-PCE also has been applied to the same syngas flame speed simulations. MUM-PCE has been shown to be a simplified version of the Bayesian method after the application of several assumptions. Furthermore, in comparison with corresponding Bayesian results, the effects of those assumptions are shown to significantly affect the update of the parameter hypervolume shape and parameter distributions, as predicted by Data Collaboration analysis [34]. This indicates that modeling of uncertainty itself will alter the results.

The Bayesian calibration process provides a rigorous mechanism for incorporating new data in order to improve existing models. The availability of such tools is important for engine design for two different reasons. The use of uncertainty estimates provides a better characterization of the state of knowledge, and allows for robust decision making. Further, these estimates also provide information about the most important models and model parameters, allowing better allocation of limited resources.

Chapter 3

Adjoint-based sensitivity analysis

3.1 Introduction

Simulation of combustion often involves hundreds of parameters, most of which arise from the chemistry mechanism used. In order to determine the predictive value of such simulations, it is useful to know the dependence of the prediction quantities on the parameters that constitute the various models. This is obtained by sensitivity, which is the derivative of the quantity of interest (QoI) to any parameter, with all other parameters held constant. In this sense, a ranking of the most sensitive parameters informs the user of the most critical processes that control the prediction. This information could be used to develop better experiments [20, 59], optimize rate parameters [13, 14], or for mechanism reduction [59–61] where the least sensitive parameters point to pathways that do not contribute significantly to the target prediction.

The QoI w.r.t which the sensitivity is obtained could be a measured value (such as laminar flame speed) or an output that is the main outcome of conducting the simulation. Typically, a small number of prediction quantities are output from each simulation but there will be a very large set of parameters. For instance, in 2D laminar flames, there might be available temperature

measurements (QoIs) at select locations in the domain. Depending on the fuel used, the number of parameters used to simulate these QoIs might be very large. The most direct approach to finding sensitivities is to differentiate the governing equations with respect to the parameters, and find the QoI sensitivity as follows

$$\frac{dJ}{d\alpha} = \frac{\partial J}{\partial \alpha} + \sum_{i=1}^{N} \frac{\partial J}{\partial \phi_i} \frac{\partial \phi_i}{\partial \alpha}, \tag{3.1}$$

where J is the QoI, ϕ_i is the i-th variable solved using the governing equations (i.e., velocity, species compositions, etc.), N is the number of independent variables that determine the state of the system, and α is the parameter w.r.t which sensitivity is needed. In the above equation, the term $\frac{\partial \phi_i}{\partial \alpha}$ is the most computationally intensive part, since for a three-dimensional flow configuration this will involve solving a partial differential equation. It is to be expected that the cost of solving this equation is commensurate with the original transport equation for the quantity ϕ_i.

In general, the number of independent variables for a three-dimensional system is equal to $N_s + 5$, where N_s is the number of species. If we assume that the number of chemical reactions scale as $5N_s$ [62], the number of parameters associated with chemical reactions alone would be of the order of $15N_s$, leading to $15(N_s + 5)N_s$ additional equations to determine the first order sensitivities for the QoIs. These additional equations will impose considerable computational expense, especially when the chemistry model is detailed with many hundreds of species.

Sensitivity analysis has been used predominantly with homogeneous or

one-dimensional flows, where the cost of solving the sensitivity equations is relatively low. For instance, the sensitivity of the laminar flame speed or ignition delay time to reaction rate parameters is commonly used to determine the important reactions [3, 13, 23–25]. Beyond these single resultant quantities, sensitivity analyses have also been used to study the one-dimensional spatial dependence of flames [28, 29]. In general, sensitivity analysis is limited to simple flame configurations due to the computational cost. An alternative approach is based on the response surface method [63], for which the output QoIs are expressed as polynomial functions of the parameters, or the high-dimensional model representation method [64, 65], for which the output QoIs are expressed as combinations of high-order orthogonal functions. The functions themselves are obtained by performing a few full-scale computations and fitting the results. While this approach is cost effective, it drastically simplifies the nonlinearity of the problem, and removes the spatial dependance of sensitivity. Nevertheless, this method has been used to develop local and global sensitivity analysis tools [31, 66].

An alternate approach that is proposed here is based on the adjoint technique for obtaining sensitivities. This method is particularly powerful when the number of QoIs is limited and the number of relevant model parameters is large. The adjoint method introduces an additional number of equations proportional to $(N_s + 5)N_{QoI}$ for a three dimensional simulation regardless of the number of parameters in the models. The application of adjoint methods, although common in the realm of aerospace systems, has not

been common for combustion. Previous aerospace applications include aerodynamic shape optimization [67–72], flow control over bodies and in channels [73, 74], reduction of acoustic noise production [75, 76], and flow instability [77]. Adjoint methods have also been used in the realm of chemical kinetics as it relates to atmospheric pollution. Sensitivity of output variables to kinetics parameters has been derived, implemented, and subsequently applied to air pollution models [78–80].

In this chapter, the adjoint equations for laminar reacting flow are derived. The implementation of these equations and verification using one-dimensional test cases are shown. Finally, a two-dimensional laminar flame is simulated, and the sensitivities of two test QoIs to chemistry model parameters are computed.

3.2 Methodology

Desired quantities to measure or calculate from combustion experiments and simulations, here referred to as Quantities of Interest (QoIs), can include various values such as flame speed, flame length, peak temperature, pollutant concentration, as well as many others. The QoIs can be sensitive to many properties of the flow including temperature, pressure, or species concentrations. Due to the dependence of the flow properties on modeling choices, the QoIs are generally sensitive to the model parameters. In the case of reacting flows, models and parameters associated with chemical reactions critically affect the QoIs.

The adjoint equations are defined based on two inputs. It is necessary to define the QoIs, which are taken to be quantities that are spatially averaged over a section of the flow domain. This could represent, for instance, a measurement location or a critical part of the flow (such as the flame tip). Additionally, the governing equations for the flow, termed primal equations, are needed. The adjoint equations are derived using a variational approach. Below, the primal problem, the dual or adjoint problem, and the evaluation of the sensitivities based on the dual solution are discussed.

3.2.1 Primal Problem

The primal problem involves the simulation of the laminar flame itself. Since this study focuses on a low-speed laminar flame, the primal problem consists of laminar low-Mach number variable density reacting flow. As a result, the reacting flow is governed by the variable density Navier-Stokes (NS), scalar mass fraction, and enthalpy equations. The governing equations are written in the following form:

$$\frac{\partial \rho}{\partial t} + \frac{\partial \rho u_i}{\partial x_i} = 0 \tag{3.2}$$

$$\rho \frac{\partial u_i}{\partial t} + \rho u_j \frac{\partial u_i}{\partial x_j} + \frac{\partial p}{\partial x_j}\delta_{ji} - \frac{\partial \tau_{ji}}{\partial x_j} = 0 \tag{3.3}$$

$$\rho \frac{\partial h_s}{\partial t} + \rho u_j \frac{\partial h_s}{\partial x_j} - \frac{\partial}{\partial x_j}\left(\rho \alpha \frac{\partial h_s}{\partial x_j}\right) = \omega_{hs} \tag{3.4}$$

$$\rho \frac{\partial Y_k}{\partial t} + \rho u_j \frac{\partial Y_k}{\partial x_j} - \frac{\partial}{\partial x_j}\left(\rho D_k \frac{\partial Y_k}{\partial x_j}\right) = \omega_{Y_k} \tag{3.5}$$

where u_i is the velocity, p is the pressure, h_s is the sensible enthalpy, α is the thermal diffusivity, ω_{hs} is the chemical source term for enthalpy, Y_k is the mass

fraction for species k, D_k is the mixture-averaged diffusivity for species k, and ω_{Y_k} is the source term for species k. The viscous stress tensor τ_{ij} is given by $\mu\left(\frac{\partial u_i}{\partial x_j}+\frac{\partial u_j}{\partial x_i}-\frac{2}{3}\frac{\partial u_k}{\partial x_k}\delta_{ij}\right)$. Only steady state problems are considered here, which would remove the time derivative in the governing equations. They are retained here since the solution procedure involves evolving these unsteady equations in time until steady state is reached. For simplicity, the Lewis number is assumed to be one and the transport properties are assumed to be constant. Note that these assumptions are not limitations of the method, but are made here only to reduce the complexity of the equations and facilitate discussion. In the low-Mach number formulation, pressure is split into two terms, the fluctuating mechanical pressure p and the thermodynamic pressure P^0. The thermodynamic pressure is assumed constant, while the mechanical pressure is allowed to vary and enforces the continuity equation [81]. The density and temperature T are determined from the following relations,

$$P^0 = \rho RT, \text{ and } h = C_p T. \tag{3.6}$$

The gas constant R and specific heat C_p are also assumed to be constant. Note that these assumptions are stringent and are not expected to hold for practical flames. In the application presented in Section 3.4, the gas constant varies between approximately 15 and 29 between the fuel jet and the coflow. For the stated objective of demonstrating the adjoint approach, these approximations are taken to be reasonable.

3.2.2 Dual Problem

To determine the sensitivity of the QoIs to model parameters, the adjoint solution is required. Commonly referred to as the dual problem, the adjoint equations are solved for a specific QoI. In this work, the QoI, $\mathcal{J}$, is assumed to be the domain-wide integration of the scalar function, g, which is a function of the primal variables $\boldsymbol{U} = [p', u_i, h_s, Y_k]$:

$$\mathcal{J}(\boldsymbol{U}) \equiv \int_{\Omega} g(\boldsymbol{U}) d\mathbf{x}. \tag{3.7}$$

Starting with the defined QoI, the adjoint equations can be derived through the use of Lagrange multipliers as shown in Appendix C. The result of this derivation is the following set of adjoint equations corresponding to the incompressible steady state reacting flow detailed in Section 3.2.1:

$$\frac{\partial \varphi_{u_i}}{\partial x_i} = 0, \tag{3.8}$$

$$\begin{aligned} \rho\frac{\partial \varphi_{u_i}}{\partial t} - \rho u_j \frac{\partial \varphi_{u_i}}{\partial x_j} - \frac{\partial \varphi_{u_j}}{\partial x_i}\rho u_j - \frac{\partial}{\partial x_j}\left(\mu\left(\frac{\partial \varphi_{u_j}}{\partial x_i} + \frac{\partial \varphi_{u_i}}{\partial x_j}\right)\right) \\ + \rho\varphi_h \frac{\partial h}{\partial x_i} + \rho\sum_{k=1}^{N} \varphi_{Y_k}\frac{\partial Y_k}{\partial x_i} - \rho\frac{\partial \varphi_p}{\partial x_i} = 0, \end{aligned} \tag{3.9}$$

$$\begin{aligned} \rho\frac{\partial \varphi_h}{\partial t} - \rho u_j \frac{\partial \varphi_h}{\partial x_j} - \frac{\partial}{\partial x_j}\left(\rho\alpha\frac{\partial \varphi_h}{\partial x_j}\right) - \frac{1}{h}\rho\alpha\frac{\partial h}{\partial x_j}\frac{\partial \varphi_h}{\partial x_j} \\ - \frac{1}{h}\rho u_j \frac{\partial h}{\partial x_j}\varphi_h - \frac{1}{h}\rho\sum_{i=1}^{N} D_i \frac{\partial Y_i}{\partial x_j}\frac{\partial \varphi_{Y_i}}{\partial x_j} + \frac{1}{h}\rho u_j \frac{\partial \varphi_p}{\partial x_j} \\ + \frac{1}{h}\rho u_j \frac{\partial \varphi_{u_i}}{\partial x_j}u_i - \frac{1}{h}\sum_{i=1}^{N}\rho u_j \frac{\partial Y_i}{\partial x_j}\varphi_{Y_i} = \frac{\partial g}{\partial h} + \frac{\partial \omega_h}{\partial h}\varphi_h + \sum_{i=1}^{N}\frac{\partial \omega_{Y_i}}{\partial h}\varphi_{Y_i}, \end{aligned} \tag{3.10}$$

$$\rho\frac{\partial\varphi_{Y_k}}{\partial t}-\rho u_j\frac{\partial\varphi_{Y_k}}{\partial x_j}-\frac{\partial}{\partial x_j}\left(\rho D_k\frac{\partial\varphi_{Y_k}}{\partial x_j}\right)=\frac{\partial g}{\partial Y_k}+\frac{\partial\omega_h}{\partial Y_k}\varphi_h+\sum_{i=1}^{N}\frac{\partial\omega_{Y_i}}{\partial Y_k}\varphi_{Y_i}, \quad (3.11)$$

where $\varphi_i, i = \{p, u_j, h, Y_k\}$ refers to the adjoint variables. The number of adjoint variables equals the number of primal equations.

The adjoint equations exhibit certain peculiar properties that merit further discussion. The adjoint continuity equation (Eq. 3.8) does not contain density and looks identical to the primal continuity equation for a constant density flow. Although the adjoint variables corresponding to the velocity equations are not similar in nature to the velocity vector, the presence of the continuity-type constraint is important in the numerical implementation (Sec. 3.2.4). The adjoint momentum, enthalpy, and species equations contain a convective term that has a negative sign which is different than the primal counterpart. This negative convection term leads to information propagation that is backwards with regard to the primal solution. For instance, this could be treated as information flowing from the outflow to the inflow. If the flow were unsteady, the information has to be propagated back in time in order to maintain numerical stability. In this particular case, the primal solutions are time invariant and as such pose no numerical issues. Finally, the different adjoint equations are coupled in a unique way. The species adjoint equations do not contain the velocity or pressure adjoint variable. Note that in the absence of chemical source terms (inert species), the species adjoint equations will be independent of the enthalpy adjoint as well. On the other hand, the species adjoint is present in all the other adjoint equations. This is different

from the primal problem, where the species influence on the velocity equations is more indirect through the density changes.

3.2.3 Sensitivity

The adjoint solution is the intermediate step in the computation of the sensitivity of the QoI to the model parameters. The primal solution $\boldsymbol{U}$ is a function of the model parameters $\boldsymbol{\theta}$, which leads to the following relation for the sensitivity of the QoI w.r.t $\boldsymbol{\theta}$:

$$\frac{d\mathcal{J}(\boldsymbol{U}(\boldsymbol{\theta});\boldsymbol{\theta})}{d\boldsymbol{\theta}} = \frac{\partial \mathcal{J}}{\partial \boldsymbol{\theta}} + \frac{\partial \mathcal{J}}{\partial \boldsymbol{U}}\frac{\partial \boldsymbol{U}}{\partial \boldsymbol{\theta}}. \tag{3.12}$$

In the cases in which $\mathcal{J}$ has no explicit dependence on $\boldsymbol{\theta}$, $\partial\mathcal{J}/\partial\boldsymbol{\theta}$ is zero, and therefore

$$\frac{d\mathcal{J}(\boldsymbol{U}(\boldsymbol{\theta}))}{d\boldsymbol{\theta}} = \frac{\partial \mathcal{J}}{\partial \boldsymbol{U}}\frac{\partial \boldsymbol{U}}{\partial \boldsymbol{\theta}}. \tag{3.13}$$

Next, define the residual form of the governing equations (3.2-3.5) as $\boldsymbol{R}(\boldsymbol{U};\boldsymbol{\theta}) = \mathbf{0}$, as in the derivation of the adjoint equations in Appendix C. Starting from this definition, the Jacobian of $\boldsymbol{R}$ is written $\boldsymbol{R}'[\boldsymbol{U}]$. From the adjoint derivation,

$$\frac{\partial \mathcal{J}}{\partial \boldsymbol{U}} = \int_\Omega \boldsymbol{\varphi}^T \boldsymbol{R}'[\boldsymbol{U}] d\mathbf{x}, \tag{3.14}$$

where $\boldsymbol{\varphi} = [\varphi_p, \varphi_{u_i}, \varphi_{h_s}, \varphi_{Y_k}]$ is the column vector of adjoint variables. Then, taking the total derivative of $\boldsymbol{R}$ with respect to the parameter θ and rearranging gives the following:

$$\frac{\partial \boldsymbol{U}}{\partial \boldsymbol{\theta}} = -\boldsymbol{R}'[\boldsymbol{U}]^{-1}\frac{\partial \boldsymbol{R}}{\partial \boldsymbol{\theta}}, \tag{3.15}$$

for which $\frac{\partial \boldsymbol{R}}{\partial \boldsymbol{\theta}}$ is the set of partial derivatives of the residual form of the equations to the parameters $\boldsymbol{\theta}$. Finally, substituting the above relations into (3.13) leads to the following expression for the sensitivity to an arbitrary parameter

$$\frac{d\mathcal{J}}{d\boldsymbol{\theta}} = -\int_{\Omega} \boldsymbol{\varphi}^T \frac{\partial \boldsymbol{R}}{\partial \boldsymbol{\theta}} d\mathbf{x}, \tag{3.16}$$

where the adjoint variable vector $\boldsymbol{\varphi}$ is substituted from the adjoint PDE solution. Note that the derivative w.r.t. $\boldsymbol{\theta}$ that appears in the integrand requires differentiation of the partial differential equations that govern the primal solution. If the parameters are part of the chemical source term, this derivative will simply be the derivative of the chemical source term w.r.t the model parameter. In the test cases below, specific parameters will be chosen to illustrate the computation of the sensitivity as defined above.

3.2.4 Numerical implementation

In terms of numerical implementation, the steady-state primal equations (3.2-3.5) are first solved. With an eye towards future unsteady flow studies, a low-Mach number pressure projection algorithm with time-stepping is used [81]. This algorithm is similar to that used for large eddy simulation (LES) computations of reacting flows [81, 82]. The mechanical pressure is obtained by solving an elliptic equation used to enforce continuity. In the cases presented, grid convergence studies were performed to ensure that the primal solution is sufficiently converged. Using the species and velocity fields obtained from the primal problem as well as the Jacobian of the chemical source terms evaluated at these conditions, the adjoint equations given above (3.8-3.11) are

solved. Similar to the primal algorithm, a pressure projection method is used, where the adjoint continuity equation is enforced through the adjoint pressure variable φ_p. The specification of boundary conditions is non-trivial but systematically derived from the primal boundary conditions. The boundary conditions corresponding to two-dimensional flow are provided in Appendix C.

3.3 One-dimensional Burner Stabilized Flame Case

To illustrate the application of the adjoint approach, a one-dimensional burner stabilized flame case is studied. For this flow, direct sensitivity obtained by solving partial differential equations for the sensitivities is also evaluated. In this configuration, a mixture of premixed fuel and oxidizer enters at the inlet of the domain with a specified mass flow rate. Within the domain, a flame burns the fuel mixture into combustion products. The mixture of hot combustion products then exits the domain at the same flow rate.

The forward sensitivity calculation, used for comparison purposes here, could be conducted many different ways. The most straightforward approach is to derive sensitivity equations, which will lead to transport equations for the variables $\partial \boldsymbol{U}/\partial \boldsymbol{\theta}$. As noted in the introduction, this will require many additional equations to be solved. The second approach is based on Eq. 3.15, where the Jacobian of the residual and the sensitivity of the residual w.r.t the parameters are obtained using finite difference methods. Here, the parameters are independently perturbed by a small number, and the the residuals recom-

puted. The difference in residuals divided by the perturbation magnitude will provide the necessary derivatives. Note that the first method is numerically well-posed, where grid convergence will lead to a convergence in sensitivity. The second method, however, is not accurate in this sense. It is well known that the computation of Jacobians using finite differences leads to errors especially when the perturbations are small. Nevertheless, this second approach is used here in order to show comparisons with the CHEMKIN [55] software.

Two different sensitivities are examined here. In the first study, sensitivity of the integration of H_2O mass fraction w.r.t species diffusivity is obtained using the first method for forward sensitivity and the adjoint approach. Grid convergence of the adjoint solutions is discussed. In the second study, a comparison of the sensitivity of the results to Arrhenius pre-exponential parameters is conducted. For this purpose, CHEMKIN [55] based sensitivity is obtained using the second method described above and the adjoint approach. The following sections discuss the test cases and the results.

3.3.1 Governing equations

Applying the same assumptions as listed in Section 3.2.1, the governing equations for this 1D test case simplify to the following:

$$\dot{M}\frac{dT}{dx} - \frac{d}{dx}\left(\alpha\frac{dT}{dx}\right) - \omega_T = 0, \tag{3.17}$$

$$\dot{M}\frac{dY_k}{dx} - \frac{d}{dx}\left(D\frac{dY_k}{dx}\right) - \omega_{Y_k} = 0, \tag{3.18}$$

in which $\dot{M} = \rho u$ is constant using the continuity equation. The second order ODEs require two boundary conditions each. At the inlet, the temperature is specified, and the species mass fractions take a mixed condition. At the outlet, the temperature and the species mass fractions are set with zero-gradient conditions.

Following a similar derivation as the 2D adjoint equations, the corresponding 1D adjoint equations are the following:

$$-\dot{M}\frac{d\varphi_T}{dx} - \frac{d}{dx}\left(\alpha\frac{d\varphi_T}{dx}\right) - \frac{\partial\omega_T}{\partial T}\varphi_T - \sum_j \frac{\partial\omega_{Y_j}}{\partial T}\varphi_{Y_j} = \frac{\partial g}{\partial T}, \tag{3.19}$$

$$-\dot{M}\frac{d\varphi_{Y_k}}{dx} - \frac{d}{dx}\left(D\frac{d\varphi_{Y_k}}{dx}\right) - \frac{\partial\omega_T}{\partial Y_k}\varphi_T - \sum_j \frac{\partial\omega_{Y_j}}{\partial Y_k}\varphi_{Y_j} = \frac{\partial g}{\partial Y_k}. \tag{3.20}$$

The boundary conditions are derived based on the primal boundary conditions as described in Appendix C. At the inlet, the boundary condition for the adjoint temperature is $\varphi_T = 0$ and for species mass fraction is $d\varphi_{Y_k}/dx = 0$. At the outlet, the boundary conditions take the folowing mixed condition:

$$\dot{M}\varphi_T + \alpha\frac{d\varphi_T}{dx} = 0 \text{ and } \dot{M}\varphi_{Y_k} + D\frac{d\varphi_{Y_k}}{dx} = 0. \tag{3.21}$$

Irrespective of the parameter for which the sensitivity is desired, the adjoint equations remain the same.

Additionally, unlike the adjoint equations, the forward sensitivity equations must be derived for each selected parameter. These derived equations will be listed separately for the two different test cases.

3.3.2 Sensitivity to diffusivity

For the test case chosen here, the fuel is hydrogen and the oxidizer is standard air. The inlet temperature is set at 300K and the fuel equivalence ratio is 1. The kinetics model of Marinov [1], which includes 9 species and 20 reactions, has been used. The domain of the solution Ω spans from $x = 0$ to $x = 4$cm, and the computational grid uses evenly spaced grid points. The number of grid points is varied from 5×10^3 to 1.6×10^5 in order to determine convergence of the computed sensitivities. The temperature and water mass fraction fields are shown in Fig. 3.1. The QoI for the sensitivity and adjoint calculations is defined over the region spanning the whole domain Ω_Q from $x = 0$ to $x = 4$ cm as

$$\mathcal{J} = \int_{\Omega_Q} Y_{\mathrm{H_2O}} dx. \tag{3.22}$$

Taking the thermal diffusivity α as the parameter, and consequently the mass diffusivity D since $Le_k = 1$, the forward sensitivity equations are the following:

$$\dot{M}\frac{d\sigma_T}{dx} - \frac{d}{dx}\left(\frac{dT}{dx}\right) - \frac{d}{dx}\left(\alpha\frac{d\sigma_T}{dx}\right) - \frac{\partial\omega_T}{\partial T}\sigma_T - \sum_j \frac{\partial\omega_T}{\partial Y_j}\sigma_{Y_j} = 0, \tag{3.23}$$

$$\dot{M}\frac{d\sigma_{Y_k}}{dx} - \frac{d}{dx}\left(\frac{dY_k}{dx}\right) - \frac{d}{dx}\left(D\frac{d\sigma_{Y_k}}{dx}\right) - \frac{\partial\omega_{Y_k}}{\partial T}\sigma_T - \sum_j \frac{\partial\omega_{Y_k}}{\partial Y_j}\sigma_{Y_j} = 0 \tag{3.24}$$

In the above equations, σ_T is the sensitivity of T to the diffusivity parameter and σ_{Y_k} is the sensitivity of Y_k to the diffusivity parameter. At the inlet, the boundary conditions for the sensitivity equations are $\sigma_T = 0$ and

$$\sigma_{Y_k} - \frac{1}{\dot{M}}\frac{dY_k}{dx} - \frac{D}{\dot{M}}\frac{d\sigma_{Y_k}}{dx} = 0. \tag{3.25}$$

At the outlet, the boundary conditions are $d\sigma_T/dx = 0$ and $d\sigma_{Y_k}/dx = 0$. The forward sensitivity solution is displayed in Fig. 3.2.

The normalized sensitivity $S = d\ln(\mathcal{J})/d\ln(\alpha)$ from the forward sensitivity solution is calculated as

$$S_{\text{fwd}} = \frac{\alpha}{\mathcal{J}} \int_{\Omega_Q} \sigma_{\text{H}_2\text{O}} dx, \tag{3.26}$$

and the sensitivity from the adjoint solution, derived from (3.16), is calculated as

$$S_{\text{adj}} = \frac{\alpha}{\mathcal{J}} \int_{\Omega} \left(\sum_{k}^{N_s} \varphi_k \frac{d^2 Y_k}{dx^2} + \varphi_T \frac{d^2 T}{dx^2} \right) dx. \tag{3.27}$$

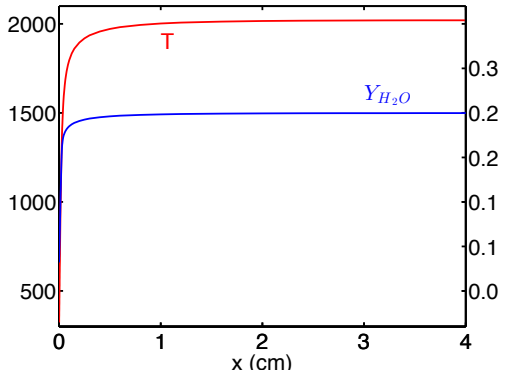

Figure 3.1: 1D primal simulation results for temperature (K) and $Y_{\text{H}_2\text{O}}$

Figure 3.3 displays the relative error, defined as $\epsilon = |S_{\text{fwd}} - S_{\text{adj}}|/S_{\text{adj}}$, between the sensitivities as a function of grid points. With 5000 grid points the relative error is on the order of 1%. However, the flame front itself is not well resolved for that grid spacing. As the grid is refined, the relative error decreases resulting in errors of the same order as the residual errors in the solution of

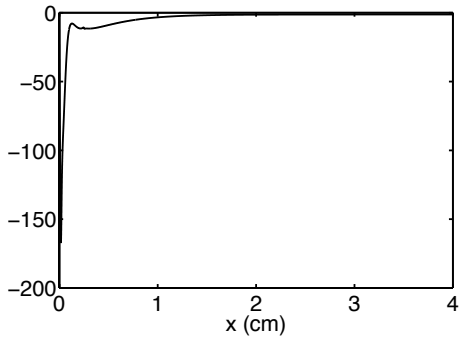

Figure 3.2: 1D forward sensitivity simulation results for $\sigma_{\mathrm{H_2O}}$

the primal equations. This test demonstrates that the forward sensitivity and adjoint sensitivity models produce near identical results accounting for the differences in the solution methodology.

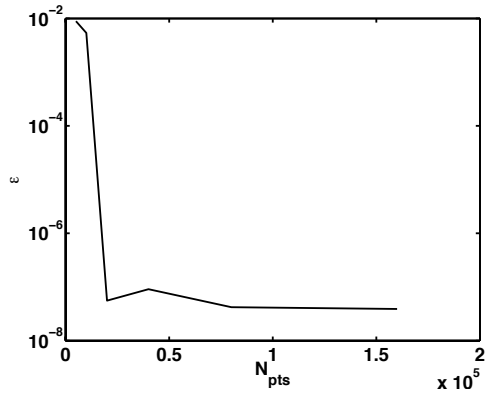

Figure 3.3: Relative error $|S_{fwd} - S_{adj}|/S_{adj}$ between the sensitivity as determined by the forward sensitivity solution and the adjoint solution

3.3.3 Sensitivity to Arrhenius pre-exponential parameters

To compare sensitivities to Arrhenius rate parameter, the finite-difference based forward sensitivity scheme is used. For this comparison, the QoI and the RoI are the same as that used in Sec. 3.3.2. To calculate the forward sensitivities, the CHEMKIN PREMIX code [55] is used along with a finite difference technique. The computational grid is adaptively refined by the CHEMKIN code, and the same grid is used for the dual problem as well. During the CHEMKIN solution, the Jacobian and the change of the residual w.r.t. perturbation of the parameters are calculated using finite differences and substituted into (3.15). Thus, the forward sensitivity from the CHEMKIN solution is calculated as the following

$$S_{\text{fwd},r} = \frac{A_r}{\mathcal{J}} \int_{\Omega_Q} \frac{\partial Y_{\text{H}_2\text{O}}}{\partial A_r} dx. \tag{3.28}$$

The adjoint solution is obtained by solving Eq. 3.19 with the g function specified as in Eq. 3.22. From the adjoint solution, derived from (3.16), the sensitivity is calculated as

$$S_{\text{adj},r} = \frac{A_r}{\mathcal{J}} \int_{\Omega} \left(\sum_{k}^{N_s} \varphi_k \frac{\partial \omega_{Y_k}}{\partial A_r} + \varphi_T \frac{\partial \omega_T}{\partial A_r} \right) dx. \tag{3.29}$$

Figure 3.4 shows the adjoint solution and the forward sensitivity solution for two sample reaction pre-exponential parameters.

Figure 3.5 shows the ten most sensitive parameters as calculated by both the CHEMKIN forward sensitivity method and the adjoint sensitivity method. For both sensitivity methods, the majority of the top ten sensitive parameters are the same and close in magnitude. The fifth and sixth

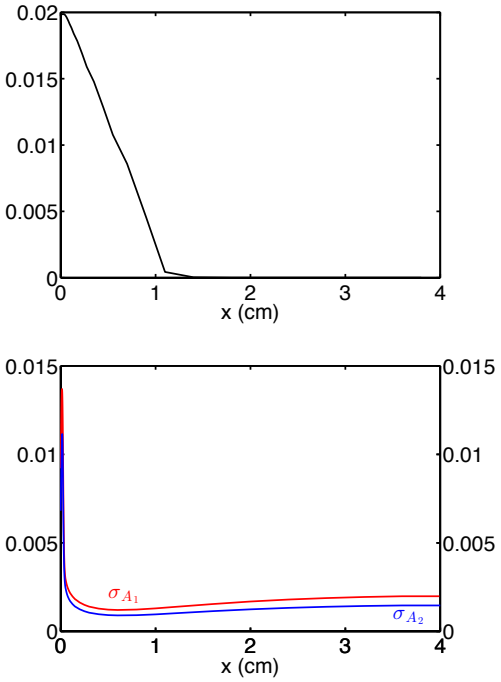

Figure 3.4: 1D adjoint solution (top) and sensitivity solution to reaction pre-exponential parameter A_1 of reaction OH+H_2 $\rightleftharpoons$ H+H_2O and A_2 of reaction O+H_2 $\rightleftharpoons$ OH+H (bottom)

parameters are switched between the two methods, and as the parameter sensitivies become smaller and comparable at the bottom of the sensitivity list, the ninth parameters are different. Note that the finite difference method used to compute forward sensitivities has its limitations, and a convergence of values cannot be obtained as the perturbations becomes small.

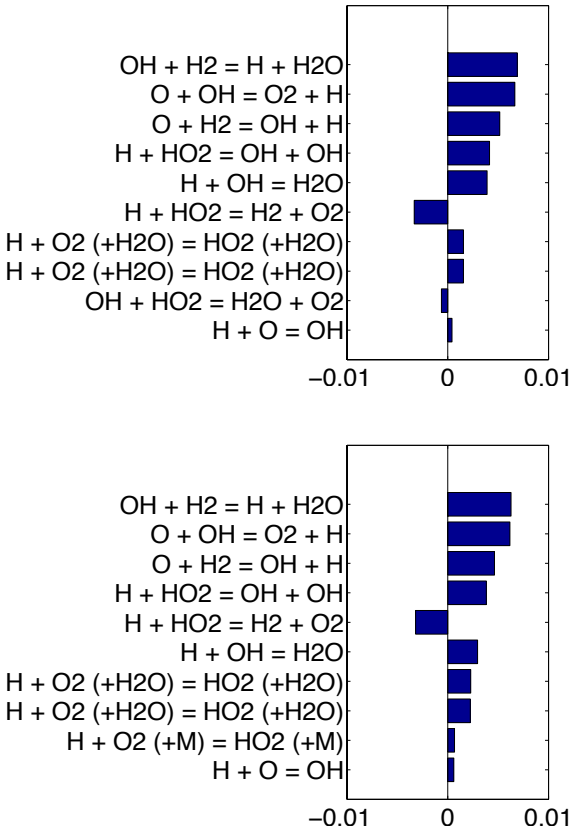

Figure 3.5: The top ten most sensitive parameters as determined by the CHEMKIN forward sensitivity solution (left) and the adjoint solution (right)

3.4 Two-dimensional laminar diffusion flame

To illustrate the application of the adjoint approach to multi-dimensional flow configurations, a laminar hydrogen diffusion flame is studied. The simulation approximates an experimental study of nitrogen-diluted flames [83]. The flame includes a jet of nitrogen-diluted hydrogen with a coflow of air at standard atmospheric pressure. Figure 3.6 shows a schematic of the domain

of the axisymmetric simulation with the inlet sections labeled. The fuel jet inner diameter is 9 mm, and the fuel pipe extends 8 mm into the domain. The coflow extends to the lateral boundary of the domain. Table 4.1 lists the inlet flow properties, as well as the rest of the boundary conditions for the primal. In the table 'zg' refers to a zero gradient boundary condition, $\partial/\partial x_n = 0$. The adjoint boundary conditions are listed in Table 4.2. Again, 'zg' refers to a zero gradient condition, while 'mg' refers to the following mixed gradient condition

$$u_n \varphi + \Gamma \frac{\partial \varphi}{\partial x_n} = 0, \tag{3.30}$$

and 'mg-φ_h' refers to

$$u_n \varphi_h + \Gamma \frac{\partial \varphi_h}{\partial x_n} = \frac{u_n}{h} \left(\varphi_C + u_t \varphi_{M_t} \right), \tag{3.31}$$

where the subscripts n and t refer to the normal and tangential components, respectively.

For this particular study, two different QoIs are considered: spatially averaged temperature and NO_x. The latter quantity is the key result of many combustion simulations, and an analysis of its sensitivities is critical in the development of robust chemistry models. For this purpose, a detailed kinetics model for hydrogen with NO_x formation [84] is used. This model includes 32 species and 172 reactions. The next two sections will include first a brief description of the flame simulation results and second a description of the parametric sensitivity results calculated using the adjoint solution.

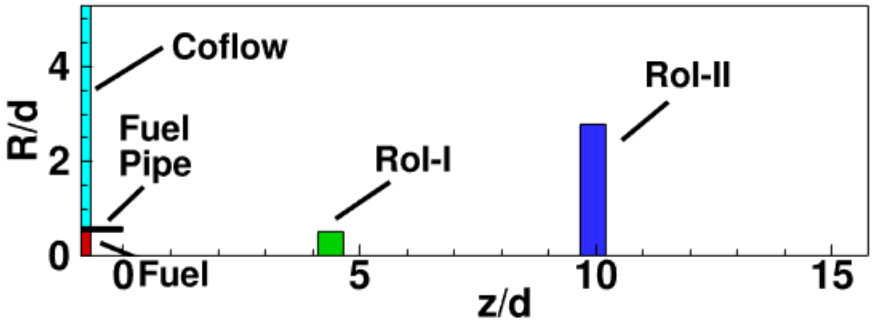

Figure 3.6: Schematic of the simulation domain showing the fuel inflow, fuel pipe, coflow, and RoIs

Table 3.1: Primal boundary conditions

Prop.	Fuel	Coflow	Pipe wall	Outlet
T, K	293.0	293.0	293.0	zg
Y_{H_2}	0.0671	0.0	zg	zg
Y_{O_2}	0.0	0.232	zg	zg
Y_{N_2}	0.9329	0.768	zg	zg
Y_{other}	0.0	0.0	zg	zg
u_z, m/s	0.18	0.18	0.0	zg
u_R, m/s	0.0	0.0	0.0	zg
p'	zg	zg	zg	zg

3.4.1 Primal solution of the laminar flame configuration

In the primal simulation, a flame forms beginning just downstream of the inlet pipe. This flame can be visualized by the temperature field shown in Figure 3.7. The flame forms around the fuel jet and reaches a peak temperature of approximately 1940K 4.4 jet diameters downstream. The central region of the flow remains greater than 825K for the entire length of the domain, which is approximately 16 jet widths.

The NO_x mass fraction fields are plotted in Fig. 3.8. Nitric oxide peaks

Table 3.2: Adjoint boundary conditions

Prop.	Fuel	Coflow	Pipe wall	Outlet
Φ_h	0.0	0.0	0.0	mg-φ_h
Φ_Y	0.0	0.0	mg	mg
Φ_{M_n}	0.0	0.0	0.0	0.0
Φ_{M_t}	0.0	0.0	0.0	mg
Φ_C	zg	zg	zg	zg

in the region just downstream of peak temperature, as expected since the Zeldovich/thermal mechanism for NO_x production is dominant for this flame. Although its peak value decreases as the flow cools downstream, NO remains in the flow. Nitrogen dioxide peaks in the downstream area of the flow beyond the flame. Here, the NO formed in the higher temperature regions combines with the cool coflow and reacts to form NO_2. In this flow configuration, NO_x concentration is predominantly due to the NO component. The NO_2 mass fraction serves to extend and spread the total mass fraction of NO_x due to its location downstream of and on the periphery of the high temperature region.

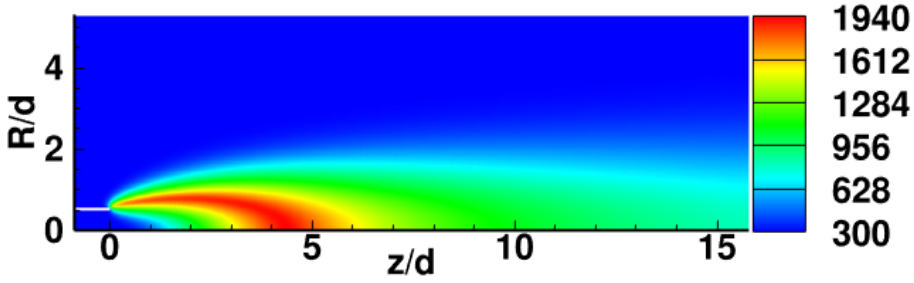

Figure 3.7: Contour plot of temperature (K) from the primal solution

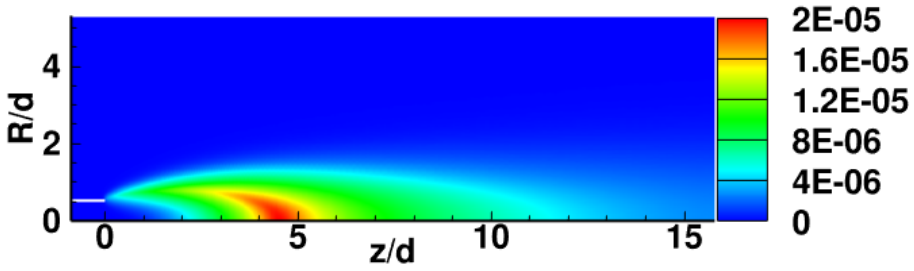

(a) Y_{NO}

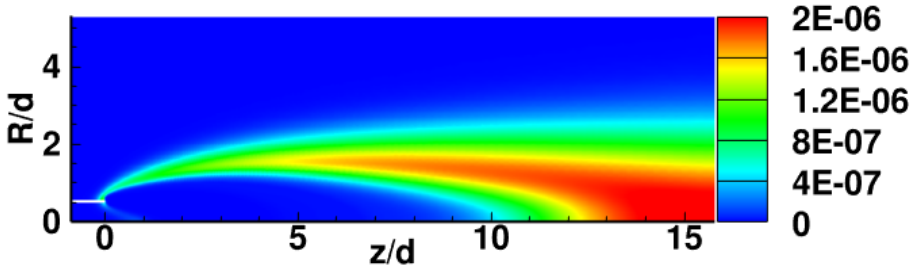

(b) Y_{NO_2}

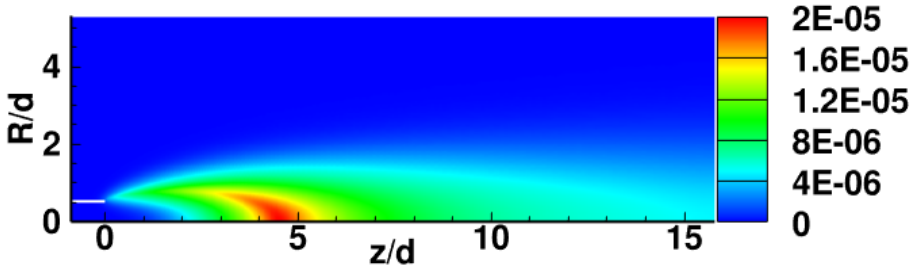

(c) Y_{NO_x}

Figure 3.8: Contour plots of NO_x mass fractions from the primal solution

3.4.2 Laminar flame adjoint simulation results

Two different QoIs are considered here. The first QoI, QoI-I, is the average temperature in a region near the tip of the flame:

$$\mathcal{J} = \frac{1}{V_{\mathrm{Q}}} \int_{\Omega_{\mathrm{Q}}} T d\mathbf{x}, \tag{3.32}$$

where Ω_{Q} refers to the RoI, the region over which the temperature has been averaged, and V_{Q} is the volume of that region. Figure 3.6 shows Ω_{Q}, which is a rectangular region (a disk when the axisymmetric region is revolved) near the tip of the flame. The region spans radially from the axis to 1.0 cm and extends axially from 4.5 cm to 5 cm. QoI-I and the region Ω_Q have been defined to serve as a measure of the flame temperature in some hypothetical combustion device. A selection of the adjoint solution fields for the temperature QoI simulation are displayed in Fig. 3.9. It is seen that the different species equations, the enthalpy equation, and the momentum equation exert differing influence over the QoI, and the region of influence depends not only on the chemical source terms of the associated equations but also the transport and diffusion characteristics. In this sense, the adjoint exhibits the propagation of information. More specifically, it could be argued that the adjoint itself describes the propagation of a small disturbance at each point in the computational domain. In other words, the magnitude of the adjoint indicates the change in the QoI for a small perturbation in the field variable at a given location. The spatial variations in the adjoint field emphasize the fact that not all regions equally impact the QoI or the RoI. For instance, the OH and O_2 adjoints indicate that

the near-exit region that forms the interface between the fuel and coflow has significant impact on the flame temperature, but the enthalpy adjoint has a more uniformly spread field.

Due to the importance of determining pollutant levels in many simulations, the mass of the pollutant NO_x downstream of the laminar flame has been chosen as the second QoI, QoI-II, for this study. QoI-II is defined in the following manner:

$$\mathcal{J} = \int_{\Omega_Q} \rho(Y_{NO} + Y_{NO_2}) d\mathbf{x}, \tag{3.33}$$

where Ω_Q refers to the RoI, the region over which the NO_x has been calculated. Figure 3.6 shows Ω_Q, which is a rectangular region (a disk when the axisymmetric region is revolved) downstream of the flame. The region spans radially from the axis to 2.5 cm and extends axially from 9.5 cm to 10 cm. QoI-II and the region Ω_Q have been defined to serve as a measure of the amount of NO_x leaving some hypothetical combustion device. A few of the adjoint solution fields are shown in Fig. 3.10. Again, the different species equations exert differing influence over the QoI, showing that the adjoint itself describes the propagation of a small disturbance at each point in the computational domain.

Figure 3.10 also shows that the adjoints for QoI-II differ from the adjoints for the temperature QoI. The QoI function $\mathcal{J}$ essentially acts as a forcing term in the adjoint equations. Its effect is seen as a clear demarcation in the adjoint solutions. Since this flow contains no recirculation, there is very little influence of the downstream fluid on the QoI. Hence, most of the adjoint

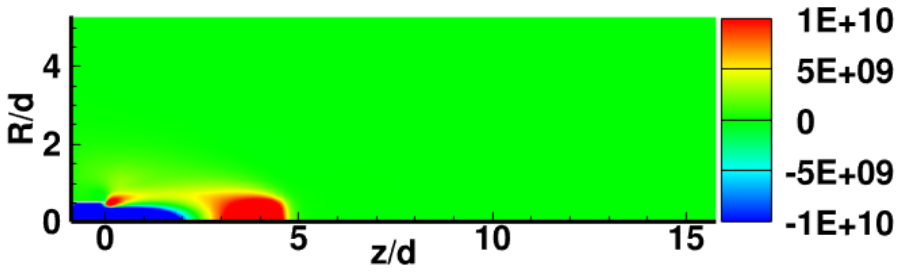

(a) φ_{OH}

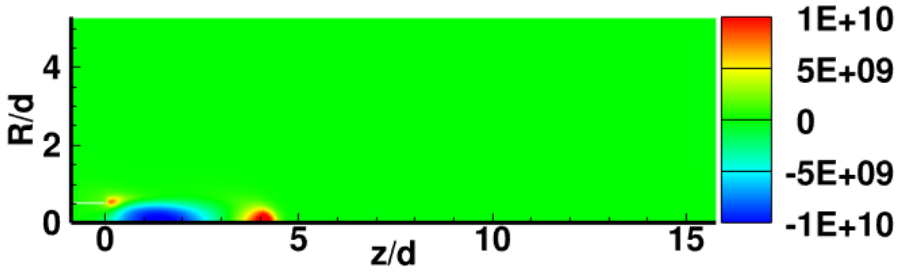

(b) $\varphi_{\mathrm{O_2}}$

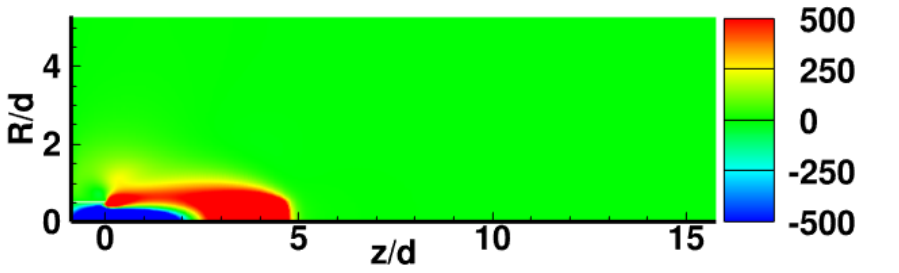

(c) φ_{h}

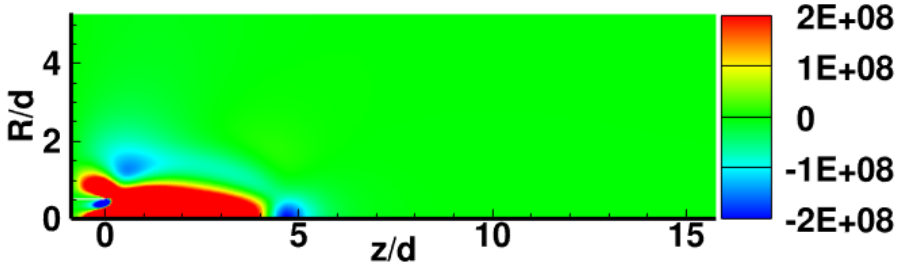

(d) φ_{u_i}

Figure 3.9: Adjoint variable fields for Y_{OH}, $Y_{\mathrm{O_2}}$, enthalpy, and axial velocity for QoI-I

features are seen upstream of the flow. The OH adjoint shows significant values in regions where the flame front is not present. This indicates that any disturbance on the lean-side of the flame will lead to large changes in the QoI. Although some adjoints are predominantly negative, there is no direct inference from this to the sensitivity, since that depends on the partial of the chemical source term with respect to the parameters as well (Eq. 3.29).

3.4.3 Sensitivity to kinetics parameters

The sensitivity of each QoI to the reaction pre-exponential parameters can be readily calculated from the adjoint solution using (3.29), for which Ω refers to the entire 2D domain. The sensitivity is shown in normalized form, $\partial ln\mathcal{J}/\partial lnA_r$. Figure 3.11 shows the ten most sensitive parameters for QoI-I. The average temperature in RoI-I is most sensitive to the parameter for H + OH $\rightleftharpoons$ H_2O. This chain terminating reaction provides significant heat release in the high temperature region of the flame. Not unexpectedly, none of the NO_x formation reaction parameters significantly affect the average temperature in the flame tip region.

The sensitivity of QoI-II to the reaction pre-exponential parameters was also calculated for the same primal flame simulation. Figure 3.12 shows the ten most sensitive parameters for QoI-II, again with the sensitivity in normalized form. The most sensitive parameter for the amount of NO_x downstream is one of the elementary reactions in the hydrogen chemistry model without NO_x production. The next five, however, come from the NO_x extension of

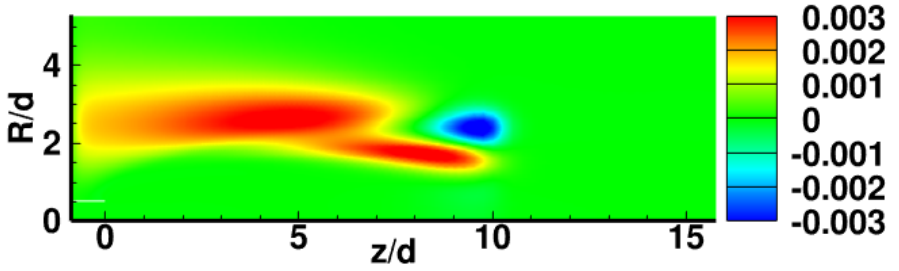

(a) φ_{OH}

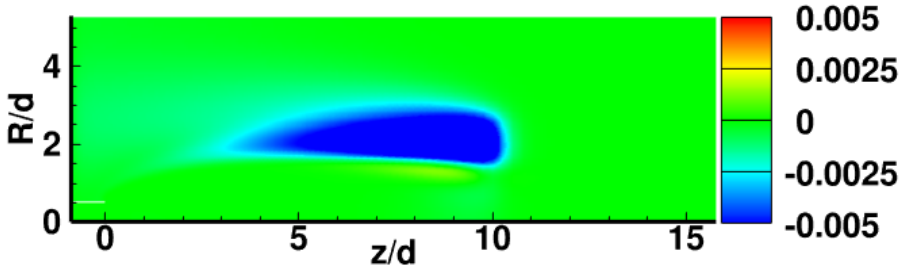

(b) φ_{O}

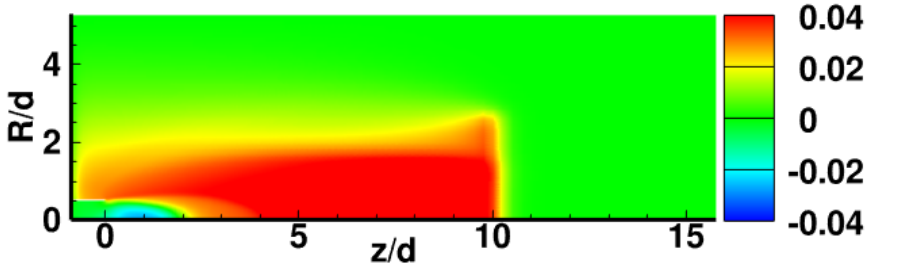

(c) φ_{N}

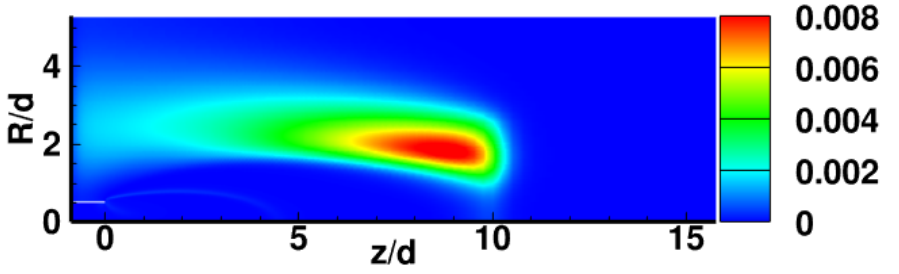

(d) φ_{NNH}

Figure 3.10: Adjoint variable fields for Y_{OH}, Y_{O}, Y_{N}, and Y_{NNH} for QoI-II

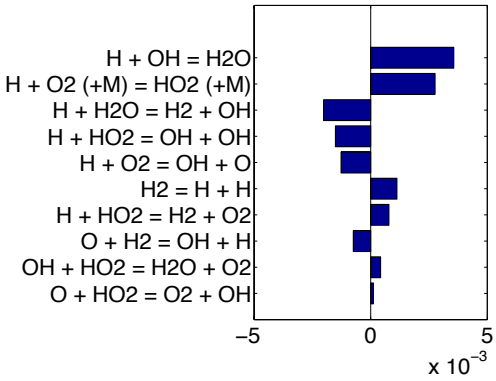

Figure 3.11: Top ten Arrhenius pre-exponential sensitivities for QoI-I, the average temperature in RoI-I

the mechanism. The most sensitive parameter of these five corresponds to the reaction N + NO $\rightleftharpoons$ O + N_2, which is the rate-limiting reaction for the thermal production of NO_x. For this high-temperature diffusion flame, the thermal mechanism for production of NO_x is expected to be the most important pathway. The next three parameters correspond to reactions important for the N_2O pathway for production of NO_x. The last of those five, as well as the ninth most sensitive parameter, correspond to reactions important in the NNH pathway of the production of NO_x.

3.5 Conclusions

The adjoint equations for low-Mach number reacting flow with multiple species have been derived and implemented in a finite-volume solver. The adjoint approach allows fast and efficient computation of sensitivity information for multi-dimensional flames. The number of additional equations that need to

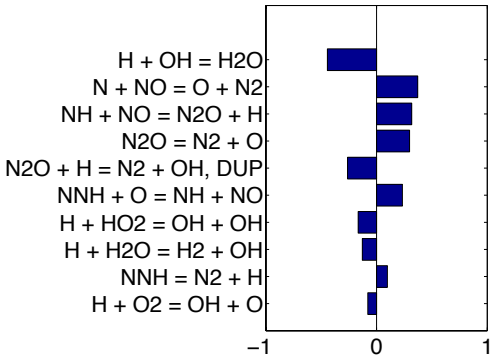

Figure 3.12: Top ten Arrhenius pre-exponential sensitivities for QoI-II, the integrated mass of NO_x in RoI-II

be solved scales as the number of primal equations times the number of QoIs, as opposed to the forward sensitivity approach that scales as the number of primal equations times the number of parameters. The adjoint equations are linear as opposed to the nonlinear primal equations, and have a mathematical structure that is comparable to the primal equations. For instance, pressure projection approaches used to solve the primal equations could be directly used for the dual system. The adjoint equations also exhibit significant differences in the details of the different terms. For instance, all the adjoint equations include a negative convective term that transports adjoint information from the primal outflow to the primal inflow. In addition, the scalar adjoint equations do not contain momentum adjoint information but are linked through the enthalpy adjoint equation. In this sense, if the scalars are passive (nonreactive), their adjoint equations will be completely decoupled from the momentum adjoints. This is different from the primal equations where passive scalars are still transported by the velocity field.

Two different flow configurations were studied. The 1-D system was used to compare adjoint solutions with forward sensitivity based results. It was shown that the adjoint method converges to the forward sensitivity solution with increasing number of grid points, which is consistent with numerical implementation of partial differential equations. Comparison of the 1-D flame solution with finite-difference based sensitivity showed that both methods reproduced the most sensitive reactions, but there were discrepancies as the sensitivities of the parameters decreased. This is mainly due to the lack of numerical convergence of the finite-difference based formulations. The 2-D laminar flame problem showed that the adjoint solution exhibits different spatial distribution for the different adjoint variables. The two different QoIs provided vastly different adjoint solutions due to the differences in the location and strength of QoI based forcing functions. It is seen that the solutions are non-trivial and exhibit complex features. Hence, it is expected that the sensitivity to parameters that affect the different species will also be inherently complex.

The adjoint method is a powerful tool that could provide enormous insight into the way validation experiments are designed and used. For instance, an analysis of the sensitivities of a particular measurement performed at a given location is directly obtained. Hence, calibration of model parameters could be carried out in a more sophisticated manner. Further, the adjoint solutions could be obtained not just for laminar flames but also for full turbulent flow configurations, which are usually the end application for any chemistry

model. Although there are difficulties applying this technique to unsteady chaotic problems [85], it is readily applied to steady-state Reynolds-averaged Navier Stokes (RANS) results, which are commonly used in the engine design cycle. Apart from providing predictions of key quantities, the adjoint approach used on these RANS results could provide the most critical parameters that affect simulations. This information could be further used to refine experiments or other sources of data for better calibration of the important parameters.

Chapter 4

Adjoint field sensitivity

4.1 Introduction

The description of gas phase chemical pathways is the first step towards the successful computational modeling of combustion. Naturally, this aspect has received considerable attention throughout the history of combustion research. Progress in chemistry model development is measured by the ability of the constructed mechanisms to reproduce certain quantities of interest (QoIs) for a variety of flow conditions. For instance, ignition time delay or specific species compositions are often chosen as the QoIs. The flow conditions are supposed to mimic, in a macroscopic sense, the end applications, which are full scale CFD calculations of large scale industrial combustion devices. In order to reproduce a wide range of operating conditions, the chemistry model is invariably made more complex by introducing a large number of pathways and associated reactions.

The downside, of course, is that this increase in the number of reactions is accompanied by the need to determine rate models, which is in effect the specification of Arrhenius rate coefficients. Since the number of experiments available to determine such rate coefficients are not sufficient to un-

ambiguously specify the values, there is considerable uncertainty introduced by the chemistry model. Recent works in the area of uncertainty quantification [20, 22, 86] have shown that not all experiments are useful in improving the model, and that there is substantial correlation between the model coefficients. In addition, it has become clear that the level of certainty required in estimating certain key quantities such as temperature really depends on the ultimate prediction QoI. For instance, Mueller and Raman [87] show that a 5% error in temperature predictions upstream could result in 50-75% error in the prediction of soot volume fraction in a turbulent jet flame. In this sense, even if chemistry models could reproduce experiments designed for parameter calibration, their accuracy in full scale calculations cannot be known *a priori*.

Here, we seek a quantitative measure that goes beyond reproducing experimental values to compare chemistry models. We introduce a new quantity termed field sensitivity that measures the sensitivity of a QoI to perturbations in the flow field. To understand field sensitivity, consider the laminar flame shown in Fig. 4.1. A region of interest (RoI) defines the QoI $\mathcal{J}$, expressed as the surface or volume integral over a sub-domain of the flow field. If the flow field U (including the gas phase species compositions) is perturbed at any point in the flow, such perturbations can impact $\mathcal{J}$. The field sensitivity is defined as $\frac{\partial \mathcal{J}}{\partial U}$, which is a fundamental quantity that, in theory, is measurable. (In Sec. 4.2, this quantity will be defined more rigorously from a computational standpoint).

The motivation for this measure comes from the fact that predictive

models should not only reproduce target quantities but also their variations with changes to the flow field. At a more fundamental level, one can view the governing equations as models that recover the nature of information propagation in a flow. A disturbance at a point in the flow will be convected and diffused in a particular manner. The goal of the models should be to capture the same propagation as that would occur in reality, if a similar perturbation occurs in the laboratory flow conditions.

It is important to distinguish field sensitivity from the conventional measure of parametric sensitivity. In the latter approach, the change in QoIs with respect to changes in model parameters are obtained. This quantity has no fundamental significance, since model parameters are not identical for the different models. The parameters could have been calibrated to take on different numerical values, or may not even be present if the pathways they are associated with are absent in a mechanism (essentially, the parameter is set to zero value in this case). Hence, this variability between different chemistry models prevents a meaningful comparison of parametric sensitivity. Because field sensitivity is related to the species/flow variables themselves, it is a more fundamental quantity.

With this introduction, the purpose of this chapter is to discuss the mathematical equations and numerical implementation for determining field sensitivity. In the next section, the field sensitivity will be defined based on the adjoint of the flow problem. Following this, a numerical simulation of a laminar flame configuration using three different chemistry mechanisms will

be used to illustrate the usefulness of this new quantity.

4.2 Adjoint-based formulation of field sensitivity

As with the previous chapter, the focus of this study is a two-dimensional steady laminar flow configuration. The formulation is based on a low-Mach number approach [88]. Again, the pressure field is decomposed into a thermodynamic pressure, P_0, and a so-called first-order pressure p'. The fluctuating pressure is set such that the continuity equation is satisfied by the flow field. This a common technique used in a variety of computational solvers, including state-of-the-art large eddy simulation (LES) methods [81, 89, 90] to avoid resolving acoustic wave propagation. Here, this approach is used primarily to be consistent with these LES solvers, so that the results could be directly interpreted in terms of the end application. In addition, constant physical properties and calorically perfect gas have been assumed. Since the focus here is only to demonstrate the concept of field sensitivity, these assumptions are made to simplify the discussion. It should be noted that there is no loss of generality, and the field sensitivity could be derived using any of the methods and property variations used to solve laminar flow equations [91, 92]. The governing equations for this flow (termed the primal equations) are those listed in Sec. 3.2.1. As in the previous chapter, to derive field sensitivity, an adjoint-based sensitivity approach is used.

The adjoint equations are derived in Appendix C. A brief discussion of that derivation is included here to motivate the use of field sensitivity. First,

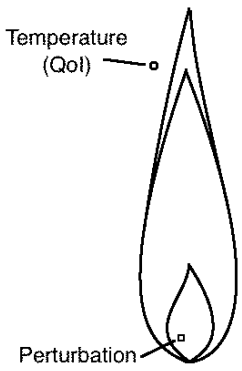

Figure 4.1: Schematic of a laminar flame showing a perturbation and temperature as the QoI

define a set of variables $\Phi = [\phi_p, \phi_{u_i}, \phi_h, \phi_{Y_k}]^T$. A Lagrangian based on Φ as the multiplier is formulated as follows:

$$\mathcal{L}(U, \Phi) = \mathcal{J}(U) + \int_\Omega \Phi^T \mathcal{R}(U) d\mathbf{x}, \tag{4.1}$$

where Ω refers to the flow domain and

$$\mathcal{J}(U) = \int_{\Omega_d} g(U) d\mathbf{x} \tag{4.2}$$

is the quantity of interest defined as an integral of a function over the region of interest (Fig. 4.2). In the context of optimization, the above equation could be interpreted as computing $\mathcal{J}$ subject to the constraint (in a weak sense) that $\mathcal{R} = \mathbf{0}$. Two optimality conditions could then be written as

$$\mathcal{L}'(\Phi)(U, \Xi) = \int_\Omega \Xi^T \mathcal{R}(U) d\mathbf{x} = 0, \tag{4.3}$$

and

$$\mathcal{L}'(U)(Z, \Phi) = \mathcal{J}' Z - \int_\Omega \Phi^T \mathcal{R}' Z d\mathbf{x} = 0. \tag{4.4}$$

In the above equations, the prime superscript on the variables denote a variation or a directional change. The first equation implies that the variation of $\mathcal{L}$ in the direction of Φ is zero, with Ξ as the variable that denotes the change in the Φ direction. This leads to the condition that the residual should be zero in a weak sense (integrated over the entire domain), which essentially states that U should satisfy the primal equations. The second equation is more interesting, providing the formulation that will lead to transport equations for Φ. The transport equations for the adjoints are listed in Eqs. 3.8-3.11.

The boundary conditions for solving the adjoint equations (Eq. 3.8-3.11) are obtained as part of the derivation, and have to be consistent with the primal boundary conditions. In fact, this consistency preserves the uniqueness of the adjoint solution. A list of boundary conditions for the particular configuration solved in this work is provided in Sec. 4.3.1.

The adjoint solution could then be used to obtain either the parametric sensitivity, as described in Sec. 3.2.3, or the field sensitivity described as follows. Consider a parameter α that appears in the primal governing equations. The sensitivity $\partial\mathcal{J}/\partial\alpha$ is given by

$$\frac{\partial \mathcal{J}}{\partial \alpha} = -\int_{\Omega} \Phi^T \frac{\partial \mathcal{R}}{\partial \alpha} d\mathbf{x}, \tag{4.5}$$

where the integrand consists of the product of the adjoint and the derivative of primal equations w.r.t the parameter. Since the adjoint solution does not depend on the choice of parameter, the same solution could be used to compute sensitivities for any number of parameters. To define the field sensitivity,

consider an additional source term to the primal scalar transport equation (Eq. 3.5), given by G_k^n. This source term serves as a local perturbation and is active only over a small region of the flow field.

$$G_k^n = \theta_k^n \delta(\mathbf{x} - \mathbf{x}_n), \tag{4.6}$$

where $\mathbf{x}_n$ is a local position in the flow field, and δ is the Dirac-delta function. For a finite sized computational grid, there will be N such parameters located at each grid point. In this case, based on Eq. 4.5, the sensitivity to the parameter θ_k^n is simply given by

$$\frac{\partial J}{\partial \theta_k^n} = -\int_\Omega \Phi^T \frac{\partial \mathcal{R}}{\partial \theta_k^n} d\mathbf{x} = \varphi_{Y_k}(\mathbf{x}). \tag{4.7}$$

In other words, the sensitivity to perturbation in the flow field is the adjoint itself. Expressed in this way, the field sensitivity is nothing but the adjoint field. Note that the perturbation is not added when solving the primal equation but is used here only to motivate the definition of the field sensitivity.

The field sensitivity thus contains information about the propagation of a disturbance through the flow field and the impact of a particular location in the flow field on the final quantity of interest. It is thus a tangible quantity that is independent of the models used to describe chemical kinetics and should reproduce the sensitivity of the true system. However, there exists no direct method for obtaining these perturbed flames in practice other than the computationally expensive method of perturbing the solution at each location with G_k^n. Alternatively, this field sensitivity measure could be used to

determine the differences between different chemistry models, even if the QoI predictions from these models are essentially similar. In addition, the field sensitivity could be evaluated in practical turbulent flames as well to determine if the regions of composition space that are critical here are accessed in a simpler laminar flame configuration. This approach will ensure that reaction rate mechanisms optimized in simpler flames are reliable in turbulent flames.

4.3 Results and discussion

4.3.1 Laminar flame test case

A series of laminar flame simulations and their corresponding adjoint simulations have been developed for a laminar hydrogen flame. The conditions were chosen to approximate those of a nitrogen-diluted flame experiment [83]. The simulations were performed on an axisymmetric grid with 9940 points. Figure 4.2 displays the domain, which includes a jet of inner diameter 9 mm which extends into the domain by 8 mm. For these simulations the Lewis number has been assumed to be 1 for simplicity of the adjoint derivation, and the associated viscosities set to $1.8\times10^{-4}\,\mathrm{kg/m/s^2}$ to counter the lack of increase in viscosity at the flame. The primal simulations were integrated forward in time until a steady state was reached. Then, given the steady state solution of the primal, the steady adjoint equations were solved to give the adjoint solution. For the simulations, both the primal and the adjoint governing equations include a continuity equation. The primal simulation imposes continuity through the use of a pressure projection method. In the

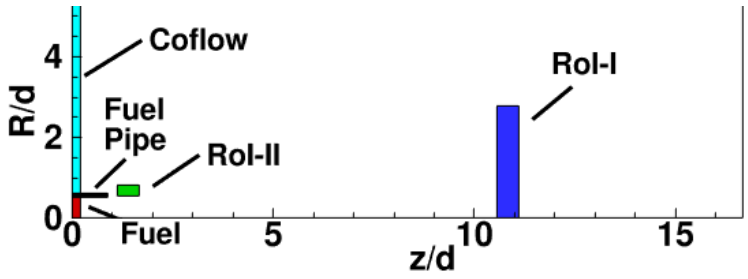

Figure 4.2: Schematic of the simulation domain, including RoI-I (blue) and RoI-II (red)

adjoint simulations, the adjoint continuity is analogously imposed through the use of a projection method.

The boundary conditions for the primal simulations are listed in Table 4.1 and those for the adjoint simulations in Table 4.2. The subscripts 'n' and 't' refer to the boundary normal and tangential components, respectively. The symbol 'zg' in the tables refers to a zero gradient condition, $\partial/\partial x_n = 0$. The symbol 'mg' in the adjoint boundary condition table refers to a mixed gradient condition, $u_n\Phi + \Gamma\partial\Phi/\partial x_n$, for which Γ is the diffusivity. The symbol 'mgΦ_h' is the mixed gradient condition on adjoint enthalpy, which is $u_n\Phi_h + \Gamma\partial\Phi_h/\partial x_n = u_n/h\,(\Phi_C + u_t\Phi_{M_t})$. Regarding the adjoint solution, although no Dirichlet boundary conditions are set, the QoI term serves as a source for the equations driving the results.

Three different chemistry models were used to simulate the laminar flame. The model of Konnov [93], referred to as KM, focused on improvements to reactions between H and HO_2, as well as OH and HO_2. The model of Li, et al [2], referred to as LM, improved on previous mechanisms by introducing

updates to the enthalpy of formation of OH, as well as updates to several key reactions. The model of Burke, et al [3], referred to as BM, is an update of the LM. It incorporates several impovements, such as third-body efficiencies for the H + O_2 (+M) $\rightleftharpoons$ HO_2 (+M) reaction.

Table 4.1: Primal boundary conditions

Prop.	Fuel	Coflow	Pipe	Outlet
T, K	293.0	293.0	293.0	zg
Y_{H_2}	0.0671	0.0	zg	zg
Y_{O_2}	0.0	0.232	zg	zg
Y_{N_2}	0.9329	0.768	zg	zg
Y_{other}	0.0	0.0	zg	zg
u_z, m/s	0.18	0.18	0.0	zg
u_R, m/s	0.0	0.0	0.0	zg
p'	zg	zg	zg	zg

Table 4.2: Adjoint boundary conditions

Prop.	Fuel	Coflow	Pipe	Outlet
Φ_h	0.0	0.0	0.0	mgΦ_h
Φ_Y	0.0	0.0	mg	mg
Φ_{M_n}	0.0	0.0	0.0	0.0
Φ_{M_t}	0.0	0.0	0.0	mg
Φ_C	zg	zg	zg	zg

4.3.2 Primal solutions for the three mechanisms

The forward solution, which involves solving Eq. 3.2-3.5, is presented in Figs. 4.3, 4.4, and 4.5 for three hydrogen chemistry mechanisms. The three mechanisms have been calibrated using some overlapping data, but unique experimental data as well. Consequently, the rate parameters for select reactions

in each mechanism are different. In spite of these differences, it is seen that the three models produce very similar data for the laminar flame under consideration. For instance, the H_2O mass fractions are within about six percent for all the calculations. For the OH mass fraction, the discrepancy in the results manifests as a small shift, change of width, and change in magnitude of the region of peak values (Fig. 4.5). This similarity in results is typical of chemistry models for well-characterized fuels. The primal solution also indicates that by z/d = 2.6, the flame tip is reached. The OH layer is confined to a region of width d/2 centered at approximately z/d of 2.4.

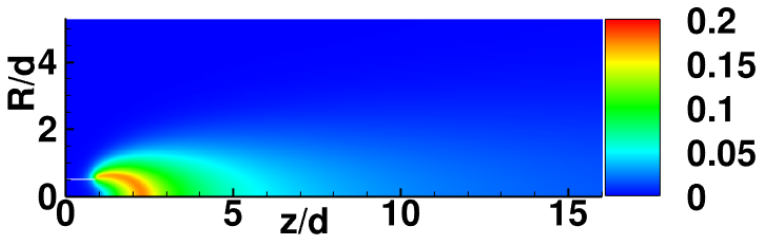

Figure 4.3: Y_{H_2O} for the KM

4.3.3 Field sensitivity for the three mechanisms

For this study, two separate QoIs are defined. The adjoint simulations are performed for each QoI, leading to a field sensitivity for each QoI for every variable. QoI-I and QoI-II are defined in the following manner:

$$\mathcal{J}_{\text{QoI-I}} = \int_{\text{RoI-I}} Y_{H_2O} d\mathbf{x},$$

$$\mathcal{J}_{\text{QoI-II}} = \int_{\text{RoI-II}} Y_{OH} d\mathbf{x}.$$

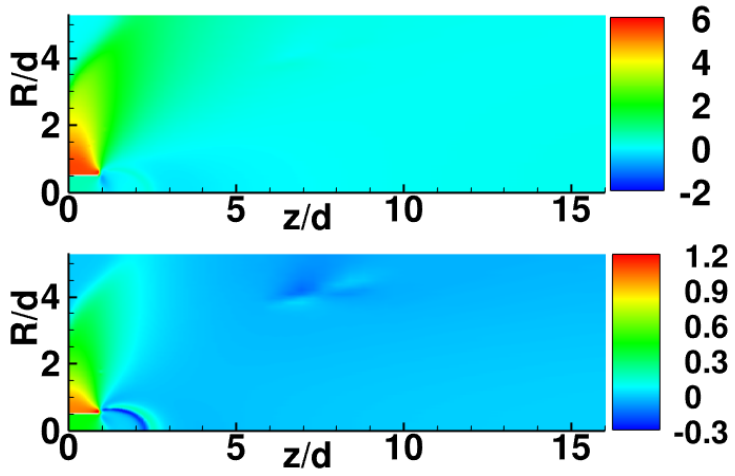

Figure 4.4: Percentage difference for Y_{H_2O} between the KM and BM (top) and KM and LM (bottom)

These QoIs represent the completion of combustion and an important intermediate for combustion. The regions of interest are shown in the domain schematic, Fig. 4.2, as the blue and green regions, respectively. From the primal simulations, QoI-I varies between the three models by less than 0.1%, and QoI-II varies by less than 6.5%.

The field sensitivity for QoI-I to OH is plotted in Fig. 4.6. Between the three models, the region upstream of the flame is very similar. Within the flame, and just downstream of the flame, there are differences. The position of the sensitivity peak shifts by approximately d/2 across the three models, and the magnitude of the peak sensitivity is greatest for the KM. These field sensitivities show that additional OH downstream of the flame will have a tendency to form additional H_2O in the region where the combustion products are at approximately 1000K.

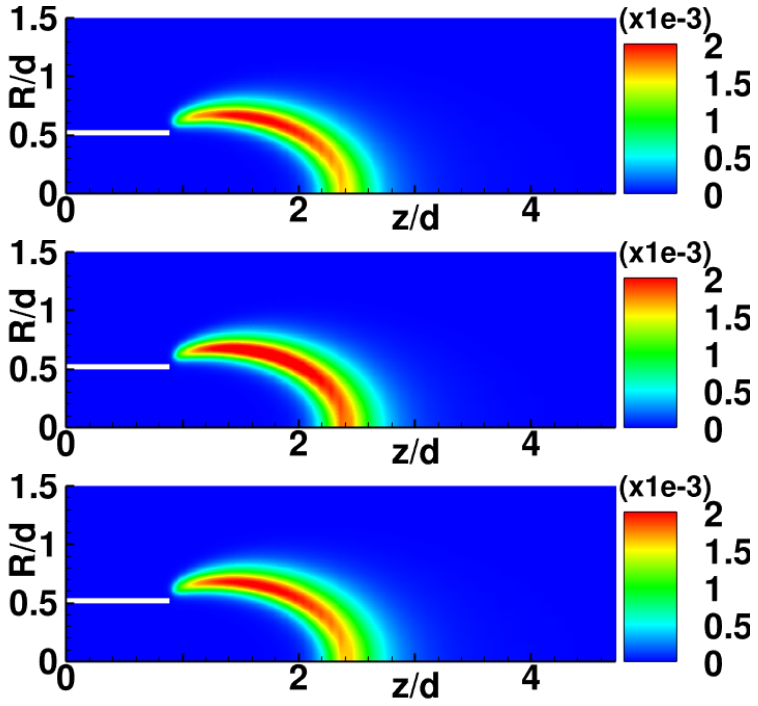

Figure 4.5: Y_{OH} for the KM (top), BM (middle), and LM (bottom)

The field sensitivity for QoI-II to HO_2 is plotted in Fig. 4.7. Between the three models, there are variations in magnitude and size of the sensitive regions. All three models show a pair of regions for which QoI-II correlates to HO_2. In a region near the fuel pipe lip, increases to HO_2 will tend to increase QoI-II. This sensitivity is most pronounced for the LM, for which the sensitivity even reaches into the fuel pipe. In a small region outside of the flame, increses to HO_2 will tend to decrease QoI-II.

The QoIs additionally can change given perturbations to the velocity itself. Figure 4.8 displays the field sensitivity of QoI-I to the velocity components for the KM. An increase in the streamwise velocity of the fuel as it exits

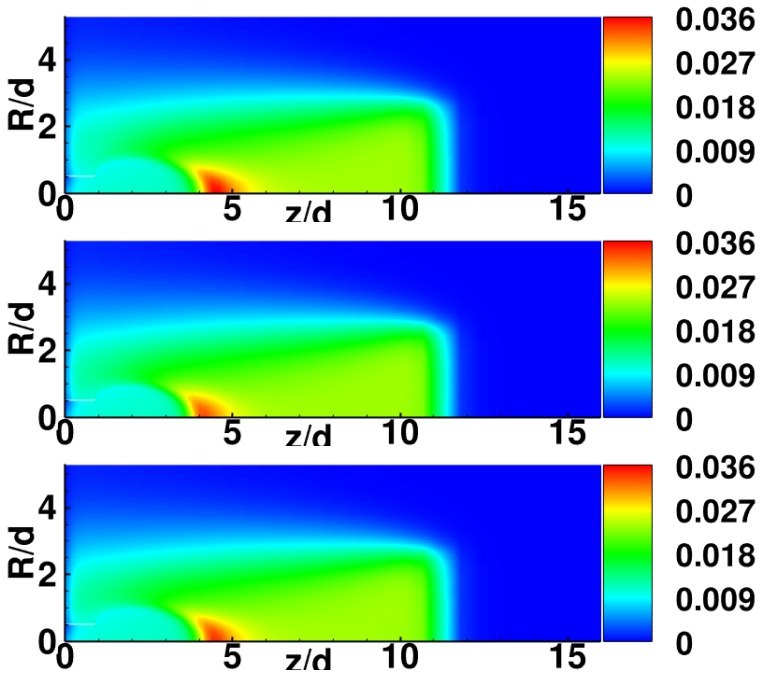

Figure 4.6: Field sensitivity of QoI-I to OH for the KM (top), BM (middle), and LM (bottom)

the fuel pipe and of the coflow near the fuel pipe corresponds to an increase in QoI-I. Also, reduced radial velocity at the lip of the fuel pipe, as well as increased radial velocity as the fuel leaves the pipe, correspond to an increase in QoI-I. Therefore, additional entrainment of oxidizer at the lip of the fuel pipe and additional H_2 entering the flame will tend to increase the mass fraction of H_2O in RoI-I, as is expected.

4.3.4 Parameter sensitivity for the three mechanisms

The sensitivity of each QoI to the reaction pre-exponential parameters can be readily calculated with this method. Here, the sensitivity $\partial ln\mathcal{J}/\partial lnA_r$ is

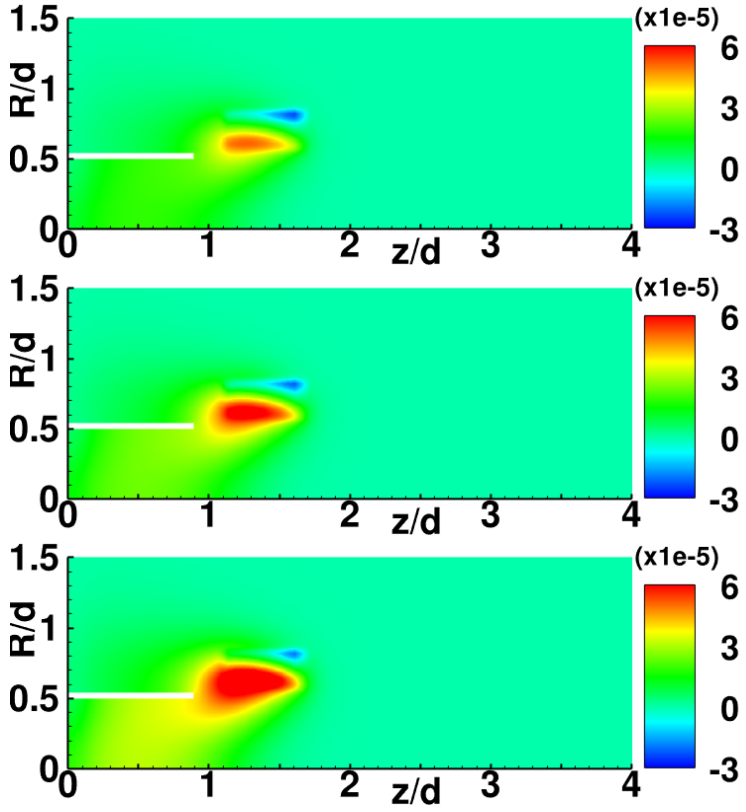

Figure 4.7: Field sensitivity x1e+5 of QoI-II to HO_2 for the KM (top), BM (middle), and LM (bottom)

shown scaled by the volume of the RoI. Figure 4.9 shows the ten most sensitive parameters for QoI-I and all three chemistry models. All three models share the most sensitive five parameters, although in a slightly different order. For instance the KM and BM share the most sensitive parameter, that for HO_2 + H $\rightleftharpoons$ OH + OH, which is second most sensitive for the LM. The next five most sensitive are similar, though each model has some sensitive parameters not listed in the top ten for the others. For all three models, the sensitivity of QoI-I, which is the integrated H_2O downstream of the flame, appears to be

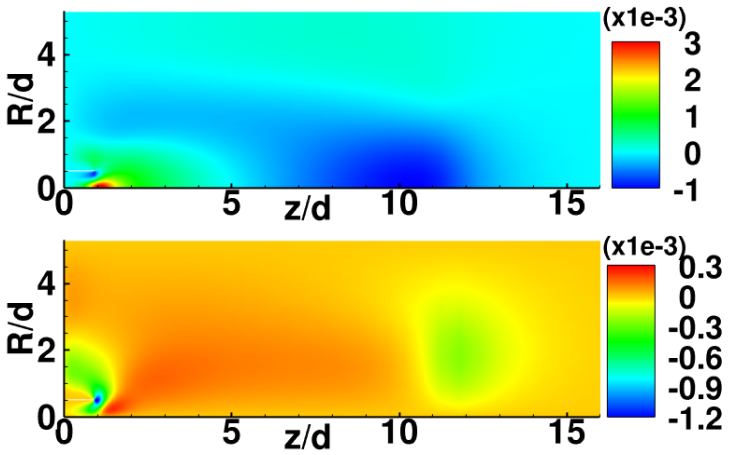

Figure 4.8: Field sensitivity of QoI-II to streamwise velocity (top) and radial velocity (bottom) for the KM

highly sensitive to the generation of and subsequent decomposition into OH of HO_2.

It is important to note the lack of agreement on the most sensitive parameters. Although the primal solutions for the three mechanisms are quite close, the models are sensitive to different sets of parameters. This arises from the fact that the models are calibrated using different sets of experiments, or the calibrated parameters obtained from different literature sources. Even if the same set of reactions are found to be most sensitive, the sensitivities are still evaluated at vastly different values of the underlying reaction rate parameters. This illustrates the fundamental problem in using parametric uncertainty to understand the performance of chemistry models.

4.4 Conclusions

We have defined a new quantity termed field sensitivity to compare chemistry models. The field sensitivity is shown to be the adjoint of the primal equations, and defines the sensitivity of a QoI to perturbations in the flow. The field sensitivity is a fundamental quantity, based on perturbations of measurable variables. Simulations of laminar flames were used to demonstrate that even if the primal solutions are sufficiently close, the field sensitivities could be very different. This illustrates that the models propagate perturbations in variables in different ways. The parametric sensitivities, which could be easily obtained from the adjoint solution, show that even for relatively simple fuels (such as H_2), there is considerable disagreement on the most sensitive parameters and their values. Due to issues with parametric sensitivity that were listed, this measure alone will not be useful in determining the accuracy and potential pitfalls of particular chemistry models. The following additional observations could be made about field sensitivity and adjoints

1. Convergence of chemistry mechanisms could be evaluated based on field sensitivity. For instance, the addition of pathways, reactions, or re-calibration of parameters could be evaluated by computing field sensitivity w.r.t variables of interest. If the end use is the prediction of certain QoIs, field sensitivity could inform us if more detailed mechanisms provide any additional gain in terms of sensitivities or if there is a marked change in the nature of the chemistry model. In a broader sense, it should be expected

that as chemistry models are refined, the field sensitivities, along with the primal solutions, should converge.

2. While it is relatively straightforward to determine field sensitivity in laminar flames, the adjoint approach itself has issues in chaotic and unsteady flows. For a general unsteady problem, the adjoints have to be propagated back in time. This would require that intermediate time primal solutions are available. While this is feasible in two-dimensional laminar flows, it is certainly not possible for large scale simulation methods such as direct numerical simulation (DNS) or large eddy simulation (LES). Both DNS and LES also model chaotic turbulent flow, which introduce other conceptual issues with adjoints [85]. In this regard, the adjoint of time-averaged DNS/LES solutions is a better starting point, especially if a statistically stationary state exists in the configurations considered.

3. Such measures of sensitivity are also useful in developing experimental configurations of maximum utility. To develop predictive models for the full scale systems, it is important to ensure that the models have the right sensitivity to perturbations in the flow. If the field sensitivity of a practical flow is evaluated, it could be used to develop simpler flow configurations to mimic this measure. Additionally, if certain regions of the flow are deemed important due to their large impact on the QoI, additional detailed measurements could be commissioned to ensure that the validation of the primal solutions is better characterized. In this sense, field sensitivity and

adjoints have a special role to play in uncertainty quantification and model validation.

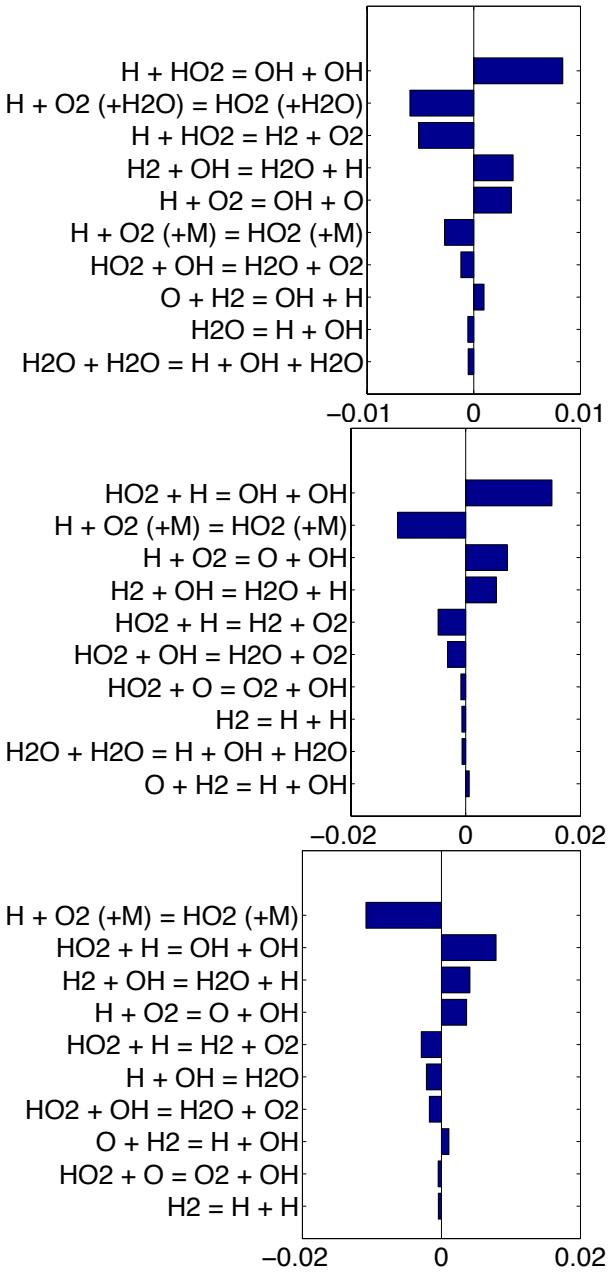

Figure 4.9: Top ten Arrhenius pre-exponential sensitivities for QoI-I for the KM (top), BM (middle), and LM (bottom)

Chapter 5

Conclusions

Bayesian uncertainty quantification and adjoint sensitivity methods provide a framework for investigating how simulations respond to chemistry modeling choices. The Bayesian method allows not only the calibration and improvement of chemistry models with experimental data, but also the quantification of how uncertainty in the model parameters themselves affects the outcome of simulations. Adjoint methods provide an ideal method for determining sensitivity of simulation results to model parameters given a limited number of relevant quantities and an arbitrary number of relevant model parameters. Together, these methods provide a means of characterizing and improving chemistry models. In this chapter key conclusions from the application of Bayesian UQ to chemistry models, the application of adjoint methods to efficiently determining sensitivities, and the application of adjoint methods to determining field sensitivity are stated. Finally, future directions of research for these topics are discussed.

5.1 Bayesian methods for chemistry model UQ

The inherent uncertainty in the determination of chemistry model parameters combined with the additional complications arising from the combination of independently calibrated parameter values necessitates the use of inversion methods for the calibration of full chemistry models. This inversion can proceed in a number of ways; however, the Bayesian method provides not only a set of nominal model parameter values, but also a multi-variate distribution on the parameters which can take an arbitrary form. The uncertainty in the model parameters also can be propagated forward in the simulations to provide an estimate of the uncertainty in the simulation results. Thus, the Bayesian framework provides the capability to update chemistry models as well as determine how precisely those models can give results given the inherent uncertainty in their parameter values.

The Bayesian framework was applied to a set of syngas chemistry models and a set of experimental flame speed results. After calibration to this data, the models provided a closer match to a set of test data, indicating an improvement in the model performance for that type of target experiment. More importantly the results of the Bayesian inversion gave a joint distribution on all of the calibrated parameters. This characterization of the uncertainty in the parameters was propagated through the simulations to show the resultant uncertainty in the flame speed results.

Therefore, the Bayesian framework provides a rigorous method for improving existing models through the incorporation of new experimental data.

Such a tool aids in practical engine design for two reasons. The uncertainty estimates obtained from the application allow for better characterization of the state of knowledge, which in turn leads to more robust decision making. Furthermore, the results indicate which models and model parameters are more important, thus leading to better allocation of resources.

5.2 Adjoint methods for determining chemistry model sensitivity

Simulation results depend upon the modeling choices made in developing those simulations. Each model can have a few to hundreds or thousands of model parameters, as in the case of chemistry models. With such a large number of parameters which potentially could alter the results of the simulations, these models require sensitivity studies to determine which parameters truly drive the relevant quantities from the simulation. These quantities, termed quantities of interest (QoIs), comprise the end goal of the simulations, and typically do not number very many. For such a situation, adjoint sensitivity methods provide an efficient means of determining parametric sensitivity of simulation behavior.

The set of adjoint equations for laminar, incompressible, variable density reacting flow have been developed. These equations have been verified for a one-dimensional burner stabilized flame configuration. After verification the adjoint equations were solved for a two-dimensional laminar hydrogen flame involving NO_x production. From the results of that simulation, the sensitivity

of two QoIs, average flame tip temperature and NO_x output, to the chemistry model parameters have been calculated. Results indicate which Arrhenius pre-exponential parameters are responsible for the flame tip temperature and NO_x output.

This methodology is a powerful tool that can inform decisions regarding how future validation experiments are designed and used. Adjoint sensitivity studies for specific QoIs which match experimental measurements can indicate how to carry out experiments to calibrate model parameters. Also, although developed here for laminar flames, the adjoint methodology easily can be extended to averaged turbulent simulations such as Reynolds-averaged Navier Stokes simulations, which are commonly used in the design cycle. Such methods can help elucidate which are the critical parameters for practical simulations, leading to refinement of experimental studies for improved model calibration.

5.3 Adjoint methods for determining field sensitivity

The adjoint solution provides not only parametric sensitivity information for the simulation, but also characterizes how the flow field variables themselves affect the QoIs in the simulation. This sensitivity, here termed field sensitivity, gives insight into how perturbations to the flow variables affect relevant quantities, which are typically downstream. For example, changes upstream of the flame can affect the temperature and extent of the flame.

For this work, the adjoint equations were solved for three laminar flame

simulations which used three separate chemistry models. Although the carried species and most of the included elementary reactions were the same for all three models, a few of the elementary reactions differed and some of the chemistry model parameter values varied amongst the different models. For those simulations, even though the primal results, especially the chosen QoIs, were very close in value, the field sensitivities showed discrepancies. This fact illustrates that the chemistry models in conjunction with the flow solution propagate perturbations to the primal variables in different ways.

Not only can field sensitivity be applied to laminar flames, but field sensitivity also can be applied to practical applications of averaged turbulent flows like RANS, averaged direct numerical simulations, or averaged large eddy simulations. Since the field sensitivity shows how perturbations affect the QoI, those regions deemed important in practical simulations due to their impact on the QoI can be useful for pointing out regions which require further characterization through experiment. Also, convergence of chemistry models can be evaluated based on field sensitivity. The addition of species and reactions, or in a broader sense chemical pathways, can be tested by examining the field sensitivity. If the additions introduce a marked change on the nature of how information is propagated in the simulation to the QoI, then those additions are important to the chemistry model. Generally, as chemistry models are refined, not only should the primal solutions converge, but the field sensitivities should converge as well.

5.4 Future directions

This work has focused on applications to simple chemistry models, namely those for hydrogen and syngas fuels. However, the adjoint sensitivity method provides great efficiency for models involving many parameters. Thus, more complex fuels can be the target of these sensitivity studies. Additionally, such sensitivity studies become more important as the experimental data becomes sparse. One example is soot formation in flames. This field lacks well-characterized experiments that provide rich data for use in model calibration and validation. Typically, only integrated measures of soot characteristics (volume fraction, for instance) are available. In some cases, only qualitative information concerning additional quantities such as PAH concentration are available. However, the models used involve many dozens of parameters in addition to the large number of chemistry model parameters. In these cases, it becomes necessary to understand the role of individual models and model parameters on the final measurable quantities. Adjoint sensitivity methods can fill this gap of knowledge and lead to improvement of soot modeling and ultimately soot simulation predictions.

Appendices

Appendix A

The syngas chemistry model of Davis [13]

Table A.1 lists the chemical reactions and the associated Arrhenius parameters for the Davis syngas chemistry model [13]. Reactions which include '+M' involve third body collisions for which the third body efficiencies are not listed here. Reactions which include (+M) are falloff reactions which utilize the Lindemann falloff function. Reactions labeled with a '*' indicate duplicate reactions. For those reactions, a single Arrhenius relation does not cover the behavior of the reaction well over a wide range of temperatures, thus the behavior is modified by the use of a duplicate reaction with different parameters. Together, the two Arrhenius equations better estimate the reaction rate for that elementary reaction.

Table A.1: The Arrhenius parameters for the Davis syngas chemistry model [13]; * refers to a duplicate reaction; units are in cm, s, mol, and cal

Reaction	A	η	E_A
$H+O_2 \rightleftharpoons O+OH$	2.65e+16	-0.671	17041
$O+H_2 \rightleftharpoons H+OH$	3.87e+4	2.7	6260
$OH+H_2 \rightleftharpoons H+H_2O$	2.16e+8	1.51	3430
$OH+OH \rightleftharpoons O+H_2O$	3.57e+4	2.4	-2110
$H+H+M \rightleftharpoons H_2+M$	1.00e+18	-1.0	0
$H+OH+M \rightleftharpoons H_2O+M$	2.20e+22	-2.0	0
$O+H+M \rightleftharpoons OH+M$	4.71e+18	-1.0	0
$O+O+M \rightleftharpoons O_2+M$	1.20e+17	-1.0	0
$H+O_2(+M) \rightleftharpoons HO_2(+M)$	4.65e+12	0.44	0
	5.75e+19	-1.4	0
$H_2+O_2 \rightleftharpoons HO_2+H$	7.40e+5	2.433	53502
$OH+OH(+M) \rightleftharpoons H_2O_2(+M)$	7.40e+13	-0.37	0
	1.34e+17	-0.584	-2293
$HO_2+H \rightleftharpoons OH+OH$	7.08e+13	0.0	295
$HO_2+O \rightleftharpoons OH+O_2$	2.00e+13	0.0	0
$HO_2+OH \rightleftharpoons O_2+H_2O$	2.90e+13	0.0	-500
$HO_2+OH \rightleftharpoons O_2+H_2O^*$	1.00e+16	0.0	17330
$HO_2+HO_2 \rightleftharpoons O_2+H_2O_2$	1.30e+11	0.0	-1630
$HO_2+HO_2 \rightleftharpoons O_2+H_2O_2^*$	4.20e+14	0.0	12000
$H_2O_2+H \rightleftharpoons HO_2+H_2$	1.21e+7	0.0	25200
$H_2O_2+H \rightleftharpoons OH+H_2O$	2.41e+13	0.0	3970
$H_2O_2+O \rightleftharpoons OH+HO_2$	9.63e+6	0.0	23970
$H_2O_2+OH \rightleftharpoons HO_2+H_2O$	2.00e+12	0.0	427
$H_2O_2+OH \rightleftharpoons HO_2+H_2O^*$	2.67e+41	0.0	-737600
$CO+O(+M) \rightleftharpoons CO_2(+M)$	1.80e+10	0.0	2384
	1.55e+24	-2.79	4191
$CO+OH \rightleftharpoons CO_2+H$	9.60e+11	0.14	7352
$CO+OH \rightleftharpoons CO_2+H^*$	7.32e+10	0.03	-16
$CO+O_2 \rightleftharpoons CO_2+O$	2.53e+12	0.0	47700
$CO+HO_2 \rightleftharpoons CO_2+OH$	3.01e+13	0.0	23000
$HCO+H \rightleftharpoons CO+H_2$	1.20e+14	0.0	0
$HCO+O \rightleftharpoons CO+OH$	3.00e+13	0.0	0
$HCO+O \rightleftharpoons CO_2+H$	3.00e+13	0.0	0
$HCO+OH \rightleftharpoons CO+H_2O$	3.02e+13	0.0	0
$HCO+M \rightleftharpoons CO+H+M$	9.35e+16	-1.0	17000
$HCO+O_2 \rightleftharpoons CO+HO_2$	1.20e+10	0.807	-727

Appendix B

Bayesian representation of the MUM-PCE approach of Sheen and Wang

The basic approach of Sheen and Wang [14, 21, 22] solves a limited form of the Bayesian inverse problem, and thus follows many of the ideas of Bayesian uncertainty quantification. Given a set of experimental results, the method solves for a nominal set of parameters and the covariance values amongst them. Such parameter determination is used to calculate the resultant uncertainties which are reduced in relation to uncertainties resulting from the initial values and variances for all parameters. We provide this discussion as a means of evaluating model parameter calibration processes by their effect on the posterior distribution.

B.1 The Sheen and Wang method

In the Sheen and Wang method, the kinetics parameters involved are the pre-exponential coefficients k_i. Each parameter is normalized to a range of -1 to 1 with

$$x_i = \frac{\ln k_i/k_{i,0}}{\ln f_i}, \tag{B.1}$$

where $k_{i,0}$ is the pre-calibrated value for k_i and f_i is the multiplicative uncertainty factor. The method proceeds by treating the set of parameters $\boldsymbol{x}$ as a set of random variables with the following polynomial chaos expansion:

$$\boldsymbol{x} = \boldsymbol{x}_0 + \sum_{i=1}^{M} \boldsymbol{\alpha}_i \xi_i + \sum_{i=1}^{M} \sum_{j=1}^{M} \boldsymbol{\beta}_{ij} \xi_i \xi_j + ..., \tag{B.2}$$

where ξ_i are standard random variables, typically treated by the method as standard normal random variables, $\boldsymbol{\alpha}_i$ and $\boldsymbol{\beta}_{ij}$ are the expansion coefficients, and M is the number of random variables used in the expansion. This expansion is simplified to the following in order to allow the analytical simplifications of the method:

$$\boldsymbol{x} = \boldsymbol{x}_0 + \sum_{i=1}^{M} \boldsymbol{\alpha}_i \xi_i. \tag{B.3}$$

The parameters $\boldsymbol{x}$ form a multivariate Gaussian distribution with mean $\boldsymbol{x}_0$ and covariance matrix $\boldsymbol{\Sigma} = \boldsymbol{\alpha}^T \boldsymbol{\alpha}$.

The Sheen and Wang method replaces the target combustion models with surrogate models, quadratic response surfaces, the use of which has been deemed Solution Mapping [63]. The response surfaces are generated from selected simulations of the target combustion model. The selected simulations are intended to provide response surface support over the range of necessary simulation conditions. The response surfaces consist of the nominal modeled value $\eta_{r,0}$ and sets of coefficients a_i and b_{ij} for each experimental condition. The modeled value η_r for each experiment r is calculated as

$$\eta_r(\boldsymbol{x}) = \eta_{r,0} + \sum_{i=1}^{N} a_i x_i + \sum_{i=1}^{N} \sum_{j \geq 1}^{N} b_{ij} x_i x_j, \tag{B.4}$$

where N is the number of optimized parameters.

Determination of the parameters in the Sheen and Wang method involves two steps. Step one is the optimization of the parameter nominal values. This step minimizes the objective function Φ, which is a sum of the least squares difference between the target experimental results and the simulation results and a parameter weighting term,

$$\Phi(\boldsymbol{x}) = \sum_{r=1}^{n} \left(\frac{\eta_r(\boldsymbol{x}) - \eta_r^{obs}}{\sigma_r^{obs}} \right)^2 + \sum_{k=1}^{N} 4x_k^2, \tag{B.5}$$

where n is the number of experimental targets. Step two is determination of the parameter covariance matrix. The objective function Φ is employed now in the construction of the PDF of a multivariate Gaussian of the parameters,

$$p(\boldsymbol{x}) = Aexp(-0.5\Phi(\boldsymbol{x})), \tag{B.6}$$

where A is a normalization constant. The distribution has its mean as the optimal parameter values $\boldsymbol{x}^*$ and has covariance matrix $\boldsymbol{\Sigma}$. Linearizing the response surface about the optimal parameter values leads to an expression for the covariance matrix,

$$\boldsymbol{\Sigma} = \left[\sum_{r=1}^{n} \frac{1}{(\sigma_r^{obs})^2} (\boldsymbol{b}\boldsymbol{x}_{\boldsymbol{0}}^{*}\boldsymbol{x}_{\boldsymbol{0}}^{*\boldsymbol{T}}\boldsymbol{b} + \boldsymbol{a}\boldsymbol{x}^{\boldsymbol{T}}\boldsymbol{b} + \boldsymbol{b}^{\boldsymbol{T}}\boldsymbol{x}\boldsymbol{a}^{\boldsymbol{T}} + \boldsymbol{a}\boldsymbol{a}^{\boldsymbol{T}}) + 4\mathbf{I} \right]^{-1}. \tag{B.7}$$

This expression is solved for the polynomial chaos expansion coefficients $\boldsymbol{\alpha}^*$ from the multivariate Gaussian treatment of $\boldsymbol{x}$, for which

$$\boldsymbol{x}^* = \boldsymbol{x}_0^* + \sum_{i=1}^{M} \boldsymbol{\alpha}_i^* \xi_i, \tag{B.8}$$

with mean $\boldsymbol{x}_0^*$ and covariance matrix $\boldsymbol{\Sigma} = \boldsymbol{\alpha}^{*T}\boldsymbol{\alpha}^*$.

B.2 The Bayesian derivation of the Sheen and Wang method

The Bayesian method aims to minimize the difference between experimental results and simulation results using an objective function, the likelihood function. Given Gaussian experimental and model form error, the likelihood function starts from the following form:

$$\pi(\boldsymbol{x};\boldsymbol{\eta}^{obs}) = \frac{1}{(2\pi)^{n/2}|\boldsymbol{\Sigma}|^{1/2}} \exp\left[-\frac{1}{2}\left(\boldsymbol{\eta}(\boldsymbol{x}) - \boldsymbol{\eta}^{obs}\right)^T \boldsymbol{\Sigma}^{-1}\left(\boldsymbol{\eta}(\boldsymbol{x}) - \boldsymbol{\eta}^{obs}\right)\right], \tag{B.9}$$

where the covariance matrix $\boldsymbol{\Sigma}$ serves as the error model term. The Sheen and Wang method uses an additive error term which involves only the experimental error, which can be written as

$$\Sigma_{ij} = \begin{cases} \sigma_i^{obs} & \text{for } i = j \\ 0 & \text{for } i \neq j. \end{cases} \tag{B.10}$$

Applying this assumption to the Bayesian likelihood leads to a simplification of the likelihood to the following

$$\pi(\boldsymbol{x};\boldsymbol{\eta}^{obs}) = \frac{1}{(2\pi)^{n/2}(\prod_{r=1}^{n}\sigma_r^{obs})^{1/2}} \exp\left[-\frac{1}{2}\sum_{r=1}^{n}\left(\frac{\eta_r(\boldsymbol{x}) - \eta_r^{obs}}{\sigma_r^{obs}}\right)^2\right]. \tag{B.11}$$

The Sheen and Wang method treats the priors typically as normal distributions with zero mean and standard deviation of 0.5, thus

$$p_{prior}(\boldsymbol{x}) = \frac{1}{(0.5\pi)^{N/2}} \exp\left[-\frac{1}{2}\sum_{i=1}^{N}(2x_i)^2\right]. \tag{B.12}$$

Substituting the prior and likelihood function into the equation for the posterior parameters (2.2) results in

$$p(\boldsymbol{x}) = A \exp\left[-\frac{1}{2} \sum_{r=1}^{n} \left(\frac{\eta_r(\boldsymbol{x}) - \eta_r^{obs}}{\sigma_r^{obs}} \right)^2 - \frac{1}{2} \sum_{i=1}^{N} (2x_i)^2 \right], \tag{B.13}$$

where A again is a normalization constant. Therefore, with the additive experimental error model and normal priors, the Bayesian posterior is equivalent to the Sheen and Wang assumed parameter probability (B.6) with objective function (B.5).

Proceeding from the expression for the parameter joint distribution, the Sheen and Wang method employs additional assumptions which allow analytical calculation of the distributions rather than by Monte Carlo sampling. These simplifications reduce the complexity of the solution method and allow the uncertainty results to be calculated rapidly; however, they also lead to restrictions on the flexibility of results. The following list outlines four of the primary simplifications of the SW method.

(1) The target combustion models are replaced by surrogate models.

(2) The parameter distributions are expressed as first order polynomial chaos expansions.

(3) The surrogate models are linearized during calculation of parameter covariance and thus for resultant uncertainty.

(4) The error model involves only additive Gaussian experimental error.

The Sheen and Wang method replaces the target combustion models with quadratic response surfaces which act as surrogate models. While simplifying the combustion model to a mere algebraic relationship of the kinetics parameters, the response surface substitution requires that the model response follow a smooth quadratic response to changes in those parameters. The random variable treatment of those parameters is accomplished with first order polynomial chaos expansions. This simplification requires that the parameters be distributed in a multivariate Gaussian distribution. However, this assumption combined with the algebraic relationship of the response surfaces allows the analytical simplification to the final equations for nominal parameter values and covariances. The calculation of the model parameter covariances involves the linearization of the response surfaces about the nominal parameter values. This simplification allows further analytical simplification for the parameter covariances. Additionally, the error model in this method involves only the experimental error, which is equivalent to an constant additive error model in the Bayesian framework, where it manifests itself in the likelihood function. The error term is distributed as a zero mean Gaussian, which maintains the simplicity of the parameter covariance calculation. Furthermore, this error term precludes the possibility of including model form error which may be present in the modeling of the target combustion experiments in the uncertainty quantification process.

The result of these simplifications is a method that limits model parameters and resultant model uncertainties to multivariate Gaussian distributions.

Input prior information about the model parameters must also be limited to a collection of univariate Gaussian distributions. Nonetheless, the method follows the general methodology of the Bayesian framework. A physical phenomenon (say, laminar flame speed for syngas combustion) is approximated by a mathematical model which involves model (kinetics) parameters. A set of experimental data (experimental flame speeds) is assembled to update the model parameters. Based upon the difference between the experimental and modeled results (flame speeds), the parameter nominal values and covariances are updated, and the posterior quantity (flame speed) uncertainty is determined.

Appendix C

Incompressible, variable density adjoint equations

C.1 Derivation

This section derives the dual (adjoint) problem corresponding to the primal problem outlined in §3.2.1. The derivation proceeds starting from the steady state primal problem governing equations as follows:

$$\frac{\partial \rho u_j}{\partial x_j} = 0 \tag{C.1}$$

$$\frac{\partial}{\partial x_j}\left(\rho u_j u_i\right) + \frac{\partial p'}{\partial x_i} = \frac{\partial \tau_{ji}}{\partial x_j}, \tag{C.2}$$

$$\frac{\partial}{\partial x_j}\left(\rho u_j h\right) - \frac{\partial}{\partial x_j}\left(\rho\alpha\frac{\partial h}{\partial x_j}\right) = \omega_h, \tag{C.3}$$

$$\frac{\partial}{\partial x_j}\left(\rho u_j Y_k\right) - \frac{\partial}{\partial x_j}\left(\rho D_k\frac{\partial Y_k}{\partial x_j}\right) = \omega_{Y_k}. \tag{C.4}$$

for which the viscous stress tensor τ_{ji} can be written

$$\tau_{ji} = \mu\left(\frac{\partial u_i}{\partial x_j} + \frac{\partial u_j}{\partial x_i} - \frac{2}{3}\frac{\partial u_k}{\partial x_k}\delta_{ij}\right). \tag{C.5}$$

Additionally, the equation of state $P^0 = \rho RT$ and the definition of enthalpy $h = c_p T$ provide constraints on the system. Since ρ and h are related, ρ will be written as a function of h, thus

$$\rho = \frac{P^0 c_p}{Rh}. \tag{C.6}$$

C.1.1 Introductory Considerations

Let $U = [p', u_i, h, Y_k]^T$ denote the primal variables and $\mathcal{R}(U) = [R_C, R_{M_i}, R_E, R_{S_k}]^T$ denote the residual operator corresponding to the primal PDEs. Further, let the quantity of interest, or cost function, be written

$$\mathcal{J}(U) = \int_\Omega g(U)\, d\mathbf{x}, \tag{C.7}$$

and let $\Phi = [\varphi_p, \varphi_{u_i}, \varphi_h, \varphi_{Y_k}]^T$ denote the adjoint variables. Then, the Lagrangian of the system can be written as

$$\mathcal{L}(U, \Phi) \equiv \mathcal{J}(U) + \int_\Omega \Phi^T \mathcal{R}(U)\, d\mathbf{x}. \tag{C.8}$$

To derive the adjoint equations, examine the first variation of the Lagrangian with respect to U. The Lagrangian must be stationary with respect to the first variation W, thus

$$\begin{aligned} \mathcal{L}(U, \Phi) &= \mathcal{L}(U + W, \Phi) \\ &= \mathcal{L}(U, \Phi) + \mathcal{L}'[U](W, \Phi) \end{aligned} \tag{C.9}$$

Specifically, the adjoint Φ solves the following problem: find Φ such that

$$\mathcal{L}'[U](W, \Phi) = 0, \tag{C.10}$$

for all admissible variations $W = [q, w_i, \delta h, z_k]$ of U, where $\mathcal{L}'[U]$ denotes the Frechet derivative of $\mathcal{L}$ with respect to U. Clearly,

$$\mathcal{L}'[U](W, \Phi) = \mathcal{J}'[U](W) - \int_\Omega \Phi^T \mathcal{R}'[U](W)\, d\mathbf{x}. \tag{C.11}$$

Thus, to begin the derivation, $\mathcal{R}'[U](W)$ must be found.

C.1.2 Variations of the Primal Residual

The governing equations are written in residual form and then perturbed by variations of the independent variables. For the continuity equation, the residual equation is the following

$$R_C(U+W) = \frac{\partial}{\partial x_i}\left[(\rho+\delta\rho)\left(u_i+w_i\right)\right], \tag{C.12}$$

thus,

$$R'_C[U](W) = \frac{\partial}{\partial x_i}\left[-\frac{\rho}{h}u_i\delta h + \rho w_i\right]. \tag{C.13}$$

For the momentum equation, the residual equation is the following

$$\begin{aligned} R_{M_i}(U+W) = &\frac{\partial}{\partial x_j}\left[(\rho+\delta\rho)(u_j+w_j)(u_i+w_i)\right] \\ &+ \frac{\partial}{\partial x_j}(p'+q)\delta_{ji} - \frac{\partial}{\partial x_j}\tau_{ji}(U+W). \end{aligned} \tag{C.14}$$

It is straightforward to show that, under the assumption of constant viscosity, the viscous shear stress is linear in the state:

$$\tau_{ji}(U+W) = \tau_{ji}(U) + \tau_{ji}(W). \tag{C.15}$$

Therefore, the variation of the momentum residual becomes the following

$$\begin{aligned} R'_{M_i}[U](W) = &\frac{\partial}{\partial x_j}\left(-\frac{\rho}{h}u_ju_i\delta h\right) + \frac{\partial}{\partial x_j}\left(\rho w_j u_i\right) \\ &+ \frac{\partial}{\partial x_j}\left(\rho u_j w_i\right) + \frac{\partial q}{\partial x_j}\delta_{ji} - \frac{\partial \tau_{ji}(W)}{\partial x_j}. \end{aligned} \tag{C.16}$$

For the enthalpy equation, since ρ and h are related, the enthalpy residual equation is the following

$$\begin{aligned} R_E(U+W) = &\frac{\partial}{\partial x_j}\left(\frac{P_0 c_p}{R}(u_j+w_j)\right) \\ &- \frac{\partial}{\partial x_j}\left((\rho+\delta\rho)\alpha\frac{\partial(h+\delta h)}{\partial x_j}\right) - \omega_h(U+W), \end{aligned} \tag{C.17}$$

which implies that

$$R'_E[U](W) = \frac{\partial}{\partial x_j}\left(\frac{P_0 c_p}{R} w_j\right) + \frac{\partial}{\partial x_j}\left(\frac{1}{h}\rho\alpha\frac{\partial h}{\partial x_j}\delta h\right) - \frac{\partial}{\partial x_j}\left(\rho\alpha\frac{\partial \delta h}{\partial x_j}\right) - \frac{\partial \omega_h}{\partial U}W. \tag{C.18}$$

For the species equations, the residual equations are the following

$$R_{S_k}(U+W) = \frac{\partial}{\partial x_j}\left[(\rho+\delta\rho)(u_j+w_j)(Y_k+z_k)\right] - \frac{\partial}{\partial x_j}\left((\rho+\delta\rho)D_k\frac{\partial(Y_k+z_k)}{\partial x_j}\right) - \omega_{Y_k}(U+W), \tag{C.19}$$

which implies that

$$R'_{S_k}[U](W) = \frac{\partial}{\partial x_j}\left(-\frac{\rho}{h}u_j Y_k \delta h\right) + \frac{\partial}{\partial x_j}\left(\rho w_j Y_k\right) + \frac{\partial}{\partial x_j}\left(\rho u_j z_k\right) - \frac{\partial}{\partial x_j}\left(-\frac{\rho}{h}D_k\frac{\partial Y_k}{\partial x_j}\delta h + \rho D_k\frac{\partial z_k}{\partial x_j}\right) - \frac{\partial \omega_{Y_k}}{\partial U}W. \tag{C.20}$$

After the collection of terms and transformation into the form necessary

for (C.11), the above residual equations take the following form:

$$\begin{aligned}
\int_\Omega \Phi^T \mathcal{R}'[U](W) d\mathbf{x} = & \underbrace{\int_\Omega \varphi_p \left[\frac{\partial}{\partial x_i} \left(-\frac{\rho}{h} u_i \delta h + \rho w_j \right) \right] d\mathbf{x}}_{\text{Continuity}} \\
& + \underbrace{\int_\Omega \varphi_{u_i} \left[\frac{\partial}{\partial x_j} \left(-\frac{\rho}{h} u_j u_i \delta h \right) + \frac{\partial}{\partial x_j} \left(\rho w_j u_i \right) \right.}_{\text{Momentum}} \\
& \qquad \underbrace{\left. + \frac{\partial}{\partial x_j} \left(\rho u_j w_i \right) + \frac{\partial q}{\partial x_j} \delta_{ji} - \frac{\partial \tau_{ji}(W)}{\partial x_j} \right] d\mathbf{x}}_{\text{Momentum}} \\
& + \underbrace{\int_\Omega \varphi_h \left[\frac{\partial}{\partial x_j} \left(\frac{P_0 c_p}{R} w_j \right) + \frac{\partial}{\partial x_j} \left(\frac{1}{h} \rho \alpha \frac{\partial h}{\partial x_j} \delta h \right) \right.}_{\text{Enthalpy}} \\
& \qquad \underbrace{\left. - \frac{\partial}{\partial x_j} \left(\rho \alpha \frac{\partial \delta h}{\partial x_j} \right) - \frac{\partial \omega_h}{\partial U} W \right] d\mathbf{x}}_{\text{Enthalpy}} \\
& + \underbrace{\int_\Omega \varphi_{Y_k} \left[\frac{\partial}{\partial x_j} \left(-\frac{1}{h} \rho u_j Y_k \delta h \right) + \frac{\partial}{\partial x_j} \left(\rho Y_k w_j \right) \right.}_{\text{Species}} \\
& \qquad + \frac{\partial}{\partial x_j} \left(\rho u_j z_k \right) + \frac{\partial}{\partial x_j} \left(\frac{1}{h} \rho D_k \frac{\partial Y_k}{\partial x_j} \delta h \right) \\
& \qquad \underbrace{\left. - \frac{\partial}{\partial x_j} \left(\rho D_k \frac{\partial z_k}{\partial x_j} \right) - \frac{\partial \omega_{Y_k}}{\partial U} W \right] d\mathbf{x}}_{\text{Species}}
\end{aligned} \tag{C.21}$$

In the above equation, several terms include the variations W within derivatives. Integration by parts can be used to move the variations W outside the derivatives.

Integration by parts transforms continuity to the following

$$\begin{aligned}
\int_\Omega \varphi_p R'_C[U](W) \, d\mathbf{x} &= \int_\Omega \varphi_p \frac{\partial}{\partial x_i} \left(-\frac{\rho}{h} u_i \delta h + \rho w_j \right) d\mathbf{x} \\
&= \mathrm{B_C} + \int_\Omega \left(\frac{\rho}{h} u_i \frac{\partial \varphi_p}{\partial x_i} \delta h \right) d\mathbf{x} - \int_\Omega \left(\frac{\partial \varphi_p}{\partial x_i} \rho w_i \right) d\mathbf{x}
\end{aligned} \tag{C.22}$$

where $\mathrm{B_C}$ includes the boundary terms. Specifically,

$$\mathrm{B_C} = -\int_{\partial\Omega} \varphi_p \frac{\rho}{h} u_i n_i \delta h \, ds + \int_{\partial\Omega} \varphi_p \rho n_i w_i \, ds, \tag{C.23}$$

where n_i is the ith component of the outward pointing unit normal vector.

For momentum integration by parts leads to the following

$$\begin{aligned}
\int_\Omega \varphi_{u_i} R'_{M_i}[U](W)\, d\mathbf{x} &= \int_\Omega \varphi_{u_i} \Bigg(\frac{\partial}{\partial x_j}\left(-\frac{\rho}{h} u_j u_i \delta h\right) + \frac{\partial}{\partial x_j}\left(\rho w_j u_i\right) \\
&\qquad + \frac{\partial}{\partial x_j}\left(\rho u_j w_i\right) + \frac{\partial q}{\partial x_j}\delta_{ji} - \frac{\partial \tau_{ji}(W)}{\partial x_j} \Bigg) d\mathbf{x} \\
&= \mathrm{B_{M1}} + \int_\Omega \Bigg(\frac{\partial \varphi_{u_i}}{\partial x_j} \frac{\rho}{h} u_j u_i \delta h - \frac{\partial \varphi_{u_i}}{\partial x_j} \rho u_i w_j \\
&\qquad - \frac{\partial}{\partial x_j}\left(\rho u_j \varphi_{u_i}\right) w_i - \frac{\partial \varphi_{u_i}}{\partial x_j} q \delta_{ji} \Bigg) d\mathbf{x} \\
&\qquad + \int_\Omega \frac{\partial \varphi_{u_i}}{\partial x_j} \tau_{ji}(W)\, d\mathbf{x} \\
&= \mathrm{B_{M1}} + \mathrm{B_{M2}} + \int_\Omega \Bigg(\frac{\partial \varphi_{u_i}}{\partial x_j} \frac{\rho}{h} u_j u_i \delta h - \frac{\partial \varphi_{u_i}}{\partial x_j} \rho u_i w_j \\
&\qquad - \frac{\partial}{\partial x_j}\left(\rho u_j \varphi_{u_i}\right) w_i - \frac{\partial \varphi_{u_i}}{\partial x_j} q \delta_{ji} \Bigg) d\mathbf{x} \\
&\qquad - \int_\Omega w_j \Bigg[\frac{\partial}{\partial x_i}\left(\mu\left(\frac{\partial \varphi_{u_i}}{\partial x_j} + \frac{\partial \varphi_{u_j}}{\partial x_i}\right)\right) \\
&\qquad - \frac{\partial}{\partial x_j}\left(\frac{2}{3}\mu \frac{\partial \varphi_{u_k}}{\partial x_k}\right) \Bigg] d\mathbf{x} \\
&= \mathrm{B_{M1}} + \mathrm{B_{M2}} + \int_\Omega \Bigg(\frac{\partial \varphi_{u_i}}{\partial x_j} \frac{\rho}{h} u_j u_i \delta h - \frac{\partial \varphi_{u_i}}{\partial x_j} \rho u_i w_j \\
&\qquad - \frac{\partial}{\partial x_j}\left(\rho u_j \varphi_{u_i}\right) w_i - \frac{\partial \varphi_{u_i}}{\partial x_j} q \delta_{ji} \Bigg) d\mathbf{x} \\
&\qquad - \int_\Omega w_j \frac{\partial \tau_{ij}(\varphi_u)}{\partial x_i}\, d\mathbf{x},
\end{aligned} \tag{C.24}$$

where $\mathrm{B_{M1}}$ and $\mathrm{B_{M2}}$ are boundary terms. Specifically,

$$\mathrm{B_{M1}} = \int_{\partial\Omega} \varphi_{u_i} \left(-\frac{\rho}{h} u_j u_i \delta h + \rho u_i w_j + \rho u_j w_i + q\delta_{ji} - \tau_{ji}(W) \right) n_j \, ds, \quad \text{(C.25)}$$

$$\begin{aligned} \mathrm{B_{M2}} &= \int_{\partial\Omega} w_j \left[\mu \left(\frac{\partial \varphi_{u_i}}{\partial x_j} + \frac{\partial \varphi_{u_j}}{\partial x_i} \right) - \frac{2}{3} \mu \frac{\partial \varphi_{u_k}}{\partial x_k} n_j \right] ds \\ &= \int_{\partial\Omega} w_j \tau_{ji}(\varphi_u) n_i \, ds, \end{aligned} \quad \text{(C.26)}$$

where n_i is the ith component of the outward pointing unit normal vector.

Integration by parts modifies the enthalpy contribution in the following fashion:

$$\begin{aligned} \int_\Omega \varphi_h R'_E[U](W) \, d\mathbf{x} &= \int_\Omega \varphi_h \left[\frac{\partial}{\partial x_j} \left(\frac{P_0 c_p}{R} w_j \right) + \frac{\partial}{\partial x_j} \left(\frac{\rho}{h} \alpha \frac{\partial h}{\partial x_j} \delta h \right) \right. \\ &\qquad \left. - \frac{\partial}{\partial x_j} \left(\rho \alpha \frac{\partial \delta h}{\partial x_j} \right) - \frac{\partial \omega_h}{\partial U} W \right] d\mathbf{x} \\ &= B_{E1} - \int_\Omega \frac{P_0 c_p}{R} \frac{\partial \varphi_h}{\partial x_j} w_j \, d\mathbf{x} \\ &\quad + \int_\Omega \frac{\partial \varphi_h}{\partial x_j} \left(-\frac{\rho}{h} \alpha \frac{\partial h}{\partial x_j} \delta h + \rho \alpha \frac{\partial \delta h}{\partial x_j} \right) d\mathbf{x} \\ &\quad - \int_\Omega \varphi_h \frac{\partial \omega_h}{\partial U} W \, d\mathbf{x} \\ &= B_{E1} + B_{E2} + - \int_\Omega \frac{P_0 c_p}{R} \frac{\partial \varphi_h}{\partial x_j} w_j \, d\mathbf{x} \\ &\quad - \int_\Omega \frac{\rho}{h} \alpha \frac{\partial h}{\partial x_j} \frac{\partial \varphi_h}{\partial x_j} \delta h \, d\mathbf{x} - \int_\Omega \frac{\partial}{\partial x_j} \left(\rho \alpha \frac{\partial \varphi_h}{\partial x_j} \right) \delta h \, d\mathbf{x} \\ &\quad - \int_\Omega \varphi_h \frac{\partial \omega_h}{\partial U} W \, d\mathbf{x} \end{aligned} \quad \text{(C.27)}$$

where $\mathrm{B_{E1}}$ and $\mathrm{B_{E2}}$ are boundary terms. Specifically,

$$\mathrm{B_{E1}} = \int_{\partial\Omega} \varphi_h \left(\frac{P_0 c_p}{R} w_j + \frac{\rho}{h} \alpha \frac{\partial h}{\partial x_j} \delta h - \rho \alpha \frac{\partial \delta h}{\partial x_j} \right) n_j \, ds, \quad \text{(C.28)}$$

$$\mathrm{B_{E2}} = \int_{\partial\Omega} \rho \alpha \frac{\partial \varphi_h}{\partial x_j} n_j \delta h \, ds, \quad \text{(C.29)}$$

where n_i is the ith component of the outward pointing unit normal vector.

For the species residual equations, integration by parts leads to the following

$$\begin{aligned}
\int_\Omega \varphi_{Y_k} R'_{S_k}[U](W)\,d\mathbf{x} &= \int_\Omega \varphi_{Y_k}\left[\frac{\partial}{\partial x_j}\left(-\frac{1}{h}\rho u_j Y_k \delta h\right) + \frac{\partial}{\partial x_j}\left(\rho Y_k w_j\right)\right. \\
&\qquad \left. + \frac{\partial}{\partial x_j}\left(\rho u_j z_k\right)\right] d\mathbf{x} + \int_\Omega \varphi_{Y_k}\frac{\partial}{\partial x_j}\left(\frac{1}{h}\rho D_k \frac{\partial Y_k}{\partial x_j}\delta h\right) d\mathbf{x} \\
&\quad - \int_\Omega \varphi_{Y_k}\frac{\partial}{\partial x_j}\left(\rho D_k \frac{\partial z_k}{\partial x_j}\right) d\mathbf{x} - \int_\Omega \varphi_{Y_k}\frac{\partial \omega_{Y_k}}{\partial U} W\,d\mathbf{x} \\
&= B_{S1} + \int_\Omega \frac{1}{h}\rho u_j Y_k \frac{\partial \varphi_{Y_k}}{\partial x_j}\delta h\,d\mathbf{x} - \int_\Omega \rho Y_k \frac{\partial \varphi_{Y_k}}{\partial x_j} w_j\,d\mathbf{x} \\
&\quad - \int_\Omega \rho u_j \frac{\partial \varphi_{Y_k}}{\partial x_j} z_k\,d\mathbf{x} \\
&\quad + \int_\Omega \frac{\partial \varphi_{Y_k}}{\partial x_j}\left(-\frac{1}{h}\rho D_k \frac{\partial Y_k}{\partial x_j}\delta h + \rho D_k \frac{\partial z_k}{\partial x_j}\right) d\mathbf{x} \\
&\quad - \int_\Omega \varphi_{Y_k}\frac{\partial \omega_{Y_k}}{\partial U} W\,d\mathbf{x} \\
&= B_{S1} + B_{S2} + \int_\Omega \frac{1}{h}\rho u_j Y_k \frac{\partial \varphi_{Y_k}}{\partial x_j}\delta h\,d\mathbf{x} \\
&\quad - \int_\Omega \rho Y_k \frac{\partial \varphi_{Y_k}}{\partial x_j} w_j\,d\mathbf{x} - \int_\Omega \rho u_j \frac{\partial \varphi_{Y_k}}{\partial x_j} z_k\,d\mathbf{x} \\
&\quad - \int_\Omega \frac{1}{h}\rho D_k \frac{\partial Y_k}{\partial x_j}\frac{\partial \varphi_{Y_k}}{\partial x_j}\delta h\,d\mathbf{x} - \int_\Omega \frac{\partial}{\partial x_j}\left(\rho D_k \frac{\partial \varphi_{Y_k}}{\partial x_j}\right) z_k\,d\mathbf{x} \\
&\quad - \int_\Omega \varphi_{Y_k}\frac{\partial \omega_{Y_k}}{\partial U} W\,d\mathbf{x} \qquad \text{(C.30)}
\end{aligned}$$

where B_{S1} and B_{S2} are boundary terms. Specifically,

$$B_{S1} = \int_{\partial\Omega} \varphi_{Y_k} \bigg(-\frac{1}{h}\rho u_j Y_k \delta h + \rho Y_k w_j + \rho u_j z_k + \frac{1}{h}\rho D_k \frac{\partial Y_k}{\partial x_j}\delta h - \rho D_k \frac{\partial z_k}{\partial x_j}\bigg) n_j \, ds, \tag{C.31}$$

$$B_{S2} = \int_{\partial\Omega} \rho D_k \frac{\partial \varphi_{Y_k}}{\partial x_j} n_j z_k \, ds, \tag{C.32}$$

where n_i is the ith component of the outward pointing unit normal vector.

C.2 Governing equations

Again, consider each component of the variation W independently. From the pressure variation q, the derivation leads to the adjoint continuity equation, from the velocity variation w_i, to the adjoint momentum equations, from the density and enthalpy variations $\delta\rho$ and δh, to the adjoint enthalpy equation, and from the species variations z_k to the adjoint species equations. Therefore, the incompressible variable density steady-state Navier-Stokes adjoint equations can be written as the following:

$$\frac{\partial \varphi_{u_i}}{\partial x_i} = -\frac{\partial g}{\partial p'} \tag{C.33}$$

$$-\frac{\partial \rho u_j \varphi_{u_i}}{\partial x_j} - \frac{\partial \varphi_{u_j}}{\partial x_i}\rho u_j - \frac{\partial}{\partial x_j}\tau_{ji}(\varphi_u) - \frac{P_0 c_p}{R}\frac{\partial \varphi_h}{\partial x_i} - \rho \sum_k Y_k \frac{\partial \varphi_{Y_k}}{\partial x_i} - \rho \frac{\partial \varphi_p}{\partial x_i} = \frac{\partial g}{\partial u_i} \tag{C.34}$$

$$-\frac{\partial}{\partial x_j}\left(\rho\alpha\frac{\partial\varphi_h}{\partial x_j}\right)-\frac{1}{h}\rho\alpha\frac{\partial h}{\partial x_j}\frac{\partial\varphi_h}{\partial x_j}-\frac{1}{h}\rho\sum_k D_k\frac{\partial Y_k}{\partial x_j}\frac{\partial\varphi_{Y_k}}{\partial x_j}$$
$$+\frac{1}{h}\frac{\partial\rho u_j\varphi_p}{\partial x_j}+\frac{1}{h}\frac{\partial\rho u_j\varphi_{u_i}}{\partial x_j}u_i \tag{C.35}$$
$$+\frac{1}{h}\sum_k\frac{\partial\rho u_j\varphi_{Y_k}}{\partial x_j}Y_k=\frac{\partial g}{\partial h}+\frac{\partial\omega_h}{\partial h}\varphi_h+\sum_{i=1}^{N}\frac{\partial\omega_{Y_i}}{\partial h}\varphi_{Y_i}.$$

$$-\frac{\partial\rho u_j\varphi_{Y_k}}{\partial x_j}-\frac{\partial}{\partial x_j}\left(\rho D_k\frac{\partial\varphi_{Y_k}}{\partial x_j}\right)=\frac{\partial g}{\partial Y_k}+\frac{\partial\omega_h}{\partial Y_k}\varphi_h+\sum_{i=1}^{N}\frac{\partial\omega_{Y_i}}{\partial Y_k}\varphi_{Y_i}. \tag{C.36}$$

A substitution can be made in the equations for $\frac{\partial\varphi_p}{\partial x_i}$. Let $\varphi_p^*=\varphi_p+h\varphi_h+\sum_k Y_k\varphi_{Y_k}$. Then, the adjoint momentum and adjoint enthalpy equations become:

$$-\frac{\partial\rho u_j\varphi_{u_i}}{\partial x_j}-\frac{\partial\varphi_{u_j}}{\partial x_i}\rho u_j-\frac{\partial}{\partial x_j}\tau_{ji}(\varphi_u)$$
$$+\rho\varphi_h\frac{\partial h}{\partial x_i}+\rho\sum_k\varphi_{Y_k}\frac{\partial Y_k}{\partial x_i}-\rho\frac{\partial\varphi_p^*}{\partial x_i}=\frac{\partial g}{\partial u_i} \tag{C.37}$$

$$-\frac{\partial\rho u_j\varphi_h}{\partial x_j}-\frac{\partial}{\partial x_j}\left(\rho\alpha\frac{\partial\varphi_h}{\partial x_j}\right)-\frac{1}{h}\rho\alpha\frac{\partial h}{\partial x_j}\frac{\partial\varphi_h}{\partial x_j}-\frac{1}{h}\rho u_j\frac{\partial h}{\partial x_j}\varphi_h$$
$$-\frac{1}{h}\rho\sum_k D_k\frac{\partial Y_k}{\partial x_j}\frac{\partial\varphi_{Y_k}}{\partial x_j}+\frac{1}{h}\frac{\partial\rho u_j\varphi_p^*}{\partial x_j}+\frac{1}{h}\frac{\partial\rho u_j\varphi_{u_i}}{\partial x_j}u_i \tag{C.38}$$
$$-\frac{1}{h}\sum_k\rho u_j\frac{\partial Y_K}{\partial x_j}\varphi_{Y_k}=\frac{\partial g}{\partial h}+\frac{\partial\omega_h}{\partial h}\varphi_h+\sum_{i=1}^{N}\frac{\partial\omega_{Y_i}}{\partial h}\varphi_{Y_i}.$$

C.3 Boundary conditions

The boundary equations are formed from the boundary terms B, which were obtained from integtation by parts of (C.21). Each boundary equation corresponds to each variation term from W. The boundary equations are as

follows:

$$\int_{\partial\Omega} q\varphi_{u_i} n_i ds = 0 \tag{C.39}$$

$$\int_{\partial\Omega} \Big[\rho\varphi_p w_i n_i + \rho u_j \varphi_{u_j} w_i n_i + \rho\varphi_{u_i} u_j w_i n_j - \varphi_{u_i}\tau_{ji}(w) n_j + \tau_{ji}(\varphi_u) w_i n_j + \frac{P_0 c_p}{R}\varphi_h w_i n_i + \rho\left(\sum_k Y_k \varphi_{Y_k}\right) w_i n_i\Big] ds = 0 \tag{C.40}$$

$$\int_{\partial\Omega} \Big[-\frac{1}{h}\rho u_i n_i \varphi_p \delta h - \frac{1}{h}\rho u_j n_j u_i \varphi_{u_i}\delta h + \frac{1}{h}\rho\alpha\varphi_h \frac{\partial h}{\partial x_j}\delta h - \rho\alpha\varphi_h \frac{\partial \delta h}{\partial x_j} n_j + \rho\alpha \frac{\partial \varphi_h}{\partial x_j} n_j \delta h - \frac{1}{h}\rho u_j n_j \sum_k Y_k \varphi_{Y_k}\delta h + \frac{1}{h}\rho \sum_k D_k \frac{\partial Y_k}{\partial x_j}\varphi_{Y_k}\delta h\Big] ds = 0 \tag{C.41}$$

$$\int_{\partial\Omega} \left[\rho u_j n_j \varphi_{Y_k} z_k - \rho D_k \varphi_{Y_k} \frac{\partial z_k}{\partial x_j} n_j + \rho D_k \frac{\partial \varphi_{Y_k}}{\partial x_j} n_j z_k\right] ds = 0 \tag{C.42}$$

C.3.1 Inlet

At the inlet of the domain, all variables except for pressure are specified. Pressure takes a zero gradient condition. Therefore, the variation terms take the following values at the inlet:

$$w_i = 0,\ \delta h = 0,\ z_k = 0,\ \text{and}\ \frac{\partial q}{\partial x_j} n_j = 0. \tag{C.43}$$

These specifications lead to the following additional conditions on the variation terms: $\frac{\partial w_i}{\partial x_j} n_j$, $\frac{\partial \delta h}{\partial x_j} n_j$, $\frac{\partial z_k}{\partial x_j} n_j$, and q can take any value. The pressure variation equation (C.39) leads to the following condition on adjoint momentum:

$$\varphi_{u_i} n_i = 0. \tag{C.44}$$

The velocity variation equation (C.40) with $w_i = 0$ leads to the following relation on adjoint momentum:

$$\int_{\partial\Omega} \varphi_{u_i} \mu \left[\frac{\partial w_i}{\partial x_j} + \frac{\partial w_j}{\partial x_i} - \frac{2}{3} \frac{\partial w_k}{\partial x_k} \delta_{ij} \right] n_j ds = 0. \tag{C.45}$$

If this relation involving the stress variation is apllied as a boundary condition, then it can be transformed to

$$\int_{\partial\Omega} \varphi_{u_i} \mu \left[\frac{\partial w_i}{\partial x_j} + \frac{\partial w_j}{\partial x_i} - \frac{2}{3} \left(\frac{1}{\rho} \frac{\partial \rho w_k}{\partial x_k} + \rho w_k \frac{\partial (1/\rho)}{\partial x_k} \right) \delta_{ij} \right] n_j ds = 0 \tag{C.46}$$

Since $\frac{\partial \rho w_k}{\partial x_k} = 0$ and $w_i = 0$, then

$$\int_{\partial\Omega} \varphi_{u_i} \mu \left[\frac{\partial w_i}{\partial x_j} + \frac{\partial w_j}{\partial x_i} \right] n_j ds = 0 \tag{C.47}$$

Applying this as normal and tangential terms leads to the following:

$$\int_{\partial\Omega} \mu \left[\varphi_{M_n} \left(\frac{\partial w_n}{\partial x_n} + \frac{\partial w_n}{\partial x_n} \right) + \varphi_{M_t} \left(\frac{\partial w_t}{\partial x_n} + \frac{\partial w_n}{\partial x_t} \right) \right] ds = 0 \tag{C.48}$$

Since $\varphi_{M_n} = 0$ from the pressure variation boundary equation, and since the tangential gradients of w_i must be zero since $w_i = 0$ across the entire boundary, then

$$\int_{\partial\Omega} \mu \varphi_{M_t} \left[\frac{\partial w_t}{\partial x_n} \right] ds = 0 \tag{C.49}$$

Since $\frac{\partial w_t}{\partial x_n}$ can take any value, then φ_{M_t} must be zero as well.

On the other hand, if the equation (C.45) is not applied given that the variation of stress can be zeroed, then either no condition or a different condition must be specified on the inlet for φ_{M_t}.

The above relations on φ_u, along with the trivial simplification of the enthalpy and species variation boundary equations, leads to the following boundary conditions:

$$\varphi_{M_n} = 0 \tag{C.50}$$

$$\varphi_h = 0 \tag{C.51}$$

$$\varphi_{Y_k} = 0 \tag{C.52}$$

No BC is explicitly set on φ_p by the boundary equations. Since the equations are of a similar form as the primal, the BC on modified adjoint pressure will be set the same as pressure. Therefore

$$\frac{\partial \varphi_p^*}{\partial x_j} n_j = 0 \tag{C.53}$$

C.3.2 Outlet

At the outlet of the domain, all variables take a zero-gradient condition. Therefore, the variation terms at the outlet take the following values:

$$\frac{\partial w_i}{\partial x_j} n_j = 0, \ \frac{\partial \delta h}{\partial x_j} n_j = 0, \ \frac{\partial z_k}{\partial x_j} n_j = 0, \text{ and } \frac{\partial q}{\partial x_j} n_j = 0 \tag{C.54}$$

These specifications lead to the following additional information about the variation terms at the outlet: w_i, δh, z_k, and q can take any value. Additionally, to solve the adjoint pressure equation, the condition $\frac{\partial \varphi_p^*}{\partial x_j} n_j = 0$ is set in analogy to pressure in the primal equation.

The boundary equation at the outlet from the pressure variation derived with q taking any value leads to the following:

$$\varphi_{u_i} n_i = 0. \tag{C.55}$$

The velocity variation equation (C.40) with w_i taking any value leads to the following equation:

$$\begin{aligned}\rho\varphi_p n_i + \rho u_j \varphi_{u_j} n_i + \rho u_j \varphi_{u_i} n_j + \mu\left(\frac{\partial \varphi_{u_i}}{\partial x_j} + \frac{\partial \varphi_{u_j}}{\partial x_i} - \frac{2}{3}\frac{\partial \varphi_{u_k}}{\partial x_k}\delta_{ji}\right) n_j \\ + \frac{P_0 c_p}{R}\varphi_h n_i + \sum_k \rho Y_k \varphi_{Y_k} n_i = 0\end{aligned} \tag{C.56}$$

This equation can be broken down into normal and tangential components. Those equations are as follows:

$$\begin{aligned}\rho\varphi_p + \rho u_j \varphi_{u_j} + \rho u_n \varphi_{M_n} + \mu\left(2\frac{\partial \varphi_{M_n}}{\partial x_n} - \frac{2}{3}\frac{\partial \varphi_{u_k}}{\partial x_k}\delta_{ji}\right) n_j n_i \\ + \frac{P_0 c_p}{R}\varphi_h + \rho\sum_k Y_k \varphi_{Y_k} = 0\end{aligned} \tag{C.57}$$

$$\rho u_n \varphi_{M_t} + \mu\left(\frac{\partial \varphi_{M_t}}{\partial x_n} + \frac{\partial \varphi_{M_n}}{\partial x_t}\right) = 0 \tag{C.58}$$

With $\varphi_{u_j} n_j = 0$ and consequently $\frac{\partial \varphi_{u_j}}{\partial x_i} n_j t_i = 0$, and using the definition of φ_p^*, those equations simplify to

$$\varphi_p^* + u_t \varphi_{M_t} + \frac{\mu}{\rho}\left(\frac{4}{3}\frac{\partial \varphi_{M_n}}{\partial x_n} - \frac{2}{3}\frac{\partial \varphi_{M_t}}{\partial x_t}\right) = 0 \tag{C.59}$$

$$\rho u_n \varphi_{M_t} + \mu\frac{\partial \varphi_{M_t}}{\partial x_n} = 0 \tag{C.60}$$

The equation formed when taking the enthalpy variation δh is

$$-u_i n_i \varphi_p - u_j n_j u_i \varphi_{u_i} + h\alpha\frac{\partial \varphi_h}{\partial x_j} n_j - u_j n_j \sum_k Y_k \varphi_{Y_k} = 0, \tag{C.61}$$

which can be simplified and rewritten to the following

$$-u_n \varphi_p - u_n u_t \varphi_{M_t} + h\alpha\frac{\partial \varphi_h}{\partial x_n} - u_n \sum_k Y_k \varphi_{Y_k} = 0. \tag{C.62}$$

Next, substituting $\varphi_p^* = \varphi_p + h\varphi_h + \sum_k Y_k \varphi_{Y_k}$, this equation becomes:

$$u_n \varphi_h + \alpha \frac{\partial \varphi_h}{\partial x_n} = \frac{u_n}{h} \varphi_p^* + \frac{u_n}{h} u_t \varphi_{M_t}. \tag{C.63}$$

Finally, the boundary condition formed from the species mass fraction variation is:

$$u_n \varphi_{Y_k} + D_k \frac{\partial \varphi_{Y_k}}{\partial x_n} = 0. \tag{C.64}$$

Bibliography

[1] N.M. Marinov, C.K. Westbrook, and W.J. Pitz. Detailed and global kinetics model for hydrogen. *Transport phenomena in combustion*, 1:118, 1996.

[2] J. Li, Z. Zhao, A. Kazakov, and F. L. Dryer. An updated comprehensive kinetic model of hydrogen combustion. *International Journal of Chemical Kinetics*, 36(10):566–575, 2004.

[3] Michael P. Burke, Marcos Chaos, Yiguang Ju, Frederick L. Dryer, and Stephen J. Klippenstein. Comprehensive h2/o2 kinetic model for high-pressure combustion. *International Journal of Chemical Kinetics*, 44(7):444–474, 2012.

[4] K. J. Hughes, T. Turányi, A. R. Clague, and M. J. Pilling. Development and testing of a comprehensive chemical mechanism for the oxidation of methane. *International Journal of Chemical Kinetics*, 33(9):513–538, 2001.

[5] Gregory P. Smith, David M. Golden, Michael Frenklach, Nigel W. Moriarty, Boris Eiteneer, Mikhail Goldenberg, C. Thomas Bowman, Ronald K. Hanson, Soonho Song, Jr. William C. Gardiner, Vitali V. Lissianski, , and Zhiwei Qin. Gri-mech 3.0, April 2014.

[6] C.K. Westbrook, W.J. Pitz, M. Mehl, and H.J. Curran. Detailed chemical kinetic reaction mechanisms for primary reference fuels for diesel cetane number and spark-ignition octane number. *Proceedings of the Combustion Institute*, 33(1):185 – 192, 2011.

[7] H. Hippler, H. Neunaber, and J. Troe. Shock wave studies of the reactions ho+h2o2=h2o+ho2 and ho+ho2=h2o+o2 between 930 and 1680 k. *The Journal of Chemical Physics*, 103(9):3510–3516, 1995.

[8] C. Kappel, K. Luther, and J. Troe. Shock wave study of the unimolecular dissociation of h2o2 in its falloff range and of its secondary reactions. *Phys. Chem. Chem. Phys.*, 4:4392–4398, 2002.

[9] C. C. Hsu, A. M. Mebel, and M. C. Lin. Abinitio molecular orbital study of the hco+o2 reaction: Direct versus indirect abstraction channels. *The Journal of Chemical Physics*, 105(6):2346–2352, 1996.

[10] Jürgen Troe. Detailed modeling of the temperature and pressure dependence of the reaction h+o2 (+m)?ho2 (+m). *Proceedings of the Combustion Institute*, 28(2):1463 – 1469, 2000.

[11] W. Tsang and R. F. Hampson. Chemical kinetic data base for combustion chemistry. part i. methane and related compounds. *Journal of Physical and Chemical Reference Data*, 15(3):1087–1279, 1986.

[12] D. L. Baulch, C. J. Cobos, R. A. Cox, C. Esser, P. Frank, Th. Just, J. A. Kerr, M. J. Pilling, J. Troe, R. W. Walker, and J. Warnatz. Evaluated

kinetic data for combustion modelling. *Journal of Physical and Chemical Reference Data*, 21(3):411–734, 1992.

[13] S. G. Davis, A. V. Joshi, H. Wang, and F. Egolfopoulos. An optimized kinetic model of H_2/CO combustion. *Proceedings of the Combustion Institute*, 30(1):1283 – 1292, 2005.

[14] David A. Sheen, Xiaoqing You, Hai Wang, and Terese Lovas. Spectral uncertainty quantification, propagation and optimization of a detailed kinetic model for ethylene combustion. *Proceedings of the Combustion Institute*, 32(1):535 – 542, 2009.

[15] Matthew T. Reagana, Habib N. Najm, Roger G. Ghanem, and Omar M. Knio. Uncertainty quantification in reacting-flow simulations through non-intrusive spectral projection. *Combustion and Flame*, 132(3):545 – 555, 2003.

[16] M. T. Reagan, H. N. Najm, B. J. Debusschere, O. P. LeMaître, O. M. Knio, and R. G. Ghanem. Spectral stochastic uncertainty quantification in chemical systems. *Proceedings of the Physical Society*, 8:607–632, September 2004.

[17] M. T. Reagan, H. N. Najm, P. P. Pbay, O. M. Knio, and R. G. Ghanem. Quantifying uncertainty in chemical systems modeling. *International Journal of Chemical Kinetics*, 37(6):368–382, 2005.

[18] Michael Frenklach, Andrew Packard, Pete Seiler, and Ryan Feeley. Collaborative data processing in developing predictive models of complex reaction systems. *International Journal of Chemical Kinetics*, 36(1):57–66, 2004.

[19] Ryan Feeley, Michael Frenklach, Matt Onsum, Trent Russi, Adam Arkin, and Andrew Packard. Model discrimination using data collaboration. *The Journal of Physical Chemistry A*, 110:6803–6813, 2005.

[20] Trent Russi, Andrew Packard, Ryan Feeley, and Michael Frenklach. Sensitivity analysis of uncertainty in model prediction. *The Journal of Physical Chemistry A*, 112(12):2579–2588, 2008. PMID: 18303866.

[21] David Sheen and Hai Wang. Modeling high-pressure $H_2/CO/O_2$/diluent mass burning rates with the method of uncertainty minimization using polynomial chaos expansions. In *7th US National Technical Meeting of the Combustion Institute*, March 2011.

[22] David A. Sheen and Hai Wang. The method of uncertainty quantification and minimization using polynomial chaos expansions. *Combustion and Flame*, 158(12):2358 – 2374, 2011.

[23] M.J. Brown, D.B. Smith, and S.C. Taylor. Influence of uncertainties in rate constants on computed burning velocities. *Combustion and Flame*, 117(3):652–656, May.

[24] K. J. Hughes, T. Turányi, A. R. Clague, and M. J. Pilling. Development and testing of a comprehensive chemical mechanism for the oxidation of methane. *International Journal of Chemical Kinetics*, 33(9):513–538, 2001.

[25] Stephen J. Klippenstein, Lawrence B. Harding, Michael J. Davis, Alison S. Tomlin, and Rex T. Skodje. Uncertainty driven theoretical kinetics studies for CH_3OH ignition: HO_2 + CH_3OH and O_2 + CH_3OH. *Proceedings of the Combustion Institute*, 33(1):351 – 357, 2011.

[26] A Tomlin. The use of global uncertainty methods for the evaluation of combustion mechanisms. *Reliability Engineering System Safety*, 91(10-11):1219–1231, 2006.

[27] T. Ziehn, K. J. Hughes, J. F. Griffiths, R. Porter, and A. S. Tomlin. A global sensitivity study of cyclohexane oxidation under low temperature fuel-rich conditions using hdmr methods. *Combustion Theory and Modelling*, 13(4):589–605, 2009.

[28] M. D. Smooke, H. Rabitz, Y. Reuven, and F. L. Dryer. Application of sensitivity analysis to premixed hydrogen-air flames. *Combustion Science and Technology*, 59(4-6):295–319, 1988.

[29] Zhenwei Zhao, Juan Li, Andrei Kazakov, and Frederick L. Dryer. Temperature-dependent feature sensitivity analysis for combustion modeling. *International Journal of Chemical Kinetics*, 37(5):282–295, 2005.

[30] Michael Frenklach. Systematic optimization of a detailed kinetic model using a methane ignition example. *Combustion and Flame*, 58(1):69 – 72, 1984.

[31] Michael Frenklach, Hai Wang, and Martin J. Rabinowitz. Optimization and analysis of large chemical kinetic mechanisms using the solution mapping method–combustion of methane. *Progress in Energy and Combustion Science*, 18(1):47 – 73, 1992.

[32] Ryan Feeley, Pete Seiler, Andrew Packard, and Michael Frenklach. Consistency of a reaction dataset. *The Journal of Physical Chemistry A*, 108(44):9573–9583, 2004.

[33] P Seiler, M Frenklach, A Packard, and R Feeley. Numerical approaches for collaborative data processing. *Optimization and Engineering*, 7(4):459–478, 2006.

[34] Trent Russi, Andy Packard, and Michael Frenklach. Uncertainty quantification: Making predictions of complex reaction systems reliable. *Chemical Physics Letters*, 499(1):1 – 8, 2010.

[35] Irving Wender. Reactions of synthesis gas. *Fuel Processing Technology*, 48(3):189 – 297, 1996.

[36] H.J. Herzog and N. Vukmirovic. *CO_2 Sequestration: Opportunities and Challenges*. American Institute of Chemical Engineers, 1998.

[37] Michael P Burke, Marcos Chaos, Frederick L Dryer, and Yiguang Ju. Negative pressure dependence of mass burning rates of $H_2/CO/O_2$/diluent flames at low flame temperatures. *Combustion and Flame*, 157(4):618–631, 2010.

[38] R. T. Cox. *The Algebra of Probable Inference*. Johns Hopkins University Press, 1961.

[39] Robert P. Christian. *The Bayesian Choice*. Springer, 2001.

[40] E. T. Jaynes. *Probability Theory: The Logic of Science*. Cambridge University Press, 2003.

[41] Jari Kaipio and Erkki Somersalo. *Statistical and Computational Inverse Problems*. Springer, 2005.

[42] Daniela Calvetti and Erkki Somersalo. *Introduction to Bayesian Scientific Computing*. Springer, 2007.

[43] H. N. Najm, B. J. Debusschere, Y. M. Marzouk, S. Widmer, and O. P. Le Matre. Uncertainty quantification in chemical systems. *International Journal for Numerical Methods in Engineering*, 80(6-7):789–814, 2009.

[44] Xun Huan and Youssef Marzouk. Optimal bayesian experimental design for combustion kinetics. In *49th AIAA Aerospace Sciences Meeting*, January 2011. Paper AIAA 2011-0513.

[45] Kenji Miki, Sai Hung Cheung, Ernesto E. Prudencio, and Philip L. Varghese. Bayesian uncertainty quantification of recent shock tube determinations of the rate coefficient of reaction H + O_2 = OH + O. *International Journal of Chemical Kinetics*, 44(9):586–597, 2012.

[46] K. Miki, M. Panesi, E.E. Prudencio, and S. Prudhomme. Probabilistic models and uncertainty quantification for the ionization reaction rate of atomic nitrogen. *Journal of Computational Physics*, 231(9):3871 – 3886, 2012.

[47] M. Muto and J. L. Beck. Bayesian updating and model class selection of hysteretic structural models using stochastic simulation. *J. Vib. Control*, 14:7–34, 2008.

[48] S. Kullback and R. A. Leibler. On information and sufficiency. *Annals of Mathematical Statistics*, 22(1):79–86, 1951.

[49] S. H. Cheung and J. L. Beck. *New Bayesian updating methodology for model validation and robust predictions based on data from hierarchical subsystem tests.* EERL Report No. 2008-04, California Institute of Technology, 2008.

[50] Ernesto E. Prudencio and Sai Hung Cheung. Parallel adaptive multilevel sampling algorithms for the Bayesian analysis of mathmatical models. *International Journal for Uncertainty Quantification*, 2(3):215–237, 2012.

[51] Ernesto Prudencio and Karl W. Schulz. The Parallel C++ statistical Library QUESO: Quantification of Uncertainty for Estimation, Simulation and Optimization. In *Workshop on Algorithms and Programming Tools for Next-Generation High-Performance Scientific Software HPSS*, Bordeaux, France, 2011.

[52] J. Li, Z. Zhao, A. Kazakov, M. Chaos, F. L. Dryer, and J. J. Scire. A comprehensive kinetic mechanism for CO, CH_2O, and CH_3OH combustion. *International Journal of Chemical Kinetics*, 39(3):109–136, 2007.

[53] H. Sun, S.I. Yang, G. Jomaas, and C.K. Law. High-pressure laminar flame speeds and kinetic modeling of carbon monoxide/hydrogen combustion. *Proceedings of the Combustion Institute*, 31(1):439 – 446, 2007.

[54] Jürgen Warnatz. Resolution of gas phase and surface combustion chemistry into elementary reactions. *Symposium (International) on Combustion*, 24(1):553 – 579, 1992.

[55] R. Kee, J. Grcar, M. Smooke, and J. Miller. A fortran program for modeling steady laminar one-dimensional premixed flames. Technical Report SAND85-8240, Sandia National Lab., Albuquerque, NM, 1985.

[56] R. Kee, G. Dixon-Lewis, J. Warnatz, M. Coltrin, and J. Miller. A fortran computer package for the evaluation of gas-phase, multicomponent transport properties. Technical Report SAND86-8246, Sandia National Lab., Albuquerque, NM, 1986.

[57] Andrew Gelman, John B. Carlin, Hal S. Stern, and Donald B. Rubin. *Bayesian Data Analysis*. Chapman & Hall, 2003.

[58] S. Goldman. *Information Theory*. Prentice-Hall, 1953.

[59] Tamás Turányi. Sensitivity analysis of complex kinetic systems. tools and applications. *Journal of Mathematical Chemistry*, 5(3):203–248, 1990.

[60] Kyle E Niemeyer, Chih-Jen Sung, and Mandhapati P Raju. Skeletal mechanism generation for surrogate fuels using directed relation graph with error propagation and sensitivity analysis. *Combustion and Flame*, 157(9):1760–1770, 2010.

[61] Zhaoyu Luo, Max Plomer, Tianfeng Lu, Sibendu Som, and Douglas E Longman. A reduced mechanism for biodiesel surrogates with low temperature chemistry. In *7th US National Combustion Meeting, Atlanta, GA*, 2011.

[62] Tianfeng Lu and Chung K. Law. Toward accommodating realistic fuel chemistry in large-scale computations. *Progress in Energy and Combustion Science*, 35(2):192 – 215, 2009.

[63] David Miller and Michael Frenklach. Sensitivity analysis and parameter estimation in dynamic modeling of chemical kinetics. *International Journal of Chemical Kinetics*, 15(7):677–696, 1983.

[64] I.M. Sobol. Global sensitivity indices for nonlinear mathematical models and their monte carlo estimates. *Mathematics and Computers in Simulation*, 55(13):271 – 280, 2001. The Second {IMACS} Seminar on Monte Carlo Methods.

[65] Genyuan Li, Carey Rosenthal, and Herschel Rabitz. High dimensional model representations. *The Journal of Physical Chemistry A*, 105(33):7765–7777, 2001.

[66] Michael J. Davis, Rex T. Skodje, and Alison S. Tomlin. Global sensitivity analysis of chemical-kinetic reaction mechanisms: Construction and deconstruction of the probability density function. *The Journal of Physical Chemistry A*, 115(9):1556–1578, 2011.

[67] A. Jameson. Aerodynamic design via control theory. *Journal of Scientific Computing*, 3:233–260, 1988.

[68] O. Baysal and M. E. Eleshaky. Aerodynamic design optimization using sensitivity analysis and computational fluid dynamics. In *29th Aerospace Sciences Meeting and Exhibit*, number AIAA 92-0471. American Institute of Aeronautics and Astronautics, 1991.

[69] A. Jameson, N. Pierce, and L. Martinelli. Optimum aerodynamic design using the navier-stokes equations. In *35th Aerospace Sciences Meeting and Exhibit*, number AIAA 97-0101. American Institute of Aeronautics and Astronautics, 1997.

[70] J. Reuther, J.J. Alonso, M.J. Rimlinger, and A. Jameson. Aerodynamic shape optimization of supersonic aircraft configurations via an adjoint formulation on distributed memory parallel computers. *Computers & Fluids*, 28(45):675 – 700, 1999.

[71] M.B. Giles and N.A. Pierce. An introduction to the adjoint approach to design. *Flow, Turbulence and Combustion*, 65:393–415, 2000.

[72] S. Kim, J.J. Alonso, and A. Jameson. In *40th Aerospace Sciences Meeting and Exhibit*, number AIAA 2002-0844. American Institute of Aeronautics and Astronautics, 2002.

[73] M.D. Gunzburger, L. Hou, and T.P. Svobodny. Boundary velocity control of incompressible flow with an application to viscous drag reduction. *SIAM J. Control Optim.*, 30(1):167–181, January 1992.

[74] T.R. Bewly, P. Moin, and R. Temam. Dns-based predictive control of turbulence: an optimal benchmark for feedback algorithms. *Journal of Fluid Mechanics*, 447:179–225, 10 2001.

[75] M. Wei and J. B. Freund. A noise-controlled free shear flow. *Journal of Fluid Mechanics*, 546:123, December 2005.

[76] J. Freund, J. Kim, and D. Bodony. Adjoint-based optimal control of a mach 1.3 turbulent jet for noise reduction. In *49th AIAA Aerospace Sciences Meeting including the New Horizons Forum and Aerospace Exposition*. American Institute of Aeronautics and Astronautics, 2011.

[77] Gary J. Chandler, Matthew P. Juniper, Joseph W. Nichols, and Peter J. Schmid. Adjoint algorithms for the navier-stokes equations in the low mach number limit. *J. Comput. Phys.*, 231(4):1900–1916, February 2012.

[78] A. Sandu, D.N. Daescu, and G. R. Carmichael. Direct and adjoint sensitivity analysis of chemical kinetic systems with kpp: Part i–theory and software tools. *Atmospheric Environment*, 37:5083–5096, 2003.

[79] A. Sandu, D. N. Daescu, G. R. Carmichael, and T. Chai. Adjoint sensitivity analysis of regional air quality models. *Journal of Computational Physics*, 204(1):222 – 252, 2005.

[80] A. Sandu and L. Zhang. Discrete second order adjoints in atmospheric chemical transport modeling. *Journal of Computational Physics*, 227(12):5949 – 5983, 2008.

[81] Charles David Pierce. *Progress-variable approach for large-eddy simulation of turbulent combustion*. PhD thesis, Stanford University, 2001.

[82] Venkatramanan Raman, Heinz Pitsch, and Rodney O Fox. Hybrid large-eddy simulation/lagrangian filtered-density-function approach for simulating turbulent combustion. *Combustion and Flame*, 143(1):56–78, 2005.

[83] V. V. Toro, A. V. Mokhov, H. B. Levinsky, and M. D. Smooke. Combined experimental and computational study of laminar, axisymmetric

hydrogenair diffusion flames. *Proceedings of The Combustion Institute*, 30:485–492, 2005.

[84] E. Ranzi, A. Frassoldati, R. Grana, A. Cuoci, T. Faravelli, A.P. Kelley, and C.K. Law. Hierarchical and comparative kinetic modeling of laminar flame speeds of hydrocarbon and oxygenated fuels. *Progress in Energy and Combustion Science*, 38(4):468 – 501, 2012.

[85] Qiqi Wang. Forward and adjoint sensitivity computation of chaotic dynamical systems. *Journal of Computational Physics*, 235(0):1 – 13, 2013.

[86] Kalen Braman, Todd A. Oliver, and Venkat Raman. Bayesian analysis of syngas chemistry models. *Combustion Theory and Modelling*, 17(5):858–887, 2013.

[87] Michael E. Mueller and Venkat Raman. Effects of turbulent combustion modeling errors on soot evolution in turbulent nonpremixed jet flames. *Combustion and Flame*, In revision.

[88] J. B. Bell and D. L. Marcus. A second-order projection method for variable-density flows. *Journal of Computational Physics*, 101:334–348, August 1992.

[89] J. Kim and P. Moin. Application of a fractional-step method to incompressible Navier-Stokes equations. *Journal of Computational Physics*, 59:308–323, June 1985.

[90] Olivier Desjardins, Guillaume Blanquart, Guillaume Balarac, and Heinz Pitsch. High order conservative finite difference scheme for variable density low mach number turbulent flows. *Journal of Computational Physics*, 227(15):7125 – 7159, 2008.

[91] A. Ern, C.C. Douglas, and M.D. Smooke. Detailed chemistry modeling of laminar diffusion flames on parallel computers. *The International Journal of Supercomputer Applications and High Performance Computing*, 9:167–186, 1994.

[92] M.D. Smooke, C.S. McEnally, L.D. Pfefferle, R.J. Hall, and M.B. Colket. Computational and experimental study of soot formation in a coflow, laminar diffusion flame. *Combustion and Flame*, 117(12):117 – 139, 1999.

[93] Alexander A. Konnov. Remaining uncertainties in the kinetic mechanism of hydrogen combustion. *Combustion and Flame*, 152(4):507 – 528, 2008.